

BEAM STEERABLE MEANDERLINE ANTENNA USING VARACTOR
DIODES AND RECONFIGURABLE ANTENNA DESIGNS BY MEMS
SWITCHES

A THESIS SUBMITTED TO
THE GRADUATE SCHOOL OF NATURAL AND APPLIED SCIENCES
OF
MIDDLE EAST TECHNICAL UNIVERSITY

BY

NIHAN GÖKALP

IN PARTIAL FULFILLMENT OF THE REQUIREMENTS
FOR
THE DEGREE OF MASTER OF SCIENCE
IN
ELECTRICAL AND ELECTRONICS ENGINEERING

AUGUST 2008

Approval of the thesis:

**BEAM STEERABLE MEANDERLINE ANTENNA USING VARACTOR
DIODES AND RECONFIGURABLE ANTENNA DESIGNS BY MEMS
SWITCHES**

submitted by **NİHAN GÖKALP** in partial fulfillment of the requirements for the
degree of **Master of Science in Electrical and Electronics Engineering**
Department, Middle East Technical University by,

Prof. Dr. Canan Özgen

Dean, Graduate School of **Natural and Applied Sciences**

Prof. Dr. İsmet Erkmen

Head of Department, **Electrical and Electronics Engineering**

Assoc. Prof. Dr. H. Özlem Aydın Çivi

Supervisor, **Electrical and Electronics Eng. Dept., METU**

Examining Committee Members:

Prof. Dr. Altunkan Hızal

Electrical and Electronics Engineering Dept., METU

Assoc. Prof. Dr. H. Özlem Aydın Çivi

Electrical and Electronics Engineering Dept., METU

Assoc. Prof. Dr. Şimşek Demir

Electrical and Electronics Engineering Dept., METU

Asst. Prof. Dr. Lale Alatan

Electrical and Electronics Engineering Dept., METU

(M.S.) M.Erim İnal

ASELSAN

Date:

22.08.2008

I hereby declare that all information in this document has been obtained and presented in accordance with academic rules and ethical conduct. I also declare that, as required by these rules and conduct, I have fully cited and referenced all material and results that are not original to this work.

Name, Last name : Nihan GÖKALP

Signature :

ABSTRACT

BEAM STEERABLE MEANDERLINE ANTENNA USING VARACTOR DIODES AND RECONFIGURABLE ANTENNA DESIGNS BY MEMS SWITCHES

GÖKALP, Nihan

M.S., Department of Electrical and Electronics Engineering

Supervisor : Assoc. Prof. Dr. H. Özlem AYDIN ÇİVİ

August 2008, 114 pages

Recently, reconfigurable antennas have attracted significant interest due to their high adaptation with changing system requirements and environmental conditions. Reconfigurable antennas have the ability to change their radiation pattern, frequency or polarization independently according to the application requirements.

In this thesis, three different reconfigurable antenna structures have been designed; beam-steerable meanderline antenna, dual circularly polarized meanderline antenna and dual-frequency slot-dipole array. Traveling wave meanderline antenna arrays are investigated in detail and a beam-steerable traveling wave meanderline antenna array has been introduced for X-band applications. Beam-steering capability of the antenna array has been achieved by loading the antenna elements with varactor diodes. Theoretical analysis and computer simulations of the proposed antenna have been verified with experimental results. Radiation direction of the 8-element meanderline

array can be rotated 10° by changing the varactor diode's bias voltage from 0V up to 20V. Also, a polarization-agile meanderline antenna array has been designed and simulated. Polarization of the circularly polarized meanderline array can be altered between right hand circularly polarized and left hand circularly polarized by using RF MEMS switches. The third type of reconfigurable antenna investigated in this thesis is a dual frequency slot-dipole array operating at X- and Ka-band. Electrical length of the slot dipoles has been tuned by using RF MEMS switches. Antenna prototypes have been manufactured for 'on' and 'off' states of RF MEMS switches and it has been shown that the operating frequency can be changed between 10 GHz and 15.4 GHz.

Keywords: Reconfigurable Antennas, Meanderline Antenna Arrays, Frequency Reconfigurable Antennas, Beam-Steerable Antennas, Polarization-Agile Antennas

ÖZ

VARAKTÖR DİYOTLU IŞIN HÜZMESİ YÖNLENDİRİLEBİLEN SUR BİÇİMLİ ANTEN VE MEMS ANAHTARLARLA AYARLANABİLİR ANTEN TASARIMLARI

GÖKALP, Nihan

Yüksek Lisans, Elektrik ve Elektronik Mühendisliği Bölümü

Tez Yöneticisi : Doç. Dr. H. Özlem AYDIN ÇİVİ

Ağustos 2008, 114 sayfa

Günümüzde, ayarlanabilir antenler değişen sistem ihtiyaçlarına ve çevre koşullarına yüksek uyumlulukları nedeniyle ilgi çekmektedir. Ayarlanabilir antenler uygulama gereksinimlerine göre ışıınım huzmelerini, frekanslarını ve polarizasyonlarını bağımsız olarak değiştirme yeteneğine sahiptir.

Bu tezde, üç farklı ayarlanabilir anten yapısı tasarlanmıştır; ışıınım huzmesi yönlendirilebilen sur biçimli anten, polarizasyonu ayarlanabilen sur biçimli anten ve çift frekanslı yarık dipol anten dizisi. Sur biçimli yürüyen dalga antenler ayrıntılı biçimde incelenmiş ve X-bant uygulamaları için ışıınım huzmesi yönlendirilebilen sur biçimli yürüyen dalga anten dizisi tanıtılmıştır. Anten dizisine ışıınım huzmesi yönlendirme özelliği, anten elemanları varaktör diyotlarla yüklenerek kazandırılmıştır. Önerilen anten dizisi ile ilgili gerçekleştirilen kuramsal tahminler ve bilgisayar benzetimleri deneysel ölçümlerle doğrulanmıştır. Varaktör diyotlara 0V'tan 20V'ta kadar besleme voltajı uygulandığında, 8 elemanlı sur biçimli anten

dizisinin ışınlım yönü 10° dönmektedir. Bununla beraber, polarizasyonu ayarlanabilen sur biçimli anten dizisi tasarlanmış ve EM benzetimleri yapılmıştır. RF MEMS anahtarlar kullanılarak, dairesel polarizasyonlu sur biçimli antenin polarizasyonu sağ el dairesel polarizasyon veya sol el dairesel polarizasyon olarak değişebilmektedir. Bu tezde incelenen üçüncü tip ayarlanabilir anten. X- ve Ka-bant uygulama frekansı ayarlanabilen yarık-dipol anten dizisidir. Yarık-dipol antenlerin elektriksel uzunlukları RF MEMS anahtarlar kullanılarak ayarlanabilmektedir. RF MEMS anahtarların açık ve kapalı durumları için anten örnekleri üretilmiş ve çalışma frekansının 10GHz ve 15.4 GHz olarak değiştiği gösterilmiştir.

Anahtar Kelimeler: Ayarlanabilen Antenler, Sur Biçimli Antenler, Frekans Ayarlanabilen Antenler, Işınlım Huzmesi Yönlendirilebilen Antenler, Polarizasyon Ayarlanabilen Antenler

To My Family

ACKNOWLEDGMENTS

I would like to thank Assoc. Prof. Dr. Özlem Aydın Çivi for her valuable supervision, support and tolerance throughout the development and improvement of this thesis.

I am grateful to Ali Günay Yıldız, Erhan Halavut, Tuncay Erdöl, Hakan Paruldar and Tülay Can for their support throughout the development and the improvement of this thesis. I would like to extend my special appreciation and gratitude to Volkan Öznazlı and my family and for their encouragement and understanding of my spending lots of time on this work.

I am also grateful to Aselsan Electronics Industries Inc. for the resources and facilities that I use throughout thesis.

I would also like to thank Turkish Scientific and Technological Research Council (TÜBİTAK) for their financial assistance during my graduate study.

Thanks a lot to all my friends for their great encouragement and their valuable help to accomplish this work.

TABLE OF CONTENTS

ABSTRACT	IV
ÖZ.....	VI
ACKNOWLEDGMENTS	IX
TABLE OF CONTENTS.....	X
LIST OF TABLES	XII
LIST OF FIGURES	XIII
CHAPTERS	
1. INTRODUCTION.....	1
2. RECONFIGURABLE ANTENNAS	4
2.1 RECONFIGURABILITY FOR ANTENNA ELEMENTS.....	5
2.1.1 <i>Frequency Reconfiguration</i>	5
2.1.2 <i>Polarization Reconfiguration</i>	8
2.1.3 <i>Radiation Pattern Reconfiguration</i>	8
2.2 RECONFIGURATION MECHANISM FOR ANTENNAS.....	9
2.2.1 <i>Switches</i>	10
2.2.2 <i>Variable Reactive Loading</i>	10
2.2.3 <i>Mechanical and Material Parameter Changes</i>	11
3. TRAVELING WAVE ANTENNAS	13
3.1 MICROSTRIP TRAVELING WAVE ANTENNAS.....	14
3.2 MEANDERLINE ARRAYS (RAMPART ANTENNA).....	18
3.2.1 <i>Radiation Mechanism of the Unit Meanderline Cell</i>	19
3.2.2 <i>Lumped Approximate Network Model of the Meanderline Cell</i>	27
4. DESIGN OF LINEARLY POLARIZED TRAVELLING WAVE MEANDERLINE ARRAY	31
4.1 DESIGN SPECIFICATIONS	31
4.2 INITIAL DESIGN.....	32
4.3 FULL-WAVE EM SIMULATIONS	34
4.4 FABRICATION OF THE ANTENNA	40

4.5	MEASUREMENTS	41
4.5.1	<i>S-Parameter Measurements of the Meander Line Array</i>	41
4.5.2	<i>Radiation Pattern Measurements of the Meander Line Array</i>	43
5.	DESIGN OF BEAM-STEERABLE TRAVELING WAVE MEANDERLINE ANTENNA	51
5.2	VARACTOR DIODE PHASE SHIFTING MECHANISM	52
5.2.1	<i>Characterization of Varactor Diode</i>	53
5.3	THEORETICAL INVESTIGATIONS OF BEAM-STEERABLE TRAVELING WAVE ANTENNA	56
5.4	EM SIMULATION RESULTS	57
5.5	PRODUCTION OF BEAM STEERABLE ANTENNA	65
5.6	MEASUREMENTS	66
5.6.1	<i>S-parameter Measurements</i>	66
5.6.2	<i>Radiation Pattern Measurements</i>	68
5.7	FURTHER INVESTIGATIONS ON BEAM-STEERABLE TRAVELING WAVE MEANDERLINE ARRAY	74
5.7.1	<i>Varactor Diode Loaded Branch-Line Coupler Phase Shifters</i>	74
5.7.2	<i>Application of Phase Shifter on Traveling Wave Arrays</i>	77
6.	DUAL CP POLARIZED TRAVELING WAVE MEANDERLINE ARRAY USING RF MEMS TECHNOLOGY FOR X-BAND APPLICATIONS	80
7.	DUAL FREQUENCY SLOT DIPOLE ARRAY FOR X- AND KA- BAND APPLICATIONS	85
7.1	RECONFIGURABLE SLOT DIPOLE ANTENNA	86
7.2	CPW-BASED FEED NETWORK	91
7.3	TWO ELEMENT SLOT DIPOLE DUAL-FREQUENCY ARRAY STRUCTURE	92
8.	CONCLUSION	98
	REFERENCES	100
	APPENDICES	104
A.	EFFECTIVE DIELECTRIC CONSTANT AND CHARACTERISTIC IMPEDANCE OF MICROSTRIP LINES	104
B.	ASELSAN TAPERED ANECHOIC CHAMBER MEASUREMENT SYSTEM	106
C.	RO5880 HIGH-FREQUENCY LAMINATE DATASHEET	109
D.	MICROSEMI MPV-2100 VARACTOR DIODE DATASHEET	112
E.	MEMS SWITCH OPERATION	115

LIST OF TABLES

Table 3.1 Polarization Components of a Meanderline Antenna	26
Table 5.1 Microsemi MPV 2100 Type Capacitors Applied Voltage vs. Capacitance Values.....	52
Table 5.2 Gain Variation of Meanderline Array for Different Values of Varactor Diodes Capacitance (Ansoft Designer Simulation)	64
Table 6.1 Axial Ratio of the Polarization-Agile Meanderline Array around Main Beam at 10 GHz.....	84
Table 6.2 Simulation of LHCP and RHCP values for the 1 st and 2 nd States of RF MEMS Switches	84

LIST OF FIGURES

Figure 2.1 2-Element Frequency Tunable Slot Dipole Antenna Array Structure with MEMS Switches.....	7
Figure 3.1 Single Wire Transmission Line over Ground Terminated with a Matched Load	13
Figure 3.2 Rectangular Loop Type Microstrip Chain Antenna	15
Figure 3.3 TEM Line Antenna Geometry	16
Figure 3.4 A Series Microstrip Patch Traveling-Wave Antenna Configuration.....	17
Figure 3.5 Compline Microstrip Traveling Wave Antenna	17
Figure 3.6 Geometry of a Franklin-Type Microstrip Traveling Wave Antenna.....	18
Figure 3.7 A Representation of Meanderline Array Section	19
Figure 3.8 Unit Cells of Different Types of Meanderline Array	19
Figure 3.9 (a)Equivalent Current Source Distribution at the Right Angle Bend (b)Equivalent Model of Four Cornered Meanderline Cell.....	20
Figure 3.10 Magnetic Current Vectors on Meander Line Unit Cell	21
Figure 3.11 Diagonally Polarized E-Field Vectors of Meanderline Cell.....	25
Figure 3.12 (a) Right Angle Bend of Meanderline (b) Equivalent Circuit of Right Angle Bend	28
Figure 3.13 (a) Four Cornered Meanderline Array (b) Equivalent Circuit Model of Four Corner Meanderline Array.....	29
Figure 4.1 Ansoft Designer Schematic Model of Linearly Polarized 8 Element Meanderline Array	35

Figure 4.2 Ansoft Designer and HFSS S11 Simulations of Linearly Polarized Meanderline Array.....	36
Figure 4.3 Ansoft Designer and HFSS E-plane Electric Field Pattern of Linearly Polarized Meanderline Array at 10 GHz.....	37
Figure 4.4 Co- and Cross-Polarization E-Plane Electric Field Patterns of Meanderline Array at 10 GHz.....	38
Figure 4.5 Co- and Cross-Polarization H-Plane Electric Field Patterns of Meanderline Array at 10 GHz.....	38
Figure 4.6 3-Dimensional Radiation Pattern of Meanderline Array.....	39
Figure 4.7 Surface Current Distribution of Meanderline Array.....	40
Figure 4.8 Prototype of Linearly Polarized Meanderline Array for X-band Applications	41
Figure 4.9 S11 (Return Loss) Measurement and Simulation Results of Linearly Polarized Meanderline Array	42
Figure 4.10 S21 Measurement and Simulation Results of Linearly Polarized Meanderline Array	43
Figure 4.11 Linearly Polarized Meanderline Array under Test in Tapered Anechoic Chamber at ASELSAN Facilities.....	44
Figure 4.12 Meanderline Array E-plane Electric Field Pattern Co-Polarization Measurement and Simulation Results.....	46
Figure 4.13 Meanderline Array E-Plane and H-Plane Electric Field Pattern Measurement Results	48
Figure 4.14 Meanderline Array E-Plane Co-and Cross-Polarization Electric Field Pattern Measurement Results.....	50
Figure 5.1 The Schematic View of Beam-Steerable Meanderline Antenna	51
Figure 5.2 Bias Circuit of the Microsemi MPV2100 Varactor Diode Placed on the 50- Ω Microstrip Line	53

Figure 5.3 S-Parameter Measurement of Varactor Diode Bias Circuit	54
Figure 5.4 Measurement of Phase Variation with Respect to Different DC Bias Voltages	54
Figure 5.5 Relation between Applied Bias Voltage and Varactor Diode Capacitance	55
Figure 5.6 Ansoft Designer Model of the Beam Steerable Rampart Antenna with Varactor Diodes and Bias Lines.....	58
Figure 5.7 Unit Element of Beam-Steerable Meanderline Array	59
Figure 5.8 S11 Simulation of Beam-Steerable Meanderline Array for Various Capacitance Values	60
Figure 5.9 S21 Simulation of Beam-Steerable Meanderline Array for Various Capacitance Values	60
Figure 5.10 E-Plane Electric Field Pattern of Beam-Steerable Meanderline Array for Different Values of Varactor Capacitance (Ansoft Designer Simulation).....	61
Figure 5.11 Beam Variation of Beam-Steerable Meanderline Array with respect to Varactor Capacitance Variation (Ansoft Designer Simulation).....	62
Figure 5.12 Co- and Cross-Polarization E-Plane Electric Field Patterns of Beam-Steerable Meanderline Array at 10 GHz.....	63
Figure 5.13 Co- and Cross-Polarization H-Plane Electric Field Patterns of Beam-Steerable Meanderline Array at 10 GHz.....	63
Figure 5.14 Surface Current Distribution of Meanderline Array.....	65
Figure 5.15 Prototype of Beam-Steerable Rampart Antenna with Varactor Diodes .	65
Figure 5.16 Unit Cell of the Beam Steering Rampart Antenna with DC Bias Pad....	66
Figure 5.17 S11 Measurement of Beam-Steerable Meanderline Array Under Different Bias Voltages.....	67
Figure 5.18 S21 Measurement of Beam-Steerable Meanderline Array under Different Bias Voltages	68
Figure 5.19 E-plane Electric Field Pattern Measurement under 0 Volt Bias Voltage	

and Ansoft Designer Simulation with 2.4 pF Varactor Capacitance	69
Figure 5.20 E-plane Electric Field Pattern Measurement under 10 Volt Bias Voltage and Ansoft Designer Simulation with 0.5 pF Varactor Capacitance	69
Figure 5.21 E-plane Electric Field Pattern Measurement under 20 Volt Bias Voltage and Ansoft Designer Simulation with 0.3 pF Varactor Capacitance	70
Figure 5.22 E-Plane Electric Field Pattern of Beam-Steerable Meanderline Array at 9.5 GHz Under Different Values of Bias Voltages.....	71
Figure 5.23 E-Plane Electric Field Pattern of Beam-Steerable Meanderline Array at 10 GHz Under Different Values of Bias Voltages.....	71
Figure 5.24 E-Plane Electric Field Pattern of Beam-Steerable Meanderline Array at 10.5 GHz Under Different Values of Bias Voltages.....	72
Figure 5.25 H-Plane Electric Field Pattern of Beam-Steerable Meanderline Array at 9.5 GHz Under Different Values of Bias Voltages.....	72
Figure 5.26 H-Plane Electric Field Pattern of Beam-Steerable Meanderline Array at 10.5 GHz Under Different Values of Bias Voltages.....	73
Figure 5.27 H-Plane Electric Field Pattern of Beam-Steerable Meanderline Array at 10.5 GHz Under Different Values of Bias Voltages.....	73
Figure 5.28 Ansoft Designer Model of 3-dB Branch-Line Coupler	75
Figure 5.29 Ansoft Designer S-Parameter Simulation of 3-dB Branch-Line Coupler	76
Figure 5.30 Ansoft Designer Model of Reflective Type Phase Shifter Loaded with Varactor Diodes	76
Figure 5.31 Ansoft Designer Simulation of Branch-Line Coupler Phase Variation with respect to Varactor Capacitance.....	77
Figure 5.32 Meanderline Array with Varactor Diode Loaded Branch-Line Coupler Phase Shifter	78
Figure 5.33 E-Plane Electric Field Pattern of Beam-Steerable Meanderline Array for Different Values of Varactor Capacitance (Ansoft Designer Simulation).....	78

Figure 6.1 The Schematic View of Polarization-Agile Meanderline Array	81
Figure 6.2 HFSS Model of the Polarization-Agile Meanderline Array	82
Figure 6.3 S11-Parameter Simulation of Polarization-Agile Meanderline Array.....	82
Figure 6.4 E-Plane Co-Polarization Pattern of Polarization-Agile Meanderline Array at 10 GHz	83
Figure 7.1 The Schematic View of 2-Element Reconfigurable Slot Dipole Antenna Array Structure with MEMS Switches	86
Figure 7.2 The Schematic View of Reconfigurable Slot Dipole Antenna with MEMS Switches Located on the Arms to Control Resonant Frequency.....	87
Figure 7.3 Prototype structures of slot dipole antenna with metallic strips instead of RF MEMS switches	87
Figure 7.4 Measurement and simulation results of a slot dipole antenna with metallic strips instead of RF MEMS switches	88
Figure 7.5 E-Plane Electric Field Pattern of Single Dipole Antenna at 10 GHz for the Switches are Up-State Case	89
Figure 7.6 H-Plane Electric Field Pattern of Single Dipole Antenna at 10 GHz for the Switches are Up-State Case	89
Figure 7.7 E-Plane Electric Field Pattern of Single Dipole Antenna at 15.4 GHz for the Switches are Down-State Case.....	90
Figure 7.8 H-Plane Electric Field Pattern of the Single Dipole Antenna at 15.4 GHz for the Switches are Down-State Case	90
Figure 7.9 The Circuit Schematic View and Parameters of the Dual-Frequency Transformer.....	91
Figure 7.10 Measurement and simulation results of dual-frequency transformer operating at X- and Ka- Band	92
Figure 7.11 Prototype Structures of 2-Element Reconfigurable Slot Dipole Antenna Array with Metallic Strips Instead of RF MEMS Switches.....	93
Figure 7.12 S11 Measurement Results of 2-Element Slot Dipole Antenna Array with	

Metallic Strips instead of RF MEMS Switches	94
Figure 7.13 E-Plane Electric Field Pattern of 2-Element Antenna Array Structure at 10.6 GHz for the Switches are Up-State Case	95
Figure 7.14 H-Plane Electric Field Pattern of 2-Element Antenna Array Structure at 10.6 GHz for the Switches are Up-State Case	95
Figure 7.15 E-Plane Electric Field Pattern of 2-Element Antenna Array Structure at 15.9 GHz for the Switches are Down-State Case	96
Figure 7.16 H-Plane Electric Field Pattern of 2-Element Antenna Array Structure at 15.9 GHz for the Switches are Down-State Case	96
Figure B.1 Top view of the Tapered Anechoic Chamber in Aselsan Inc.	107
Figure B.2 Antenna Measurement Setup in Anechoic Chamber	108
Figure C.1 RO5880 High-Frequency Laminate Datasheet.....	109
Figure C.2 RO5880 High-Frequency Laminate Datasheet.....	110
Figure D.2 MICROSEMI MPV-2100 Varactor Diode Datasheet.....	111
Figure D.2 MICROSEMI MPV-2100 Varactor Diode Datasheet.....	112
Figure E.1 Up State Schematic Models of (a) Series SPST Switch (b) Shunt SPST RF MEMS Switch.....	113
Figure E.2 Down State Schematic Models of (a) Series SPST Switch (b) Shunt SPST RF MEMS Switch.....	113
Figure E.3 Schematic Model and Photograph of RADANT SPST RF MEMS Shunt Switch.....	114

CHAPTER I

INTRODUCTION

Antennas are crucial components of many systems such as radars, wireless communication systems, and remote sensing applications. There are different types of antennas that could satisfy the requirements of systems. For instance, traveling wave antennas are very suitable for radar applications due to their high directivity and side lobe control capabilities. Most of the time, to satisfy various system requirements, different antenna configurations are needed. At the basic antenna concept point of view, different system configurations need different antennas or large antenna units. Reconfigurable antenna concept adapts the antenna units depending on system configurations. Reconfiguration in antennas decreases the size of antenna units in systems and increases the operational capability of the antenna. Depending on system requirements; frequency, radiation pattern or polarization reconfigurations can be accomplished using electrical and mechanical mechanisms. Besides, planar surfaces are required to mount electrical reconfiguration components. Hence, microstrip antennas are good candidates for reconfigurable antenna applications.

In this thesis, three different reconfigurable antenna structures have been studied; beam-steerable meanderline antenna, polarization-agile meanderline antenna and dual-frequency slot-dipole array. Beam-steerable microstrip traveling wave antennas with varactor diodes have been analyzed, manufactured and tested. In addition, a polarization-agile meanderline array with RF MEMS (Radio Frequency MicroElectroMechanical Systems) switches has been designed. Lastly, frequency reconfigurable slot-dipole array has been designed and prototype structures have been manufactured and measured.

A detailed investigation of reconfigurability in antennas is presented in Chapter 2. Frequency, radiation pattern and polarization reconfigurable antennas are described and some examples are given. Furthermore, advantages and disadvantages of different reconfiguration mechanisms and methods are discussed.

General features of microstrip traveling wave antennas are given in Chapter 3. Electrical properties of different types of microstrip traveling wave antennas are explained. Since the main focus of the thesis is meanderline arrays, rest of the chapter is devoted to this subject. Radiation characteristics of the meanderline antenna are examined using different approaches and design parameters of meanderline array are obtained.

Chapter 4 describes design, simulation and measurement of the linearly polarized meanderline array operating at 10 GHz. According to design specifications, using commercial electromagnetic analysis tools Ansoft Designer and Ansoft HFSS, S-parameters, radiation pattern and surface current distributions of the meanderline array have been examined. Afterwards, the designed array has been manufactured and its S-parameters and radiation pattern have been measured. Measurement results in comparison with simulations are presented.

Chapter 5 presents a beam-steerable meanderline array operating at 10 GHz. In order to steer the beam to the specified direction, varactor diodes are employed on meanderline sections. Meanderline array loaded with varactor diodes has been manufactured. S-parameters and radiation pattern of the beam-steerable meanderline array have been measured at operating frequency.

In order to achieve more beam-steering, reflective type phase shifting mechanisms is proposed. Reflective type phase shifter is composed of a 3-dB branch-line coupler loaded with varactor diodes. This type of phase shifter has more phase tuning range than a single varactor diode. Analysis and simulations of meanderline array reflective type phase shifter are presented in this chapter.

A dual circularly polarized meanderline array is proposed in Chapter 7. Polarization of the proposed antenna can be altered by using SPDT (Single Pole Double Throw) RF MEMS switches between LHCP and RHCP.

A frequency reconfigurable slot dipole antenna array operating at X- and Ka- band is given in Chapter 7. Dual frequency operation of the slot dipole antennas is accomplished using SPST RF MEMS switches. MEMS switches are placed on the slot dipoles and electrical length of the dipoles changes with MEMS switches. Comparison of simulations and measurements is presented.

CHAPTER 2

RECONFIGURABLE ANTENNAS

Reconfigurable antennas have many advantages over traditional antenna elements and systems such as decreasing the size of the antenna units and increasing the degree of freedom in systems. Due to these benefits, reconfigurable antennas become more popular in many RF/microwave systems. Two different application areas can be considered while examining the functionality of the reconfigurable antennas. First application area is antenna arrays. Traditional antenna arrays have limited scan angle and frequency due to unit array elements. Unit elements of the array have fixed operating frequency and radiation pattern. Therefore, reconfigurability of the array unit elements enhances the operating frequency range of the array and beam scan angle. In addition to these, antenna arrays with fixed scan angle can be beam steerable with the advantage of reconfigurability. Second application area is portable wireless devices such as; cellular phones. These devices could demand different operating frequencies, diversity in transmission and reception. These properties can be satisfied by using different antennas in one system but due to size limitations of portable devices usually it is not desired. Main and effective solution to frequency and pattern reconfiguration is reconfigurable antennas. It is possible to obtain frequency or pattern reconfigurability by using reconfigurable antennas, also; the reconfigurability of the antennas increases the degree of freedom in the systems.

On the other hand, addition of the reconfigurability to the antenna units, increases complexity, requires signal processing and feedback circuitry. Reconfigurable antennas have more complicated fabrication processes compared to the traditional antennas.

In this chapter, first reconfigurability of the antenna's fundamental electrical

characteristics will be investigated and different reconfiguration mechanisms will be presented.

2.1 *Reconfigurability for Antenna Elements*

Antenna reconfigurability can be defined as the capacity to change the fundamental operating characteristics of the unit antenna element by means of electrical or mechanical [1]. For instance phasing of signals in an array in order to achieve beam forming or beam steering does not make the antenna reconfigurable because it does not change the fundamental electrical or mechanical characteristics of the antenna such as frequency response, radiation pattern etc. In addition to these if the antenna is said to be reconfigurable while its one of the electrical parameters changes, its other parameters should be kept constant.

Generally antennas are characterized with their input impedance characteristic over frequency (typically called the frequency response) and the radiation characteristic (or radiation pattern). Furthermore radiation pattern has the information about polarization, beam width, directivity, and beam scan angle of the antenna. Since the reconfigurability is the change of the fundamental operating characteristics, an antenna could be reconfigurable in frequency response, polarization or radiation pattern. In fact, radiation pattern is strongly correlated with frequency response in many antennas so there is a big challenge while constructing reconfigurable antennas. For example while designing a frequency reconfigurable antenna its radiation pattern should be identical for the entire band but it is not the case always. The following sections describe frequency response, polarization and radiation pattern reconfigurability of the antennas.

2.1.1 Frequency Reconfiguration

Frequency response of the antenna can be defined as its input impedance as a function of frequency. Antenna input impedance can be used to determine the

reflection coefficient (Γ) and related parameters, such as voltage standing wave ratio (VSWR) and return loss (RL), as function of frequency as given.

$$\Gamma = \frac{Z_{in}(\omega) - Z_0}{Z_{in}(\omega) + Z_0} \quad (2.1)$$

$$VSWR = \frac{1 + |\Gamma|}{1 - |\Gamma|} \quad (2.2)$$

$$RL = 20 \log |\Gamma| \quad (dB) \quad (2.3)$$

where $\omega = 2 * \pi * f$

Z_{in} : Input impedance of the antenna,

Z_0 : Characteristic impedance,

f : Operating frequency of the antenna.

Therefore in order to tune or reconfigure the antenna element its input impedance should be controlled in some manner. Input impedance in other means frequency response of the antenna elements can be changed continuously or discretely. Discretely tunable antennas have some kind of switching mechanisms that enable antennas to operate discrete frequency bands and continuous frequency tunable antennas has smooth transitions between operating bands without jump by using loading elements. Both discrete and continuous frequency tunable antennas have similar operation principle such as extending the effective length of the antenna element.

Frequency reconfiguration can be mainly applied to the resonant type antennas including linear antennas, slot antennas, and microstrip antennas. Effective electric length of these types of antennas can be tuned in order to obtain desired resonant frequencies [1]. There are different methods to achieve frequency reconfiguration:

First, it is possible to tune the antenna length by using switches. Dual frequency

operation of the antenna can be achieved by changing the electrical length of the antenna [2], [3], [4], [5]. An example of frequency reconfigurable antennas is 2-element frequency tunable slot dipole antenna array structure with MEMS switches as seen in Figure 2.1 [6]. The first resonance of the slot dipole antenna occurs when the switches are OFF. Electric length of the slot dipole antenna is decreased by making switches ON and operating frequency is shifted to higher frequency. Since the current distribution is same relative to the wavelength, radiation pattern does not change considerably. Design, prototype fabrication and measurements of 2-element frequency tunable slot dipole antenna array are in Chapter 7.

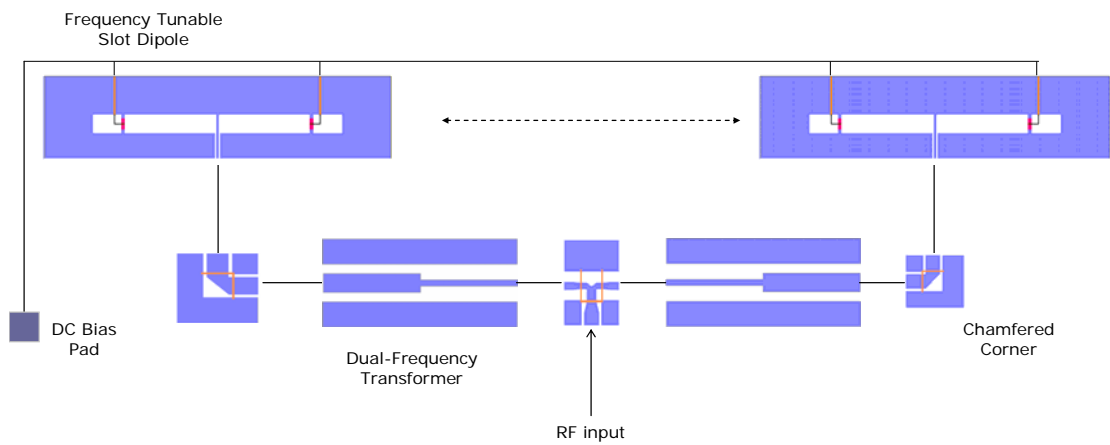


Figure 2.1 2-Element Frequency Tunable Slot Dipole Antenna Array Structure with MEMS Switches

Secondly, electrical length of the antenna can be changed by loading the antenna with variable capacitances. An example of the loaded antenna is a patch antenna with a stub loaded by RF MEMS variable capacitances [7]. The proposed antenna's operating frequency can be tuned between 15.75 GHz and 16.05 GHz.

2.1.2 Polarization Reconfiguration

Polarization of the antenna can be defined as the polarization of the wave transmitted (radiated) by the antenna. Electric field polarization of the antenna in the far field can be translated from the current flow on the antenna surface. Therefore, antenna polarization can be altered by controlling the current flow on the antenna surface. Polarization reconfigurations can occur between different types of linear polarizations, right and left hand circular polarizations, or between linear and circular polarizations. Polarization reconfiguration methods are generally similar with frequency reconfiguration methods although their implementations are different. Polarization reconfigurable antenna with a MEMS actuator has been introduced in [8]. The proposed antenna is a corner-fed nearly square patch antenna with two notches at two sides to generate 2 orthogonal modes. A MEMS actuator is placed on one of the notches and consists of a movable metal strip suspended over a metal stub. When the strip is suspended above the stub, the antenna has a circularly polarized pattern. When the actuator is down, the antenna is linearly polarized.

In addition, polarization reconfigurable circularly polarized meanderline array is designed and simulation results are given in Chapter 6. Antenna's polarization can be changed between RHCP (Right Hand Circularly Polarized) and LHCP (Left Hand Circularly Polarized) by using SPDT MEMS switches.

2.1.3 Radiation Pattern Reconfiguration

Antenna radiation pattern can be defined as a graphical representation of radiation properties of the antenna as a function of space coordinates. Radiation pattern is generally determined in the far field region and is represented as a function of directional coordinates. In fact radiation patterns are generally determined by the current distribution on the antenna structure. Therefore while achieving pattern

reconfigurability, it is hard to keep the frequency response of the antenna constant but not impossible. In order to achieve desired pattern reconfiguration magnitude and phase information of the current distribution should be analyzed in detail. After that for specific current distribution antenna structure is modified accordingly. While obtaining radiation pattern reconfigurability, to keep input impedance in other words frequency response more or less constant, tunable matching circuits can be used. In fact, reflector antennas and parasitically coupled antennas are more appropriate for pattern reconfiguration. Because reconfigured part is located in the feeding circuit so it is isolated from the radiated part. Therefore, it is easier to keep constant frequency response of the antennas.

There are many radiation pattern reconfigurable antennas reported in the literature [1], [9]. An example of a pattern reconfigurable antenna is planar ‘V’ antenna proposed in [11]. Arms of the ‘V’ antenna can be moved by using MEMS actuators, thus beam direction can be rotated or different beam shapes can be obtained. In addition, a rectangular spiral antenna with MEMS switches has been reported in [12]. Switches are located on the arm of the spiral. When these switches are activated, the spiral overall arm length is changed and as a result, its radiation beam direction is changed.

In Chapter 5, a beam-steerable meanderline array with varactor diodes is presented. Meanderline sections have been loaded with variable capacitors and beam direction is rotated. Design, manufacture and measurements of the proposed antenna are presented in Chapter 5.

2.2 Reconfiguration Mechanism for Antennas

Antenna reconfiguration can be accomplished by using number of mechanisms. Reconfiguration methods can be investigated in three groups: switches, diodes, mechanical and material changes. Each method has advantages and drawbacks and in some situations two or three methods are applied in the same design in order to achieved desired reconfiguration. In the following sections, a brief description will

be given for each method.

2.2.1 Switches

Switches are commonly used mechanisms in order to achieve any type of reconfigurations. There are many kinds of switches such as; optical switches, PIN diodes, FETs, and radio frequency micro electro mechanical system (RF MEMS) switches. Frequency tunability can be realized by changing the electrical length of the antenna by using switches. Also radiation pattern and polarization reconfiguration is obtained by controlling current distribution on the antenna surface using switches. Especially, pin diodes are preferable since they are easy to integrate and cost efficient. On the other hand, biasing circuits of the pin diodes has parasitic effects and has higher insertion loss compared to the RF MEMS switches. RF MEMS switches have low insertion, high linearity and low power consumption [13]. Besides, when the RF MEMS switches are fabricated on the same substrate with antenna it alleviates the packaging effects and other affects due to soldering and bonding [14].

In addition to these, optical switches have advantages over other kind of switches such as that can get rid of the some switch and bias line effects. In order to control the optical switches light from infrared laser diodes guided with fiber-optic cables can be used [15]. However, it should be noted that optical power used to activate the switches can affect the antenna gain and other parameters [16].

2.2.2 Variable Reactive Loading

Variable reactive loading is different from switch mechanism in a manner that it results in continuous reconfiguration while switches provide discrete changes. These continuous reconfigurations are commonly achieved by variable capacitor type mechanisms such as FETs, varactor diodes, RF MEMS variable capacitors. For instance, varactor diode capacitances change with respect to reverse applied voltage. By loading the antenna with tunable capacitance, it is possible to change its input

impedance and obtain frequency tunability. One example of the varactor loaded antenna is presented in [17]. In this structure, two varactor diodes have been connected between the main radiating edges of the antenna and the ground plane. With a reverse bias varying between 0 and 30 V, the varactors had capacitances between 2.4 and 0.4 pF. As the bias level changed, the capacitances at the edges of the patch tuned the electrical length of the patch. Continuous frequency tuning over a large band has been achieved.

Especially varactor diodes are packaged components and easy to integrate to the antenna elements. On the other hand biasing circuits of the varactor diodes can affect the electrical characteristics of the antenna. Hence, during the design of the antenna bias circuitry of the varactor diodes should be analyzed in detail.

In a similar manner, reactance of the FET components changes with applied voltage and this variable reactance can be used to tune the electrical length of the antenna or change the current phase and magnitude distribution of the antenna [18].

On the other hand tunable RF MEMS capacitors can also reduce parasitic effects, the losses, system size, and costs. A reconfigurable CPW-fed dual frequency rectangular slot antenna is given in [7]. In this structure, a rectangular slot antenna is integrated with MEMS cantilever type capacitors located on a stub. Capacitors are actuated by different voltage values and resonance frequency of the antenna can be changed.

2.2.3 Mechanical and Material Parameter Changes

Mechanical changes have more advantages over switches or variable reactive loading mechanisms because mechanical changes can create abrupt changes in frequency and radiation pattern reconfigurability. The main challenge using mechanical reconfiguration mechanisms is the actuation mechanism and the maintenance of other characteristics while changing the physical structure of the antenna abruptly [19], [20]. An example of mechanical changes is piezoelectric actuator systems which enable to control the distance between elements and makes possible to change

operating frequency or radiation pattern. It is stated that piezoelectric actuator systems changes other characteristics while achieving in one kind of reconfigurability [21].

Although it is known that current radiation characteristic of the antenna is dominantly determined by the conductor part of the antenna, it is possible to tune the antennas by changing material characteristics of substrates. For instance, ferroelectric materials relative permittivity can change with an applied static electric field and the permeability of the ferrite can change with an applied static magnetic field [22], [23], [24]. It is possible to change the effective length of the antennas by changing relative permittivity and permeability of the substrates. Also, the resonant current distributions on conductors can be arranged accordingly by changing permittivity and permeability of the ferrite or ferroelectric materials. Another example of mechanical reconfiguration mechanism is the electromagnetically actuated antenna proposed in [25]. By applying DC magnetic field, the patch can bend on the substrate surface at an angle which is called plastic deformation. The main advantage of changing characteristics of materials over other reconfiguration mechanisms is elimination of bias circuits commonly used for switches and variable reactive loading mechanisms. The main drawback of ferroelectric and ferrite materials is their high-conductivity resulting in high loss compared to other substrates and it decreases the efficiency of the antennas.

CHAPTER 3

TRAVELING WAVE ANTENNAS

Traveling wave antenna can be defined as an antenna whose conductors support a current distribution described by a traveling wave. It is possible to model a traveling wave antenna as a single wire transmission line (single wire over ground) which is terminated with a match load so no reflection at the end of the antenna as seen in Figure 3.1. Generally, the length of the transmission line is several wavelengths. Since, traveling wave antennas act as transmission line, they have constant input impedance over a very wide frequency range. On the other hand, their gain, efficiency and radiation pattern changes with frequency that limits operational bandwidth of the antennas.

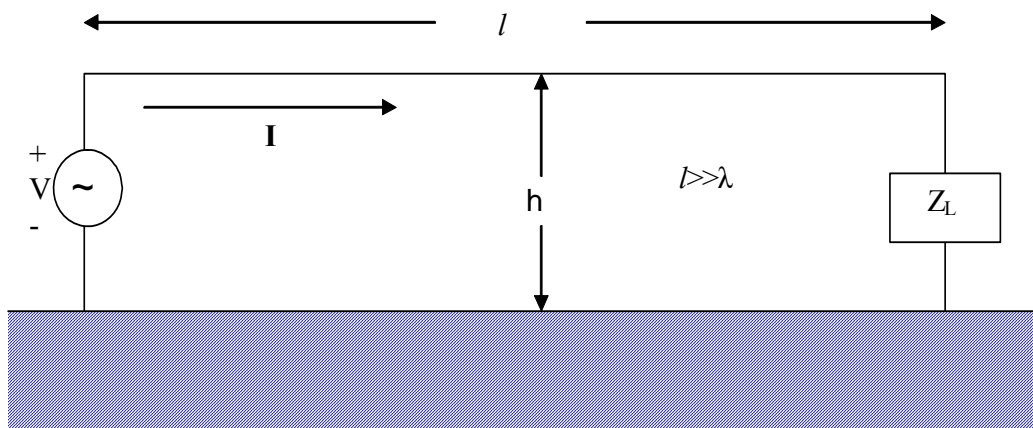


Figure 3.1 Single Wire Transmission Line over Ground Terminated with a Matched Load

Traveling wave antennas can be classified as a fast wave when the phase velocity of the wave is greater than the velocity of the light in free space and ($v_p / c > 1$) and slow wave if its phase velocity is equal or smaller than the velocity of light c in free space ($v_p / c \leq 1$). (Phase velocity is defined as, $v_p = \omega / k$, where ω is wave angular frequency, k is wave phase constant)

In general, there are two types of traveling wave antennas. First one is called leaky wave that couples power, either continuously or discretely, in a small increments per unit length from a traveling wave structure to free-space. An example of leaky wave antennas is a slotted rectangular waveguide antenna [26], [27]. Most of the leaky wave antennas are fast wave structures, they continuously loose energy due to the radiation and the fields decay along the structure in the direction of wave travel.

Second type of traveling wave antennas is surface wave antennas. Surface wave antennas radiate power from discontinuities in the structure that interrupt a bound wave on the antenna surface. Phase velocity of the traveling wave on the surface wave antenna is commonly equal to or less than velocity of light so that these antennas are also called slow wave structures. Radiation of the surface wave antennas are mainly occurs from discontinuities, curvatures, and non-uniformities. Discontinuities on the antenna surface can be discrete or distributed. In fact, most of the surface wave antennas are end-fire or near end-fire radiators. Practical configurations of surface wave antennas are curved, modulated structures, line and planar surfaces [29], [30].

3.1 Microstrip Traveling Wave Antennas

Printed microstrip antennas have many applications in satellite communications, radars, remote sensing, missile telemetry and other biomedical instruments. The advantages of microstrip antennas compared to other type of antennas are their light weight, low profile, easy to mount on systems and compatible with modular designs such as reconfiguration mechanisms; switches, phase shifters etc.

Microstrip traveling wave antennas have the advantages of both traveling wave antennas and microstrip antennas. Microstrip traveling wave antennas are slow wave structures. They consist of curved or chain shaped periodic conductors or an ordinary long TEM line on a substrate backed by a ground plane [28]. Traveling wave array structures are terminated with a matched load. There are number of microstrip configurations that have been used in the design of traveling wave antennas. These antennas are briefly described in this section.

Chain Antenna

Chain antenna is composed of rectangular loops which are chain shaped patterns on the grounded dielectric slab. End of the chain antenna is terminated with matched load as seen in Figure 3.2. Typically, the width of the rectangular loop, $2T$, is in the order of one wavelength and the separation between chains, S , is slightly less than half a wavelength [29]. In order to obtain propagation along the chain antenna without reflections, the characteristic impedance of the line connecting the rectangular loops should be half of the impedance of the loop line and the effects of the discontinuities should be minimized [34].

As the wave propagates along the structure, the current along the chain structure attenuates due to radiation. The radiation occurs from the ‘S’ parts of the chain antenna which are parallel to the antenna axis whereas, radiation occurs from the T parts cancels each other since they have equal but opposite magnitudes. Therefore, the polarization of the chain antenna is parallel to the chain structure.

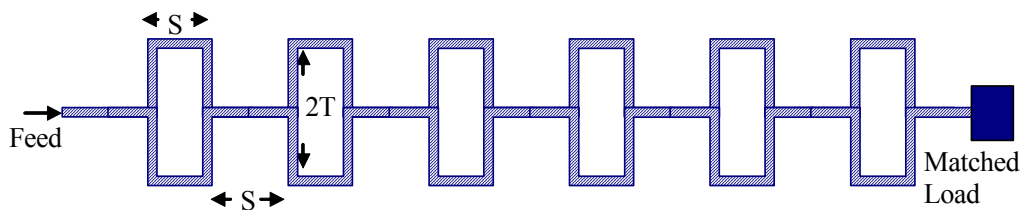


Figure 3.2 Rectangular Loop Type Microstrip Chain Antenna

TEM Line Antenna

TEM antenna is a microstrip type traveling wave antenna supporting TE_{01} coupled to a TEM mode along a microstrip line. Radiation mainly occurs at the frequencies not far above the cut-off frequency of the TE_{01} - mode since it is very loosely coupled to the line. As seen from Figure 3.3, the antenna is fed asymmetrically to excite the first higher order mode [29]. Also, it is possible to insert metal post on the antenna or create small slots on the antenna surface in order to suppress the fundamental mode. In addition, a matching transformer is used to match the antenna to the feed line.

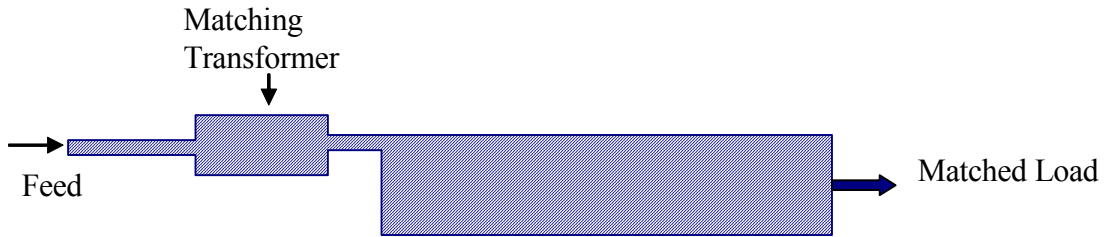


Figure 3.3 TEM Line Antenna Geometry

Series Microstrip Patch Antenna

The series microstrip patch traveling wave antenna consists of patch elements cascaded by high impedance transmission lines. Array of cascaded microstrip patches are terminated with a matched load as seen in Figure 3.4. The array input impedance is approximately same as the impedance connecting the elements because the internal reflections within the array add randomly in phase at the feed. In addition, series microstrip patch traveling wave antenna is a broadband structure [29].

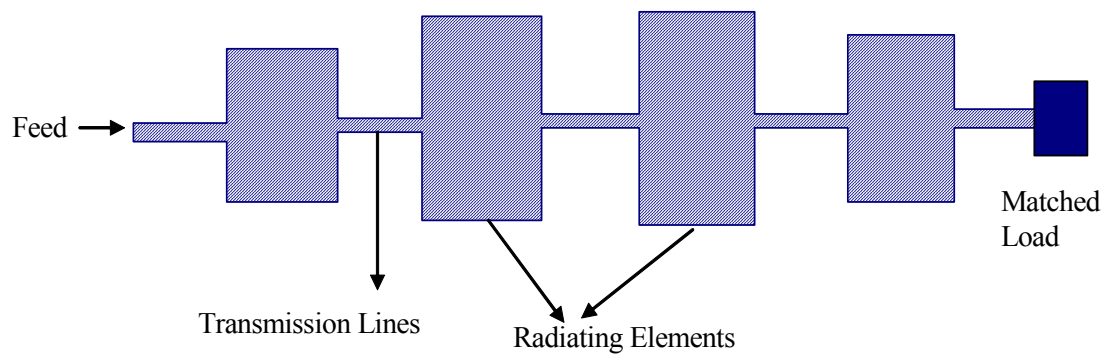


Figure 3.4 A Series Microstrip Patch Traveling-Wave Antenna Configuration

Comblne Antenna

Another type of traveling wave antenna is a comb-line antenna shown in Figure 3.5. The antenna radiates from the open ended stubs or fingers. Stub lengths are approximately half a wavelength long, so that the radiation conductance is directly transferred to the feed line. Since the radiation conductance symbolizes the loading on the line, in order to obtain desired aperture distribution, the widths of the stubs are selected accordingly [29].

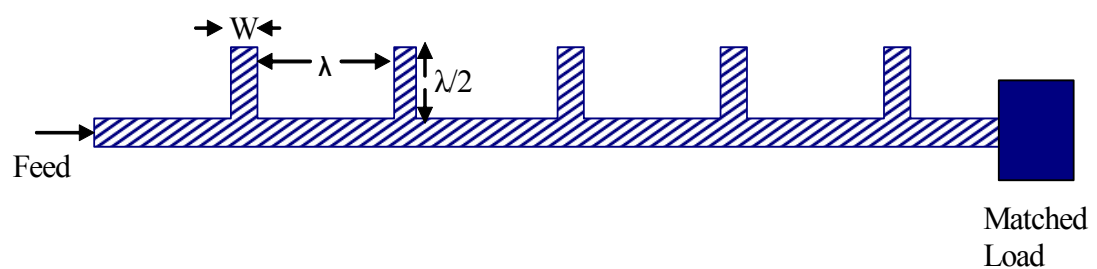


Figure 3.5 Comblne Microstrip Traveling Wave Antenna

Franklin Type Antenna

Franklin type antenna configuration is shown in Figure 3.6. The antenna composed

of 50Ω microstrip line with a Franklin-antenna shape and open end of the antenna is terminated with a matched load or open circuit [29].

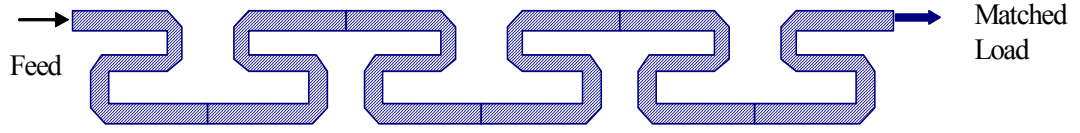


Figure 3.6 Geometry of a Franklin-Type Microstrip Traveling Wave Antenna

3.2 Meanderline Arrays (*Rampart Antenna*)

Meanderline arrays are another type of microstrip traveling wave antennas. Meanderline arrays have some advantages compared to other types of printed antennas, for instance their polarization and beam direction can be controlled by simply adjusting the spacing between the bends. Due to these features, meanderline arrays are good candidates of radar applications.

Meanderline arrays consist of a meandering microstrip line with a matched load at the end of the antenna as shown in Figure 3.7. A meanderline array composed of unit cells and each unit cell has six or four corners depending on the antenna polarization requirements as shown in Figure 3.8 (a) and (b) respectively. According to [28], radiation of the meanderline array mainly occurs from the right angle bends. In order to reduce the right-angled discontinuity susceptance and return loss, right-angled bends are chamfered. The radiation direction and the polarization can be controlled with the length, width and the period of the rampart cells. In the case of four cornered rampart cell, polarization radiated by the cell is controlled by two lengths s and d , and the third length l is used to control the required array scan angle.

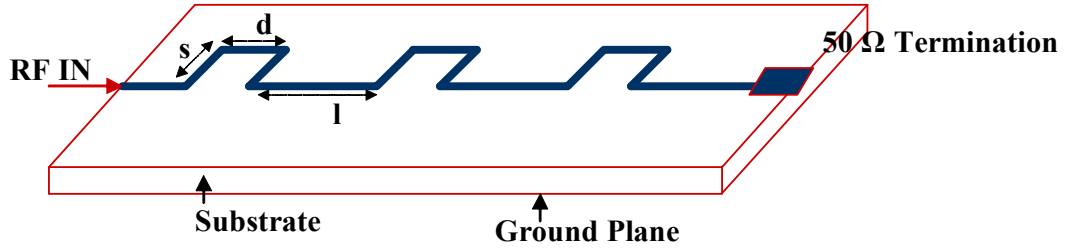


Figure 3.7 A Representation of Meanderline Array Section

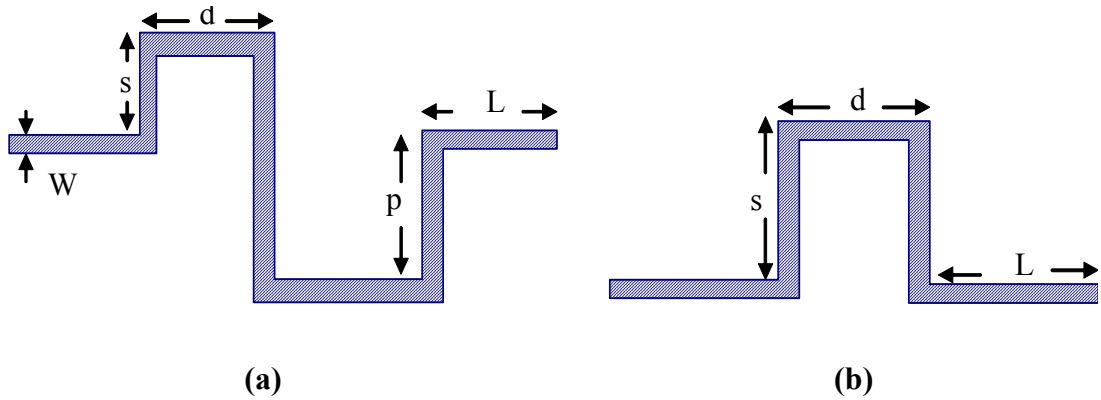


Figure 3.8 Unit Cells of Different Types of Meanderline Array

(a) Six Cornered Meanderline Cell for Arbitrary Polarization

(b) Four Cornered Meanderline Cell for Linear or Circular Polarization

3.2.1 Radiation Mechanism of the Unit Meanderline Cell

As mentioned above radiation of the meanderline mainly occur from the right-angled bends. It is possible to model these right angled bends as magnetic current elements as seen in Figure 3.9(a), Since the current on the meanderline antenna travels a shorter path at inside edge than the outside edge, it creates an imbalance magnetic current [28]. Thus, the four cornered meanderline antenna cell can be modeled as an array of magnetic current elements which are fed in a phase progression for a traveling-wave array.

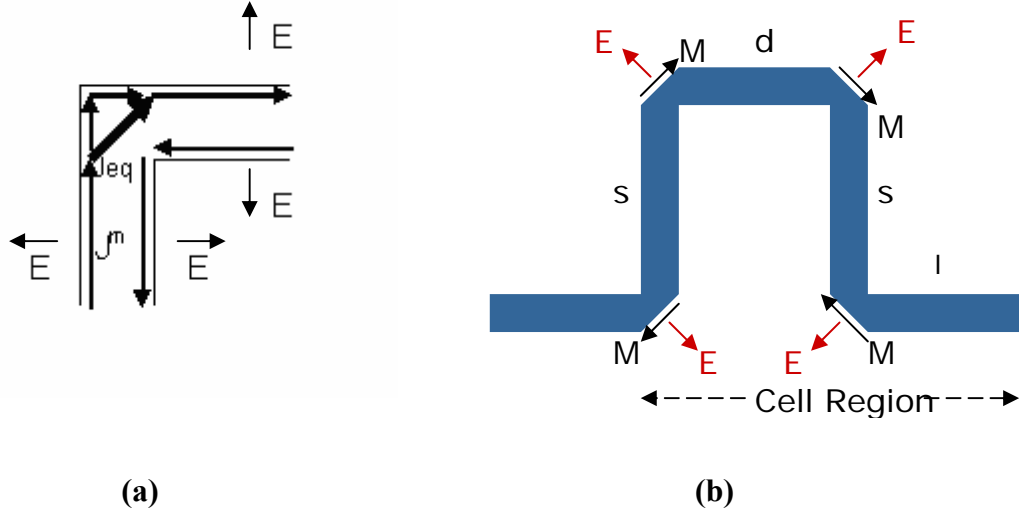


Figure 3.9
(a) Equivalent Current Source Distribution at the Right Angle Bend
(b) Equivalent Model of Four Cornered Meanderline Cell

Since quasi TEM mode is excited on the meanderline structure as seen from Figure 3.9 (a), the E-field components on the straight lengths are oppositely directed and tend to cancel each other's radiation. As shown in Figure 3.9 (b) radiated electric field is diagonally placed to the corner and magnetic field is perpendicular to the electric field. The electric field and magnetic current distribution of the meanderline cell can be expressed in terms of electric and magnetic field elements.

$$\bar{J}^e = \hat{n} \times \bar{H} \quad (3.1)$$

$$\bar{J}^m = \bar{E} \times \hat{n} \quad (3.2)$$

where \hat{n} is unit normal outward from the meanderline .

In Equations 3.1 and 3.2 electric field E and magnetic field H are associated with electric and magnetic type sources (\bar{J}^e and \bar{J}^m) on the meanderline sections. Contribution of electric and magnetic current elements to the total radiation is equal [28], therefore while analyzing the radiated field only magnetic current element has

been used. Therefore, meanderline array is represented with magnetic current elements fed in a phase progression. Also, it is assumed that coupling due to surface waves and attenuation of the traveling wave on the line is negligible.

Formulation of the total radiated fields of the meanderline array is presented below:

As shown in Figure 3.10 antenna is placed on the y-z plane and magnetic current elements are represented with hertzian magnetic dipoles at the corners. Distance between magnetic current elements is equal to the length of the meander sections. Total magnetic current of the unit cell is equal to the summation of hertzian magnetic dipoles. First current element is located at the origin with zero phase and phase shift and the position of the other current vectors are written in terms of the first one.

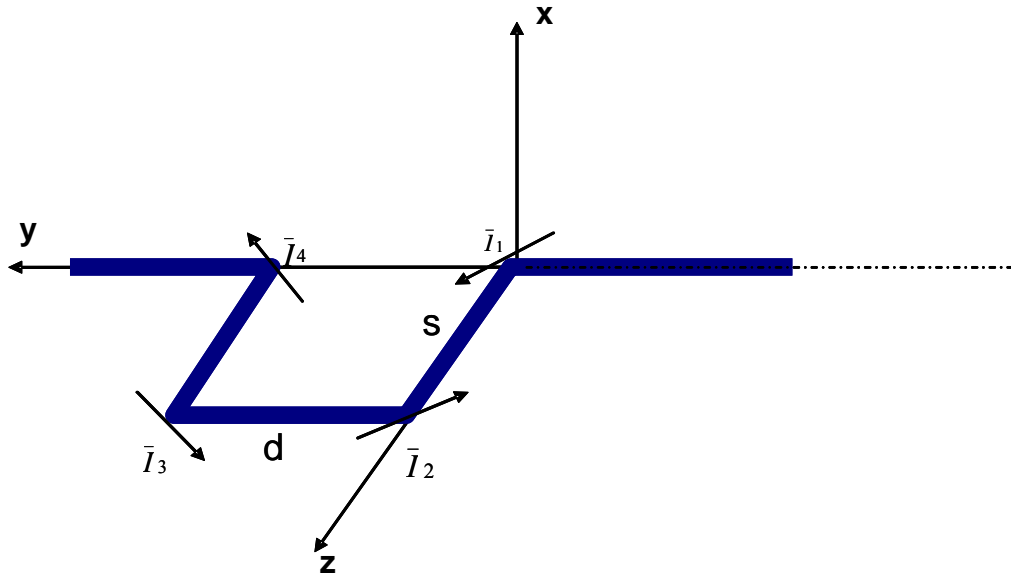


Figure 3.10 Magnetic Current Vectors on Meander Line Unit Cell

In order to calculate E and H fields of the meanderline array, it is possible to use induction equivalent modeling. It is assumed that the dominant part of the magnetic current J^m resides only in the front face of the conductor. From the image theory total magnetic current equals to $2J^m$. Therefore, by using $2J^m$ formulation given in

Equation 3.3, vector potential can be derived. J^m can be written in terms of current elements ($\bar{I}_1, \bar{I}_2, \bar{I}_3, \bar{I}_4$) defined at the corners of the meanderline cell.

$$\bar{A}_m = \frac{1}{4\pi} \int_V 2\bar{J}^m(x', y', z') \frac{e^{-jk_0 R}}{R} dV' \quad (3.3)$$

\bar{A}_m can be decomposed into $\bar{A}_m = \bar{A}_1^m + \bar{A}_2^m + \bar{A}_3^m + \bar{A}_4^m$

$$\bar{A}_1^m = (\hat{a}_y + \hat{a}_z) \frac{I}{\sqrt{2}} \frac{1}{2\pi} \frac{e^{-jk_0 r}}{r} \quad (3.4-a)$$

$$\bar{A}_2^m = (-\hat{a}_y - \hat{a}_z) \frac{I}{\sqrt{2}} \frac{1}{2\pi} \frac{e^{-jk_0 r}}{r} e^{-jk_0 s \sin \theta \sin \phi} e^{-j\beta s} \quad (3.4-b)$$

$$\bar{A}_3^m = (-\hat{a}_y + \hat{a}_z) \frac{I}{\sqrt{2}} \frac{1}{2\pi} \frac{e^{-jk_0 r}}{r} e^{-jk_0 s \sin \theta \sin \phi} e^{-jk_0 d \cos \theta} e^{-j\beta(s+d)} \quad (3.4-c)$$

$$\bar{A}_4^m = (\hat{a}_y - \hat{a}_z) \frac{I}{\sqrt{2}} \frac{1}{2\pi} \frac{e^{-jk_0 r}}{r} e^{-jk_0 d \cos \theta} e^{-j\beta(2s+d)} \quad (3.4-d)$$

where I equals to current flowing on each dipole.

In order to write magnetic vector potential in spherical coordinates $\hat{a}_x, \hat{a}_y, \hat{a}_z$ are written in terms of $\hat{a}_r, \hat{a}_\theta, \hat{a}_\phi$ as shown in Equations 3.5 (a-b).

$$\hat{a}_y - \hat{a}_z = (\sin \theta \sin \phi - \cos \theta) \hat{a}_r + (\cos \theta \sin \phi - \sin \theta) \hat{a}_\theta + \cos \phi \hat{a}_\phi \quad (3.5-a)$$

$$\hat{a}_y + \hat{a}_z = (\sin \theta \sin \phi + \cos \theta) \hat{a}_r + (\cos \theta \sin \phi + \sin \theta) \hat{a}_\theta + \cos \phi \hat{a}_\phi \quad (3.5-b)$$

Therefore, in spherical coordinates at the far field \bar{A}_m can be written as in Equations

3.6 and 3.7 (a-c).

$$A^m = A_r^m \hat{a}_r + A_\theta^m \hat{a}_\theta + A_\phi^m \hat{a}_\phi \quad (3.6)$$

$$A_r^m = \frac{I}{\sqrt{2}} \frac{1}{2\pi} \frac{e^{-jk_0 r}}{r} \begin{pmatrix} (\sin \theta \sin \phi - \cos \theta) \\ -(\sin \theta \sin \phi - \cos \theta)(e^{-jk_0 s \sin \theta \sin \phi} e^{-j\beta s}) \\ +(\sin \theta \sin \phi + \cos \theta)(e^{-jk_0 s \sin \theta \sin \phi} e^{-jk_0 d \cos \theta} e^{-j\beta(s+d)}) \\ -(\sin \theta \sin \phi + \cos \theta)e^{-j\beta(2s+d)} \end{pmatrix} \quad (3.7-a)$$

$$A_\theta^m = \frac{I}{\sqrt{2}} \frac{1}{2\pi} \frac{e^{-jk_0 r}}{r} \begin{pmatrix} (\cos \theta \sin \phi - \sin \theta) \\ -(\cos \theta \sin \phi - \sin \theta)(e^{-jk_0 s \sin \theta \sin \phi} e^{-j\beta s}) \\ +(\cos \theta \sin \phi + \sin \theta)(e^{-jk_0 s \sin \theta \sin \phi} e^{-jk_0 d \cos \theta} e^{-j\beta(s+d)}) \\ -(\cos \theta \sin \phi + \sin \theta)e^{-j\beta(2s+d)} \end{pmatrix} \quad (3.7-b)$$

$$A_\phi^m = \frac{I}{\sqrt{2}} \frac{1}{2\pi} \frac{e^{-jk_0 r}}{r} \begin{pmatrix} (\cos \phi) \\ -(\cos \phi)(e^{-jk_0 s \sin \theta \sin \phi} e^{-j\beta s}) \\ +(\cos \phi)(e^{-jk_0 s \sin \theta \sin \phi} e^{-jk_0 d \cos \theta} e^{-j\beta(s+d)}) \\ -(\cos \phi)e^{-j\beta(2s+d)} \end{pmatrix} \quad (3.7-c)$$

By using Far Field approximations, E-field at the far field can be derived.

$$\bar{E}_r \approx 0 \quad (3.8-a)$$

$$\bar{E}_\theta = -j\omega \bar{A}_\theta^m \quad (3.8-b)$$

$$\bar{E}_\phi = -j\omega \bar{A}_\phi^m \quad (3.8-c)$$

In order to obtain the azimuth pattern (E-plane) of the meanderline unit cell, take the $\phi=0$ cut plane

So;

$$\bar{E}_\theta = -j\omega \bar{A}_\theta^m \Big|_{\phi=0} \quad (3.9-a)$$

$$E_{\theta} = j\omega \frac{I}{\sqrt{2}} \frac{1}{2\pi} \frac{e^{-jk_0 r}}{r} \sin \theta \left(1 - e^{-j\beta s} - e^{-jk_0 d \cos \theta} e^{-j\beta(s+d)} + e^{-j\beta(2s+d)} \right) \quad (3.9-b)$$

$$\bar{E}_{\phi} = -j\omega \bar{A}_{\phi}^m \Big|_{\phi=0} \quad (3.10-a)$$

$$E_{\phi} = -j\omega \frac{I}{\sqrt{2}} \frac{1}{2\pi} \frac{e^{-jk_0 r}}{r} \left(1 - e^{-j\beta s} + e^{-jk_0 d \cos \theta} e^{-j\beta(s+d)} - e^{-j\beta(2s+d)} \right) \quad (3.10-b)$$

After \bar{E}_{θ} , \bar{E}_{ϕ} values of the meanderline unit cell is calculated as in Equations 3.9 and 3.10, array theory is applied in order to calculate the array pattern of the meanderline array.

$$\bar{E}_{tot} = \bar{E}_{unit} * AF \quad (3.11)$$

where \bar{E}_{tot} is the total electric field of the meanderline array and \bar{E}_{unit} is the radiation pattern of the meanderline array unit cell. AF is the array factor and can be defined as;

$$AF = \frac{\sin N \frac{\psi}{2}}{N \sin \frac{\psi}{2}} \quad (3.12)$$

Where N is the number of elements in the array and

$$\psi = k_0(d + L)\cos \theta - (2s + d + L)\beta$$

$$\beta = \frac{2\pi}{\lambda_g}$$

In conclusion, radiated E-Field at $\phi=0$ plane (E-plane) at the far field for meanderline array has been calculated as;

$$\bar{E}_{tot} = \frac{\sin N \frac{\psi}{2}}{N \sin \frac{\psi}{2}} j \omega \frac{I}{\sqrt{2}} \frac{1}{2\pi} \frac{e^{-jk_0 r}}{r} \left[\begin{aligned} &(\sin \theta (1 - e^{-j\beta s} - e^{-jk_0 d \cos \theta} e^{-j\beta(s+d)} + e^{-j\beta(2s+d)})) \bar{a}_\theta \\ &+ (-1 + e^{-j\beta s} - e^{-jk_0 d \cos \theta} e^{-j\beta(s+d)} + e^{-j\beta(2s+d)}) \bar{a}_\phi \end{aligned} \right] \quad (3.13)$$

Polarization of the Meanderline Array

Total radiated electric field of the four corner meanderline array is calculated in the previous section. As seen from Equation 3.14, far field E-pattern of the antenna is controlled by s and d parameters of the unit meanderline cell. Polarization of the array can be analyzed in terms of the diagonally polarized fields and in this case, it is convenient to analyze the polarization of the meanderline array with ratio of E_θ and E_ϕ .

$$\frac{E_\theta}{E_\phi} = \frac{\sin \theta (1 - e^{-j\beta s} - e^{-jk_0 d \cos \theta} e^{-j\beta(s+d)} + e^{-j\beta(2s+d)})}{(-1 + e^{-j\beta s} - e^{-jk_0 d \cos \theta} e^{-j\beta(s+d)} + e^{-j\beta(2s+d)})} \quad (3.14)$$

In [29], it is stated that the radiation on the meanderline cell is diagonally polarized as seen from Figure 3.11.

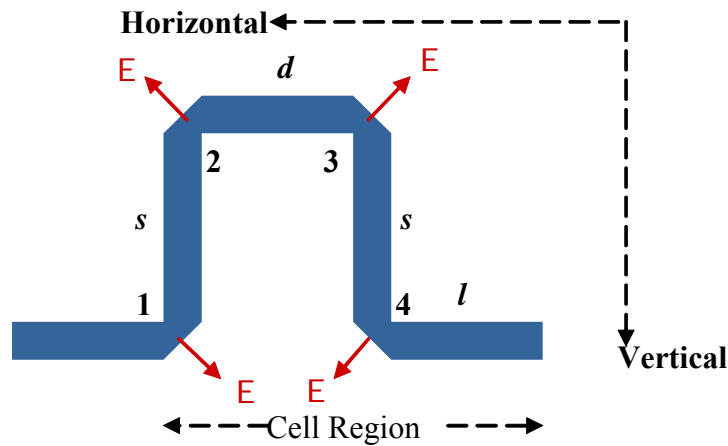


Figure 3.11 Diagonally Polarized E-Field Vectors of Meanderline Cell

The radiation from each bend in the cell can be decomposed into horizontal and vertical components; summation of these vertical and horizontal components gives the polarization of the meanderline array. While analyzing the polarization of the meanderline cell; vertical and horizontal components of the total radiated field at the first corner of the meanderline cell can be written in terms of P, where P is the radiation polarization field strength, after that, radiation components of other corners is calculated in terms of first corner, according to distance between radiation components i.e corners and direction of radiation vector at that corner.

Table 3.1 Polarization Components of a Meanderline Antenna

(a) Circular Polarization Case with $s=\lambda/2$, $d=\lambda/4$, and $l=3\lambda/4$ Dimensions

Bend	Polarization Component	
	Vertical	Horizontal
1	$P/\sqrt{2}$	$-P/\sqrt{2}$
2	$P/\sqrt{2}$	$-P/\sqrt{2}$
3	$jP/\sqrt{2}$	$jP/\sqrt{2}$
4	$jP/\sqrt{2}$	$jP/\sqrt{2}$
Total	$\sqrt{2}P(1+j)$	$j\sqrt{2}P(1+j)$

(b) Vertical Polarization Case with $s=\lambda/4$, $d=\lambda/4$ and $l=\lambda/4$ Dimensions

Bend	Polarization Component	
	Vertical	Horizontal
1	$P/\sqrt{2}$	$-P/\sqrt{2}$
2	$-jP/\sqrt{2}$	$jP/\sqrt{2}$
3	$P/\sqrt{2}$	$P/\sqrt{2}$
4	$-jP/\sqrt{2}$	$-jP/\sqrt{2}$
Total	$P(1-j)\sqrt{2}$	0

As seen from Table 3.1 (a) total vertical and horizontal components of the

meanderline cell have a $\pi/2$ phase difference and thus produce circular polarization. Similarly, as seen from Table 3.1 (b) vertical polarization can be achieved with $s=\lambda/4$, $d=\lambda/4$ and $l=\lambda/4$ dimensions. In addition, $s=2\lambda/3$, $d=\lambda/3$ and $l=\lambda/3$ provides horizontal polarization.

3.2.2 Lumped Approximate Network Model of the Meanderline Cell

In order to complete the electrical investigation of the meanderline array, a lumped approximate model of the meanderline is presented. This network model is developed in [28] by using two different methods, ‘Transmission line Approach’, and ‘Two port Network Representation’. It is possible to calculate the input VSWR from the equivalent circuit representation. As shown from Figure 3.12, right angle bend of the meanderline element can be modeled with reactive elements, X_L , X_c , and the radiation conductance of the bend is represented with G . Equations of X_L , X_c and G are given in Equations 3.15, 3.16 and 3.17.

$$G = \frac{1}{90} \left(\frac{l}{\lambda_0} \right)^2 \quad (3.15)$$

where l is the length of the magnetic current element and approximated as $l = \sqrt{2}W_{eq}$, W_{eq} is the equivalent width of the microstrip line and is given.

$$W_{eq} = \frac{120\pi h}{Z_c \sqrt{\epsilon_e}} \quad (3.16)$$

where h is the height of the dielectric, Z_c is the characteristic impedance of the antenna and ϵ_e is the effective dielectric constant.

$$X_L = \frac{W_{eq}}{\lambda_g} \left(1.756 + 4 \left(\frac{W_{eq}}{\lambda_g} \right)^2 \right) \quad (3.17)$$

$$X_C = -0.0865 \left(\frac{W_{eq}}{\lambda_g} \right) \quad (3.18)$$

where λ_g is the guided wavelength.

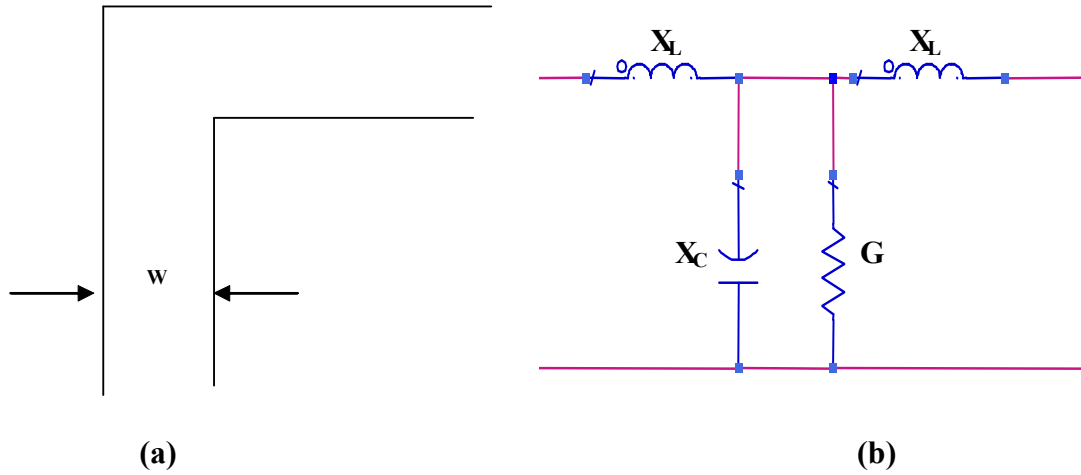
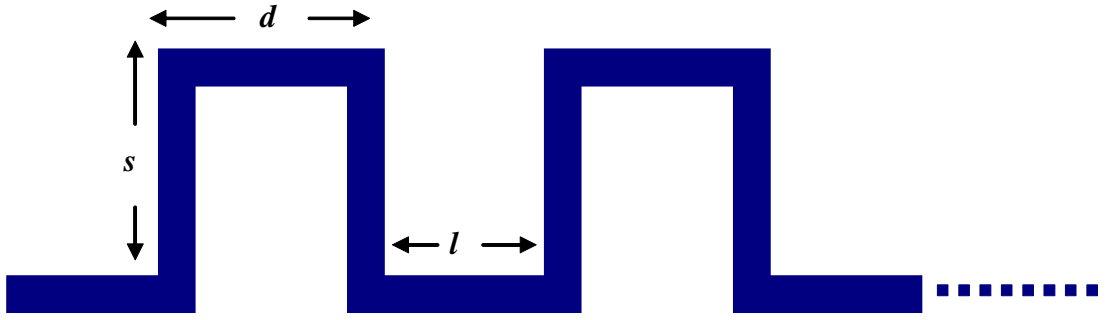
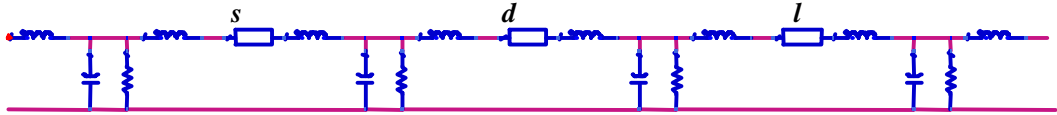


Figure 3.12
(a) Right Angle Bend of Meanderline
(b) Equivalent Circuit of Right Angle Bend

Overall meanderline array is composed of right angle bends and transmission lines. Therefore, according to the lumped equivalent network model overall meanderline array structure can be represented with right angled bend equivalent circuits cascaded with transmission lines that have similar lengths and impedance with microstrip lines of the meanderline array. Overall circuit of the meanderline array is shown in Figure 3.13.



(a)



(b)

Figure 3.13

(a) Four Cornered Meanderline Array

(b) Equivalent Circuit Model of Four Corner Meanderline Array

Presented circuit model is an approximation to the meanderline array and can be used only VSWR analysis of the antenna. In order to obtain more realistic model, it is better to use full-wave EM simulators throughout the design of the antenna.

To sum up, electrical characteristics; radiation mechanisms, radiation pattern, polarization and lumped equivalent model of the meanderline array is analyzed in detail. It could be observed that s and d parameters of the meanderline array controls the polarization of the unit meanderline element and direction of the radiation depends on distance between unit cells i.e l parameter. In addition to these, as verified from total radiation pattern formulation of the meanderline array and the theory of traveling wave arrays, increasing number of elements in the array increases

directivity and efficiency because if the number of elements increases less power is dissipated at the load. Also, when the number of elements increases, side lobe levels of the antenna decreases since array elements are not fed uniformly.

CHAPTER 4

DESIGN OF LINEARLY POLARIZED TRAVELLING WAVE MEANDERLINE ARRAY

In the preceding section practical and theoretical background of four-corner meanderline has been investigated. By using the formulations and technical investigations, a linearly polarized traveling wave meanderline array operating at X-band has been studied. In this chapter, design, fabrication and the measurement procedures of the antenna have been presented in detail.

4.1 Design Specifications

Design specifications of linearly polarized traveling wave meanderline array for X-band applications are summarized below;

Operating frequency of the meanderline array is set to 10 GHz that is in X-band. In fact, one should be aware of that traveling wave antennas have very narrow bandwidth because when frequency sweeps electrical length between elements varies and electrical characteristics of the antenna i.e. polarization and beam scan angle changes.

Polarization of the meanderline array is set vertically polarized in order to receive both right and left hand circularly polarized fields.

Main beam direction of the meanderline array is set to 30° and antenna parameters are calculated according to beam scan angle.

Input impedance of the array is taken as $50\ \Omega$ in order to make the antenna

compatible with connectors and measurement systems.

Beam width of the meanderline array is expected to be 8° in Co-polarized plane and side lobe levels are below -13 dB. In fact, theoretically, it is stated in [28] that for uniform illumination of the meanderline array side lobe levels are around -13 dB and in the case of non-uniform illumination, side lobe levels decrease below -13 dB.

An initial design has been performed by using the formulations derived in the 3rd Chapter to satisfy the design requirements. Then full-wave EM (Electromagnetic) simulations have been performed to finalize the design.

4.2 Initial Design

Before theoretical analysis substrate of the antenna array has been taken under consideration. Many substrates do not operate properly at high frequencies and their performances degrade with increasing frequency. ROGERS 5880 Duroid has very low dissipation factor at high frequencies. According to test data sheet at 10 GHz its maximum dissipation factor equals to 0.0015 that is very low compared to the other substrates. Due to all these reasons, 15 mil ROGERS 5880 Duroid with $\frac{1}{2}$ OZ. copper thickness has been used during design of the meanderline array. Dielectric constant (ϵ_r) of the substrate equals to 2.2.

Derivation of Microstrip Parameters

It is stated in the specification that the input impedance of the antenna and characteristic impedance of the meanderline sections will be equal to 50Ω . In order to calculate the microstrip line parameters it is possible to use theoretical formulas given in Appendix A or ADS (Advanced Design System) which is an electromagnetic simulator.

Effective dielectric constant and the width of the microstrip line are calculated using “Line Calc” in ADS. In addition, guided wavelength is computed in order to use in calculating dimensions of the meanderline array. Calculated values are presented

below;

Effective Dielectric Constant; $\epsilon_e = 1.836$

Guided Wavelength; $\lambda_g = 22.14$ mm

50 Ω microstrip line width $w = 1.17$ mm

Computing Parameters of Meanderline Array

In order to satisfy the specifications about polarization and radiation characteristics, initially, dimensions of the meanderline cell which defines the polarization of the antenna should be estimated. Afterwards, direction of the beam, beamwidth and side lobe levels are controlled by the array of meanderline cells and other design parameters are controlled by array formulations.

Polarization: As explained in Section 3.2.1 the polarization of the meanderline array can be investigated using vector addition of magnetic current elements at the corners of the meanderline cell. So, using Table 3.2.2, s and d values of the meanderline cell has been figured out $\lambda_g/4$. Since λ_g is derived as 22.14 mm s and d values equals to 5.535 mm.

Main Beam Scan Angle: Direction radiation of the meanderline array is controlled by the sections of the meanderline array as seen from Equation 4.1.

$$\psi = k_0(d + L)\cos\theta - (2s + d + L)\beta \quad (4.1)$$

where $k_0 = \frac{2\pi}{\lambda_0}$ and $\beta = \frac{2\pi}{\lambda_g}$

Array factor takes its maximum value when $\psi = 2n\pi$ ($n=0,1,2,\dots$) so for a desired beam direction, it is possible to calculate s , d or l parameters when two of the parameters given.

For s and d values found from polarization calculations; l value of the antenna is

calculated as;

$$l=5.522\text{mm}$$

Meanderline array composed of 8 elements satisfies the beamwidth considerations.

In fact, during theoretical calculations, it is assumed that signal traveling on the meanderline array does not attenuate; therefore each magnetic current element has the same magnitude. In real case, wave traveling on the meanderline array attenuates so each radiation element of the meanderline array has different magnitudes. Final design parameters are obtained by performing full wave electromagnetic simulations using Ansoft Designer V2 and HFSS V10.

4.3 Full-wave EM Simulations

Throughout the simulations of meanderline array, commercial software programs; Ansoft Designer and Ansoft HFSS have been used. Each program uses different numerical tools and has advantages and disadvantages according to the application.

Ansoft Designer is a full-wave EM simulator based on Method of Moments and very efficient at microstrip antenna analysis. It is possible to insert N-port networks with S-parameters into the structure that will be analyzed. This property has been used during beam steerable meanderline antenna design. The other full wave EM analysis tool used in this thesis study is Ansoft HFSS which based on FEM (Finite Element Method). Designer can analyze only 2D or 2.5 D structures whereas HFSS can simulate 3D structures.

Linearly polarized meanderline array has been optimized using Ansoft Designer; schematic model of the array has been shown in Figure 4.1.

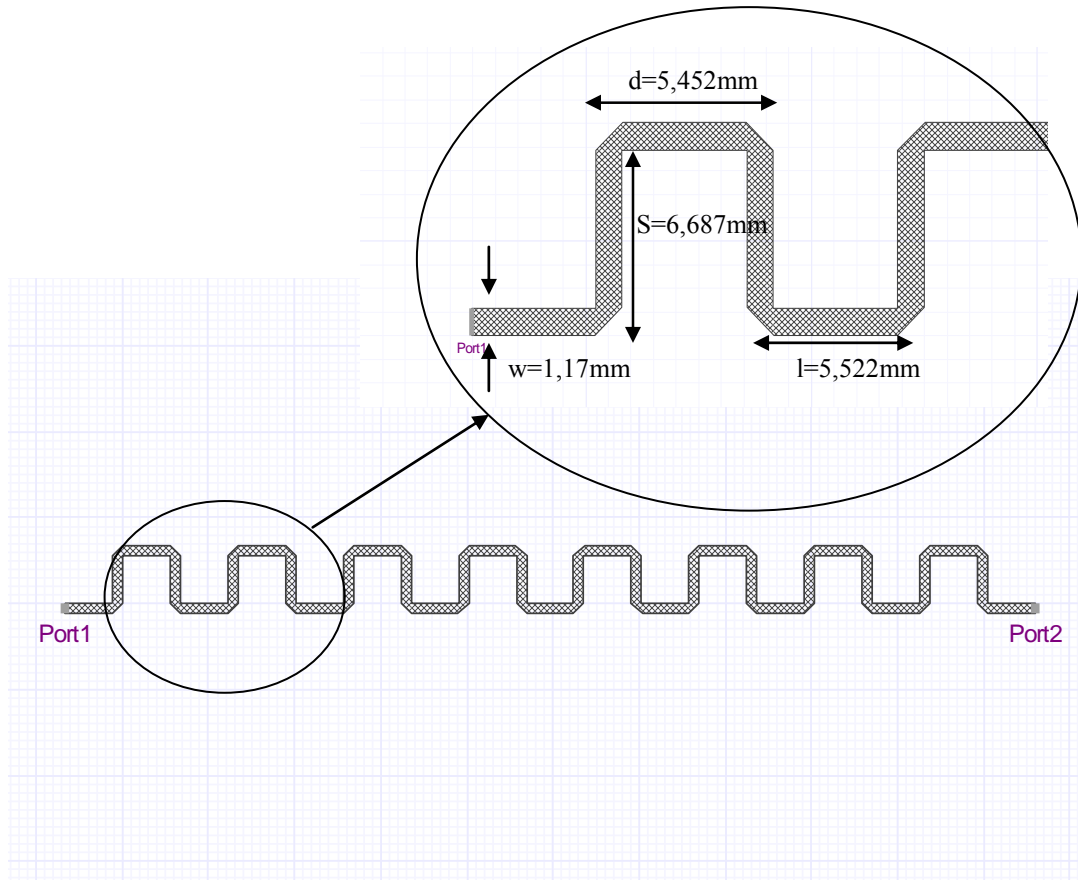


Figure 4.1 Ansoft Designer Schematic Model of Linearly Polarized 8 Element Meanderline Array

As shown in Figure 4.1, meanderline array is represented with meshes on the surfaces and there are two ports. First port is the excitation port and the second port is termination port. Optimized dimensions of the meanderline array are given on the simulation schematic model.

S-parameters of the meanderline antenna have been simulated between 9-11 GHz. E-plane radiation pattern of the array has been simulated at 10 GHz. Ansoft Designer simulation results of the meanderline array is compared with measurement results and presented in Sections 4.5.1 and 4.5.2.

Ansoft Designer simulates 2.5-D structures, i.e. it uses infinite substrate and ground plane. However, it is possible to analyze finite 3-D structures with HFSS. Therefore, meanderline array has been analyzed with Ansoft HFSS as well. The meanderline array is located in y-z plane in HFSS, S-parameters, E- and H-plane co- and cross-polarization patterns, three dimensional pattern and current distribution on the meanderline at 10 GHz have been investigated.

In addition, HFSS simulations have been compared with Ansoft Designer simulations. In Figure 4.2, S11 simulation of linearly polarized meanderline array is presented.

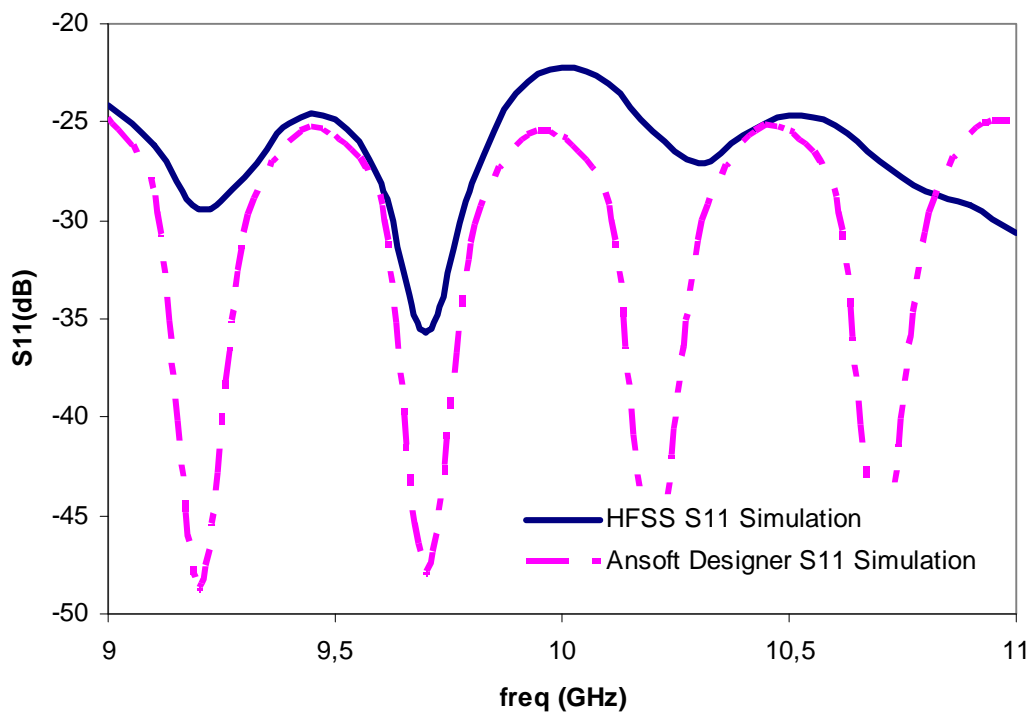


Figure 4.2 Ansoft Designer and HFSS S11 Simulations of Linearly Polarized Meanderline Array

As shown in Figure 4.3, E-plane pattern at Ansoft Designer and HFSS are similar, but there is a small shift at the maximum radiation direction. Maximum radiation direction is 32° at Ansoft HFSS and 30° at Ansoft Designer. Since HFSS defines finite dielectric in simulations, discrepancy between side lobe levels is expected.

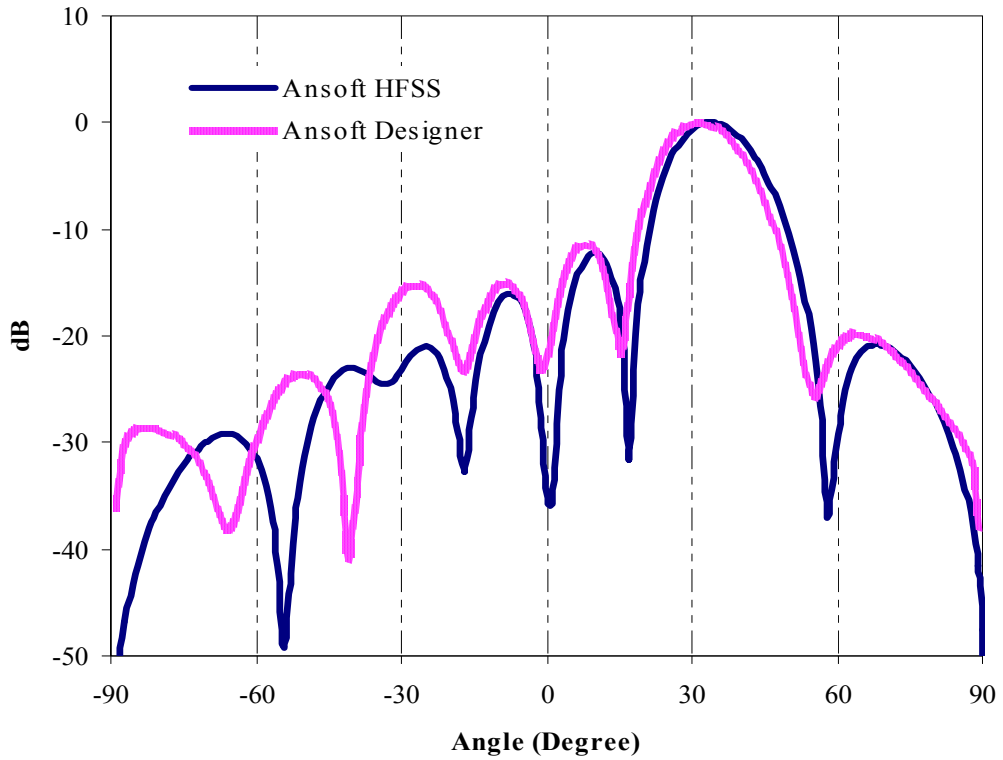


Figure 4.3 Ansoft Designer and HFSS E-plane Electric Field Pattern of Linearly Polarized Meanderline Array at 10 GHz

E-plane (X-Y) plane co- and cross-polarization patterns at 10 GHz are given in Figure 4.4. In simulations more than 20 dB cross-polarization level has been achieved at the maximum of the antenna main beam that satisfies the linearity requirement. Co-polarization of the antenna corresponds to z component of the E-field since the antenna is vertically polarized and cross-polarization of the antenna is y component of the electric field.

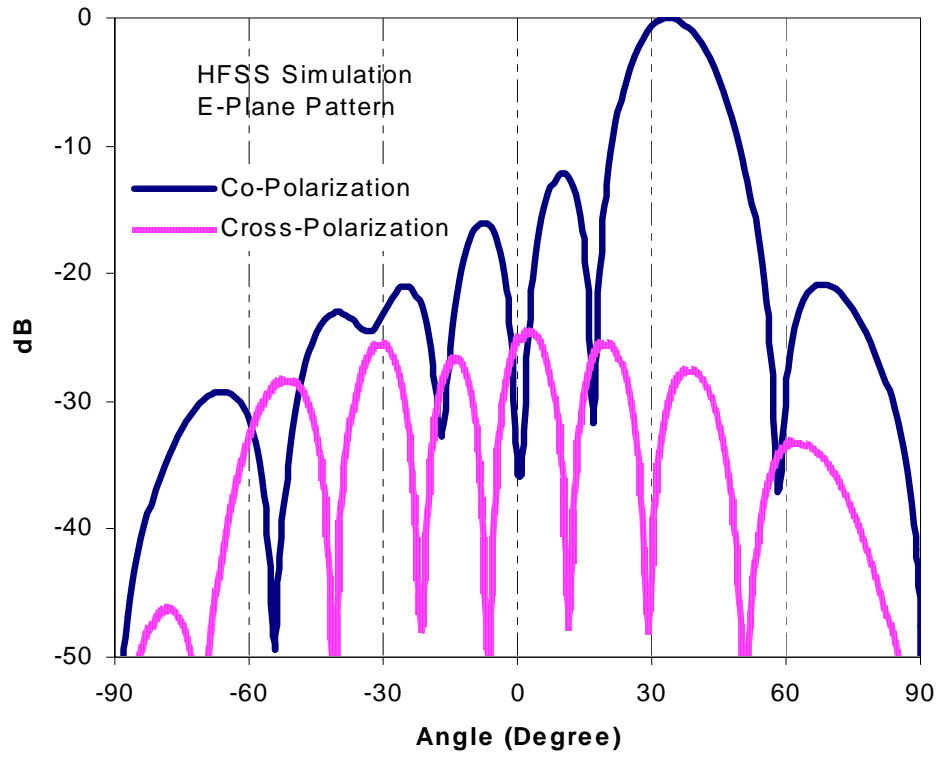


Figure 4.4 Co- and Cross-Polarization E-Plane Electric Field Patterns of Meanderline Array at 10 GHz

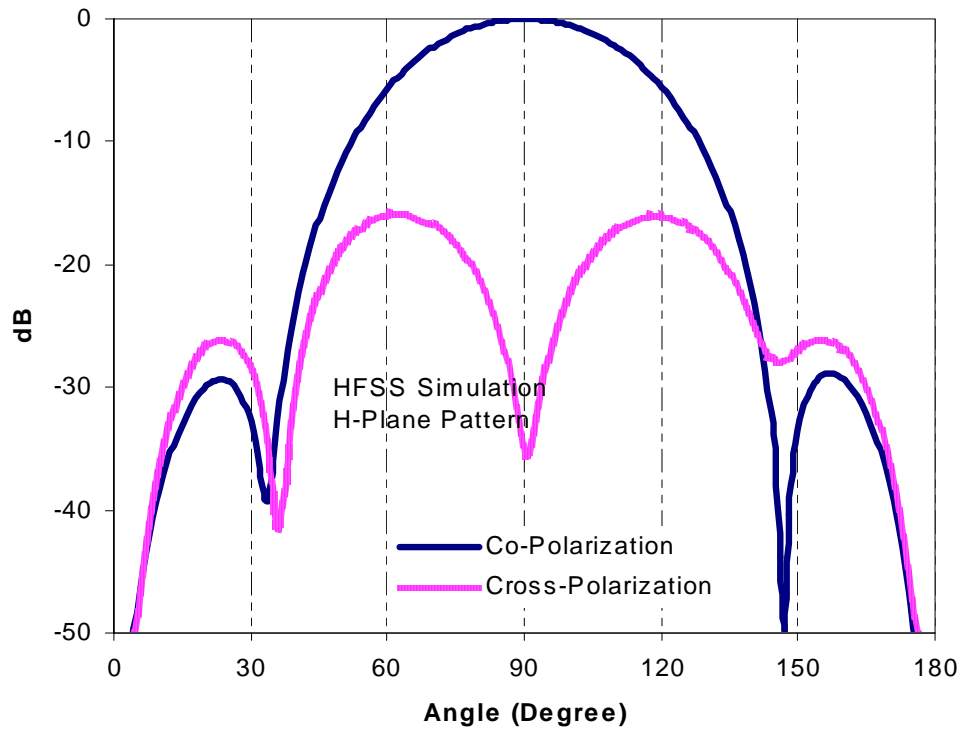


Figure 4.5 Co- and Cross-Polarization H-Plane Electric Field Patterns of Meanderline Array at 10 GHz

H-plane pattern of the meanderline array at 10 GHz is shown in Figure 4.5 and H-plane cut of the antenna corresponds to a cut for $\phi=32^\circ$ (maximum of radiation at E-plane cut). Co- and cross-polarizations of the meanderline array are as seen from Figure 4.5 and there is more than 20 dB difference between co- and cross-polarization levels of the antenna.

3-dimensional radiation pattern of the meanderline array is shown in Figure 4.6. Main beam is directed towards 32° and side lobes of the antenna are shown clearly.

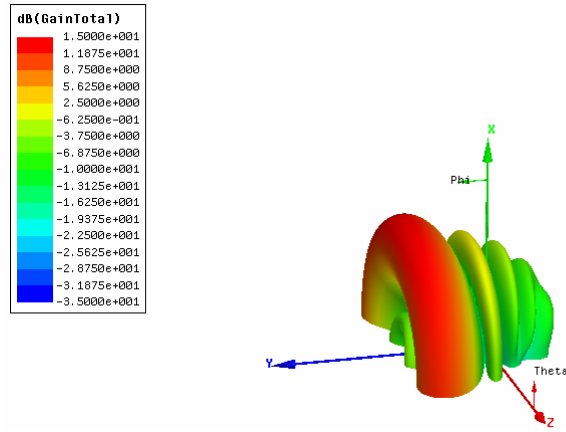


Figure 4.6 3-Dimensional Radiation Pattern of Meanderline Array

Surface current distribution of the meanderline array at 10 GHz and is presented as in Figure 4.7.

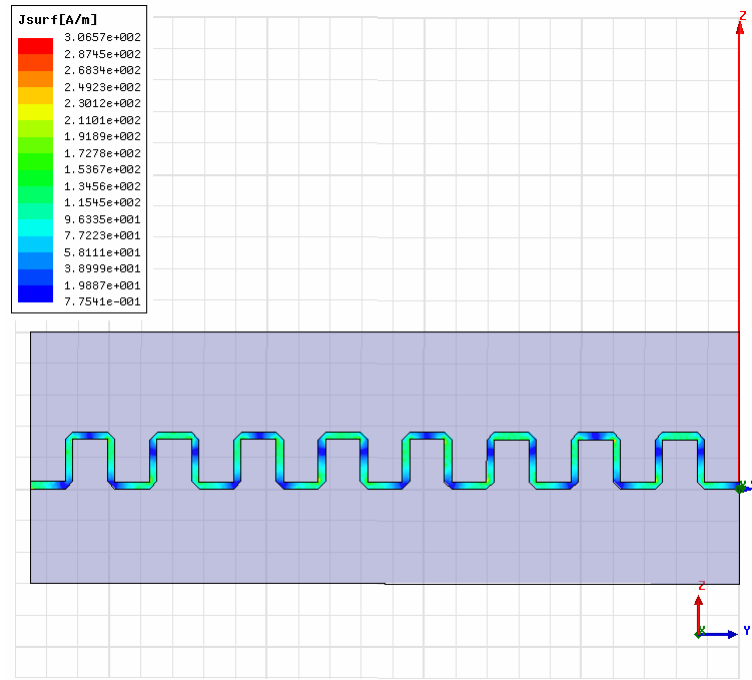


Figure 4.7 Surface Current Distribution of Meanderline Array

To sum up, linearly polarized meanderline array operating at 10 GHz has been investigated by using different simulation tools Ansoft Designer and Ansoft HFSS. Simulation results satisfy design criteria.

4.4 Fabrication of the Antenna

The designed linearly polarized meanderline array has been manufactured on 15 mil ROGERS 5880 Duroid with dielectric constant $\epsilon_r=2.2$. Fabrication of the antenna has been performed by a LPKF 200 Machine in ASELSAN facilities. Photograph of the fabricated antenna is shown in Figure 4.8. Tyco/AMP SMA connectors operating from DC-18 GHz have been used at the two ports of the array. The first connector is RF-input connector and 50 Ω load is connected to the second port as shown in Figure 4.8.

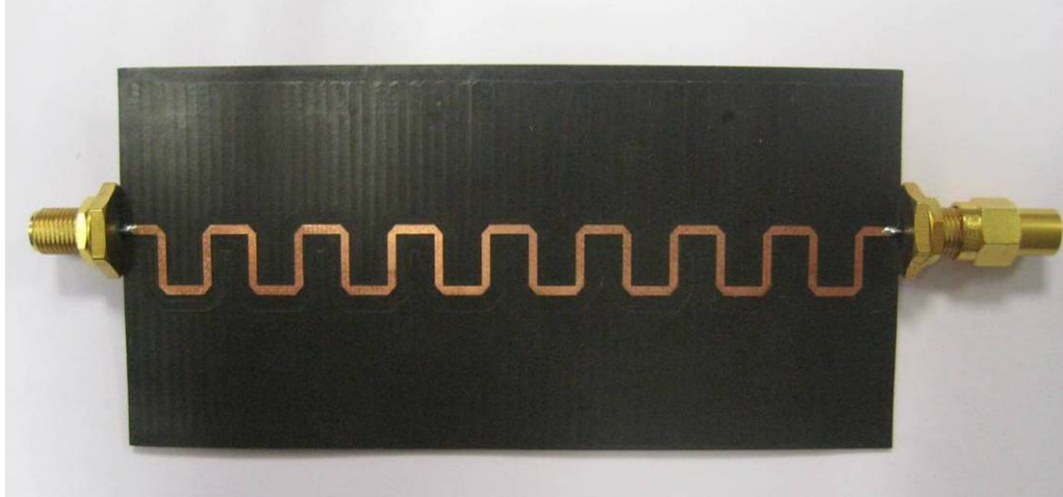


Figure 4.8 Prototype of Linearly Polarized Meanderline Array for X-band Applications

4.5 Measurements

S-parameters and radiation pattern of the meanderline array have been measured and compared with simulation results. Measurement set-ups and techniques are described briefly in the following sections. Measurement results are presented and compared with the simulation results.

4.5.1 S-Parameter Measurements of the Meander Line Array

The input return loss and S21 measurements of the meanderline array have been performed using Agilent E8364C PNA, 10 MHz to 50 GHz Vector Network Analyzer. Measurements have been carried out between 9-11 GHz. In order to measure S11 and S21 parameters of the antenna, network analyzer should be calibrated from the ports where the antenna will be connected. 3.5 mm Calibration Kit has been used for full two-port calibration. Before calibration, measurement frequency has been selected and IF bandwidth is set to 100 Hz and throughout the calibration open, short and load has been connected to each port of the network separately and lastly, two ports are connected with a through connection to complete

calibration.

After completion of calibration, S11 and S21 parameters of the antenna has been measured and compared to simulation results performed using Ansoft Designer.

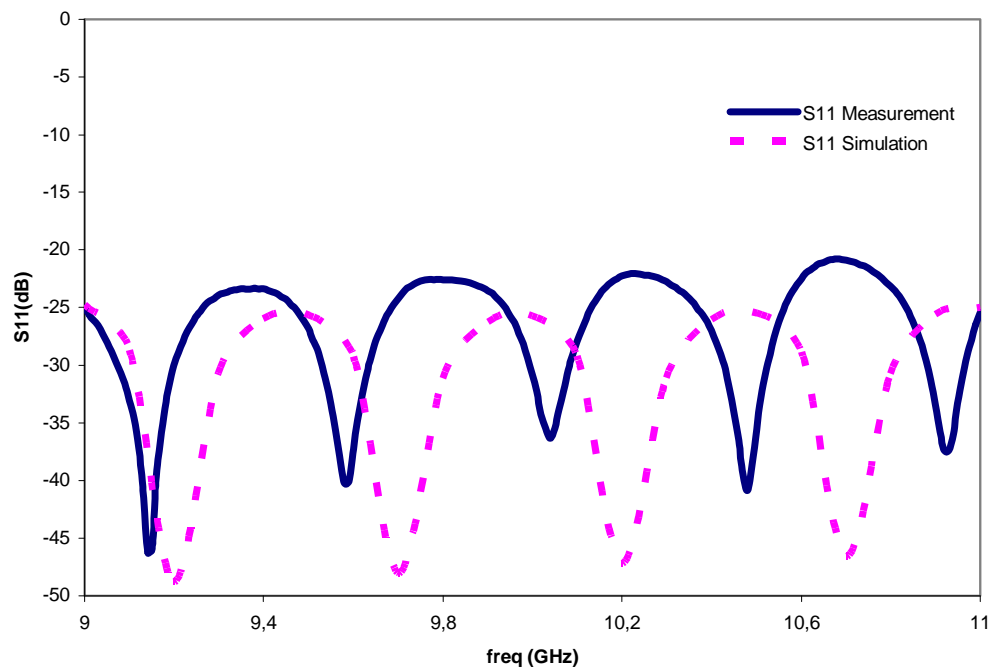


Figure 4.9 S11 (Return Loss) Measurement and Simulation Results of Linearly Polarized Meanderline Array

As shown in Figure 4.9, return loss is well below -20 dB in the band. In addition measurement and simulation results are similar except a slight shift in frequency.

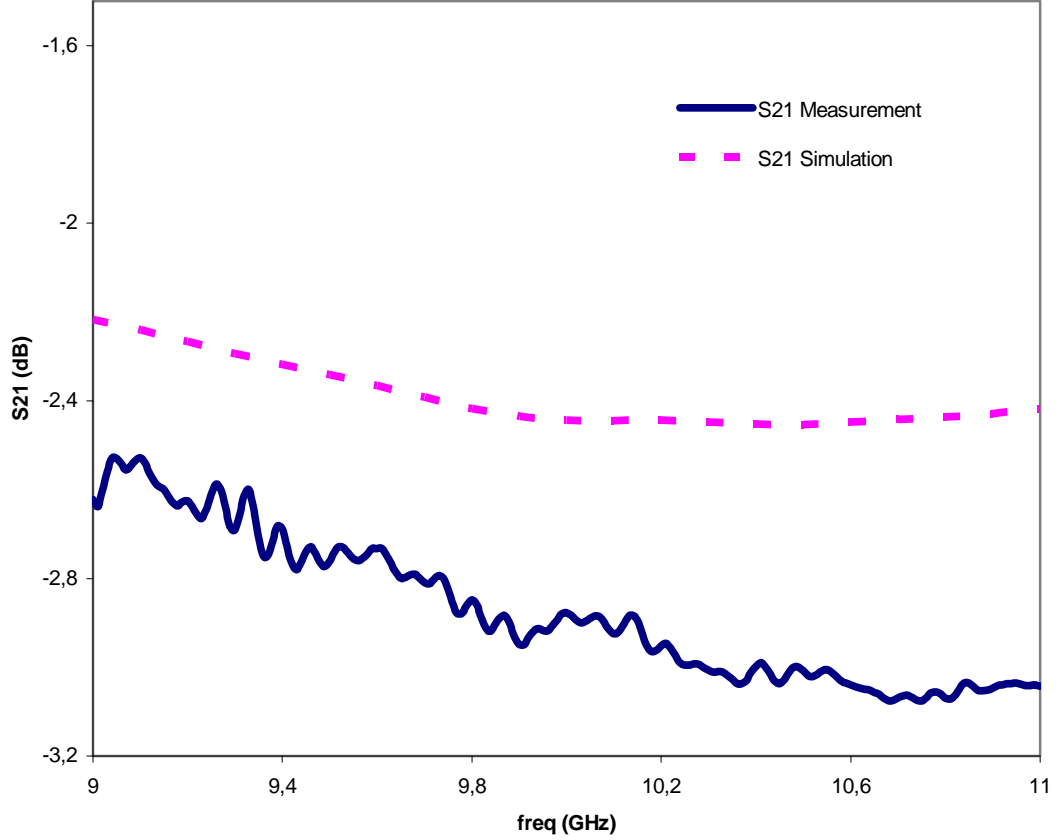


Figure 4.10 S21 Measurement and Simulation Results of Linearly Polarized Meanderline Array

In Figure 4.10, S21 measurements and Ansoft Designer simulations of meanderline array is shown. In Ansoft Designer simulations S21 is about 2.3 dB and in measurements it is approximately 2.6 dB; hence, there is a 0.3 dB difference between simulations and measurements. In fact, S21 of the meanderline array in simulations includes radiation losses and dielectric losses, on the other hand, connector losses and conductor losses have not been taken into account. Therefore, 0.3 dB difference in simulation and measurement is due to conductor and connector losses.

4.5.2 Radiation Pattern Measurements of the Meander Line Array

Radiation pattern of the array has been measured in tapered anechoic chamber at ASELSAN facilities. ASELSAN tapered anechoic chamber is described in Appendix C. Photograph of the meanderline array under test is shown in Figure 4.11.



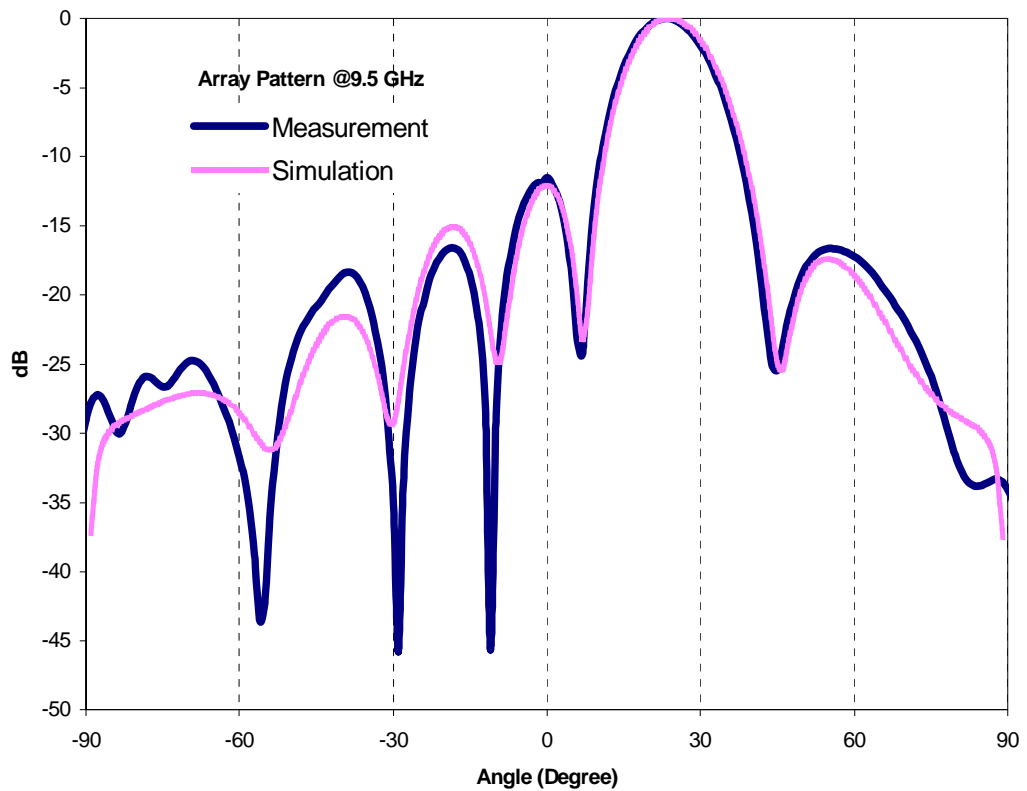
Figure 4.11 Linearly Polarized Meanderline Array under Test in Tapered Anechoic Chamber at ASELSAN Facilities

During measurements, meanderline array (AUT) is in receiver mode and the source antenna is transmitter mode. Source antenna is linearly polarized 2-18 GHz horn. So Co-polarized pattern of the meanderline array is measured when the source antenna is vertically placed in the test region and cross-polarized pattern of the meanderline array is measured by placing the feed antenna horizontally in the test region. Measurements have been performed at three frequencies; 9.5, 10 and 10.5 GHz.

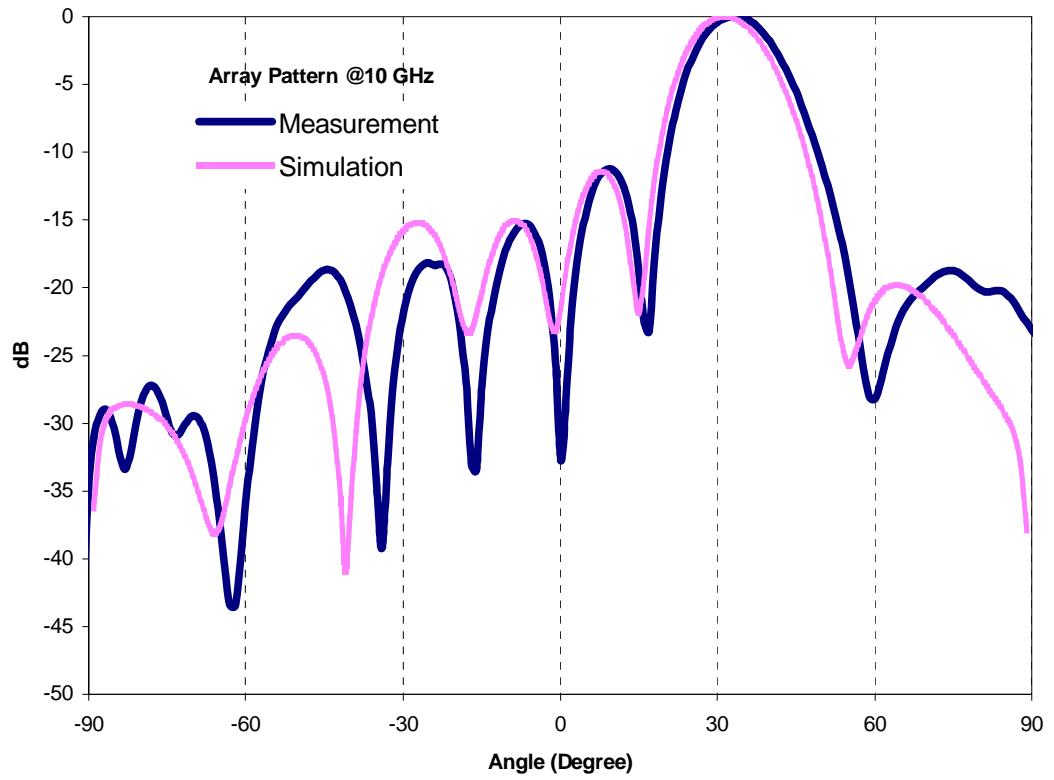
Comparison of E-Plane Pattern Measurements and Simulations

Measured E-plane pattern of the antenna is compared with the simulations and presented in Figure 4.12 (a), (b), and (c) for 9.5, 10 and 10.5 GHz.

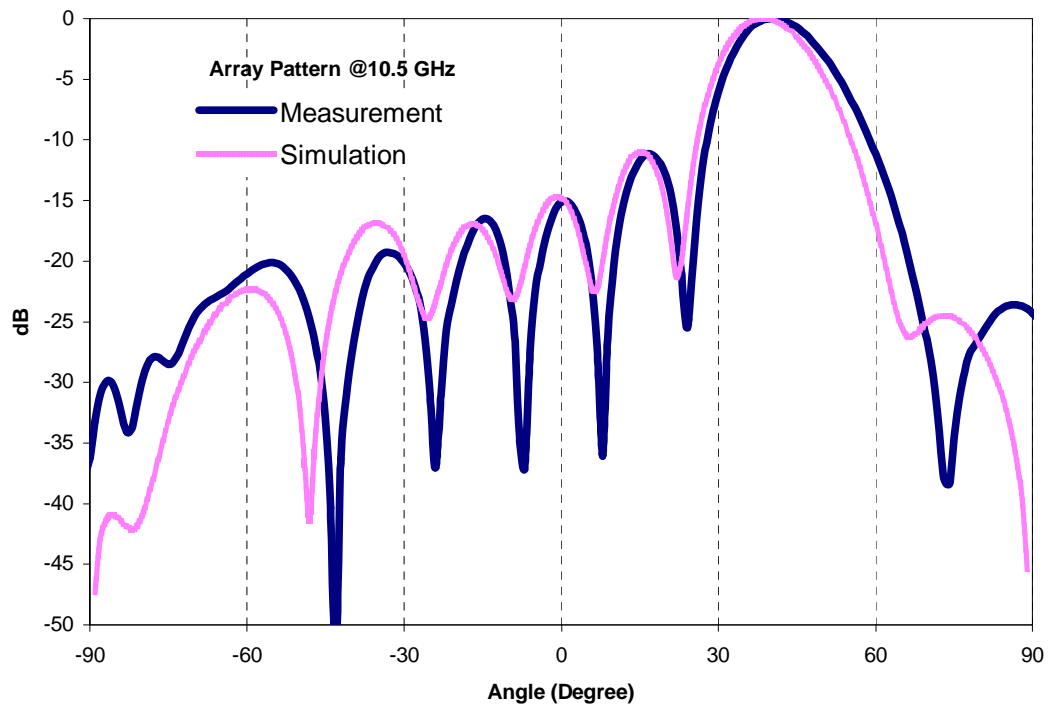
As shown from the Figure 4.12 (a), (b) and (c), measurements agree well with simulations. As the general characteristics of the meanderline array as frequency sweeps electrical length between elements varies so that main beam of the meanderline array sweeps. In Figure 4.12 (a) at 9.5 GHz beam direction is directed to 25° . At 10 GHz (Figure 4.12(a)) beam is directed to 32° and at 10.5 GHz (Figure 4.12(c)) beam is directed to 38° . Maximum side lobe levels at 9.5 GHz, 10 GHz and 10.5 GHz about 13 dB and satisfies design criteria.



(a) at 9.5 GHz



(b) at 10 GHz

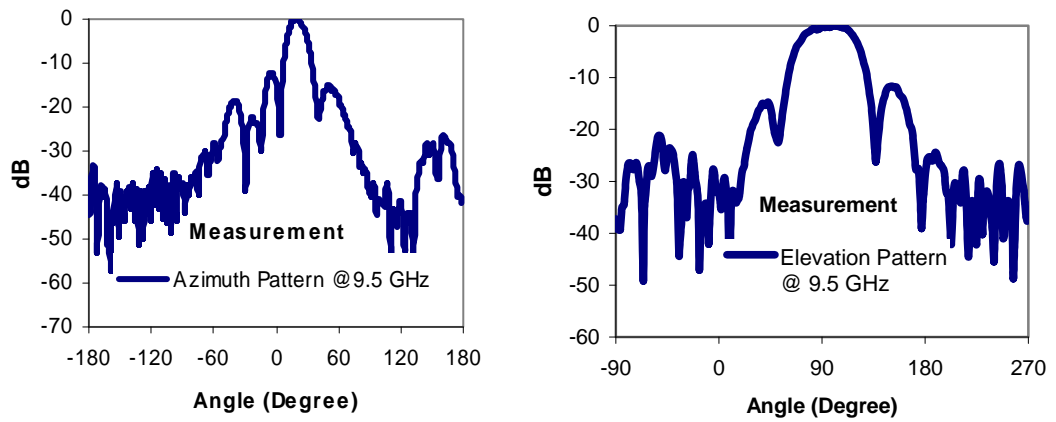


(c) at 10.5 GHz

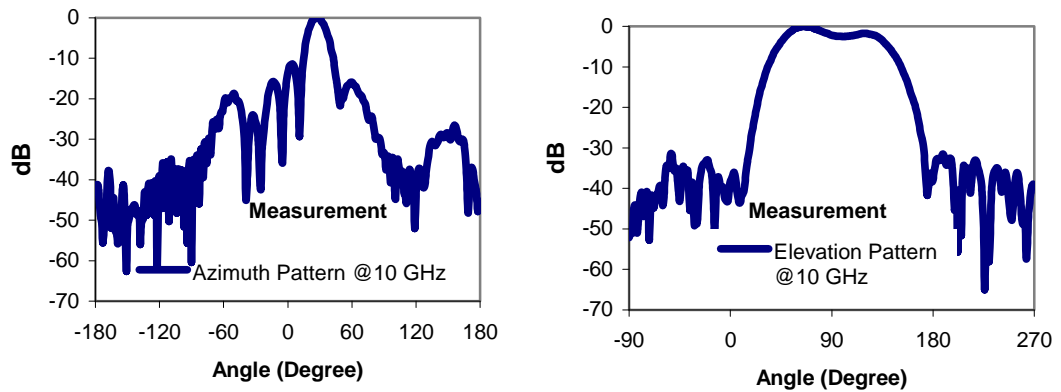
Figure 4.12 Meanderline Array E-plane Electric Field Pattern Co-Polarization Measurement and Simulation Results

E-Plane & H-Plane Pattern Measurements

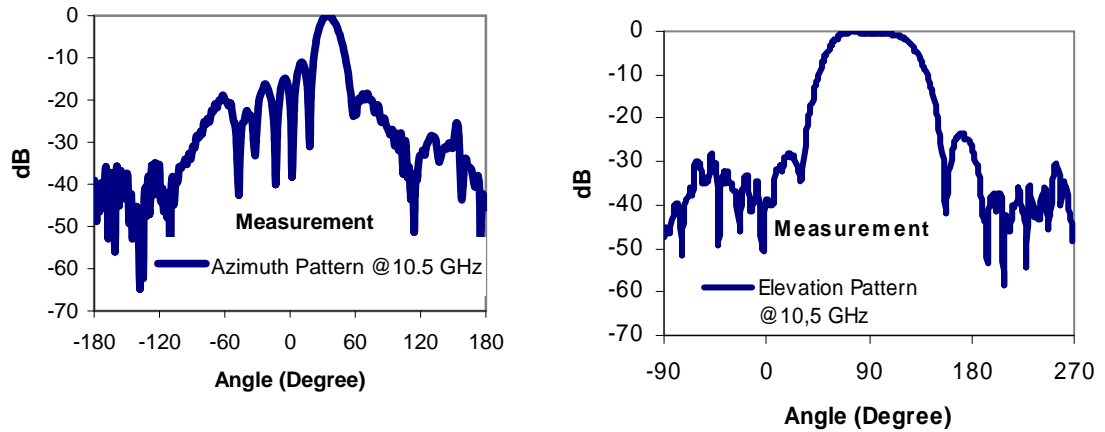
H-plane pattern of the meanderline array has been measured at three different frequencies. During H-plane measurement another rotator system has been used in order to measure the desired elevation cuts of the antenna. H-plane patterns as well as E-plane patterns are given in Figure 4.13 (a), (b) and (c). H-plane measurement results are similar to the H-plane patterns simulated in Ansoft HFSS



(a) at 9.5 GHz



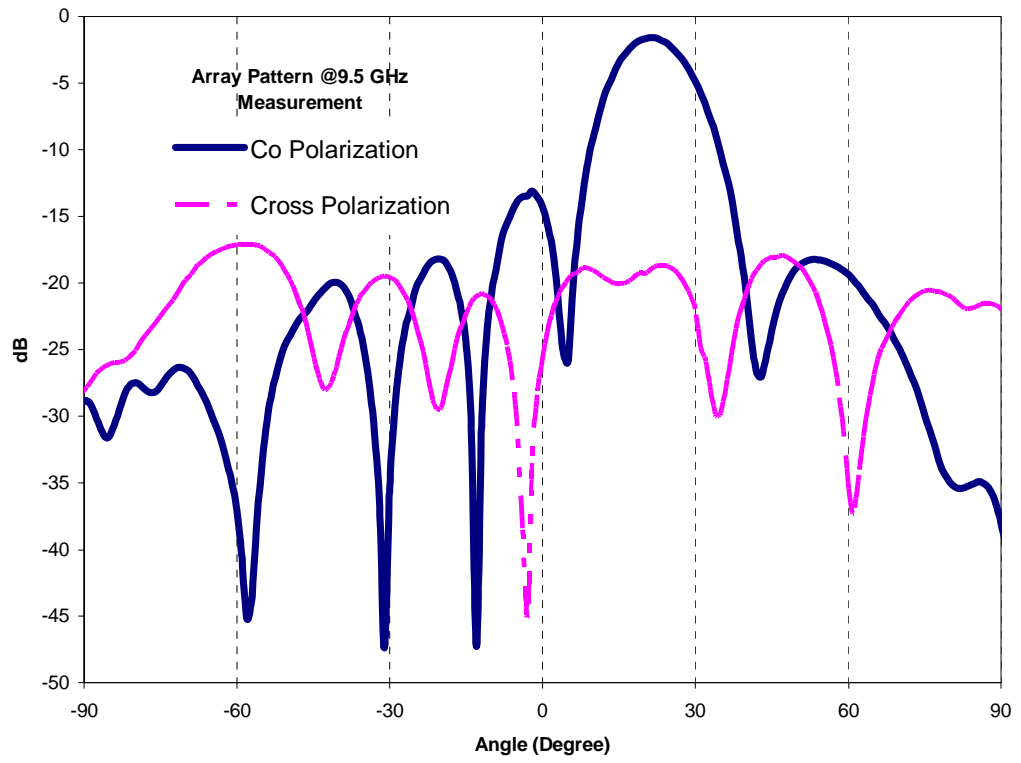
(b) at 10 GHz



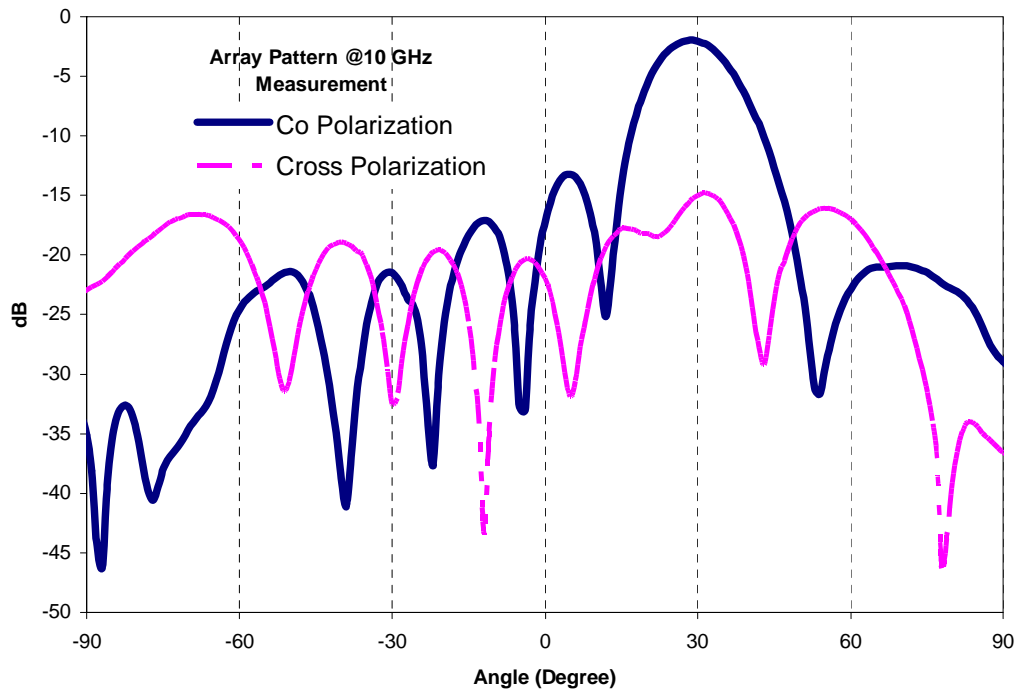
(c) at 10.5 GHz
Figure 4.13 Meanderline Array E-Plane and H-Plane Electric Field Pattern Measurement Results

Co- & Cross-Polarization Measurements

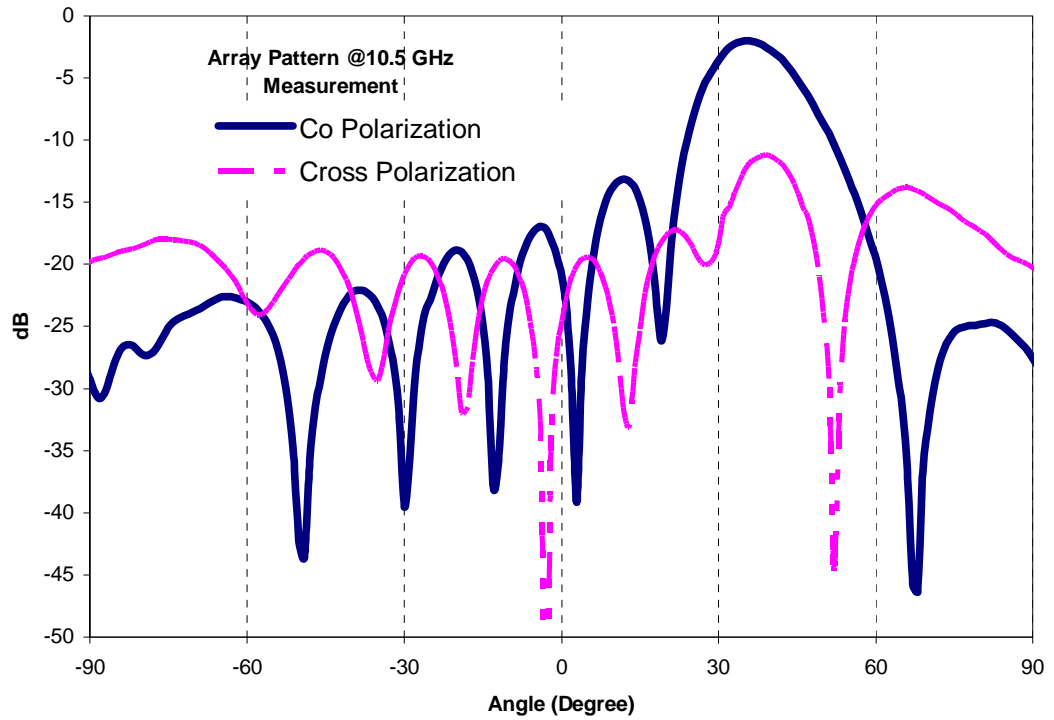
Measured cross polarized components of the patterns are given in Figure 4.14 in comparison with co-polarization patterns. There is more than 15 dB difference between co- and cross-polarization levels of the antenna, at 9.5 GHz and 10 GHz, whereas at 10.5 GHz difference between co- and cross-polarization levels decreases up to 10 dB. In other words, linear polarization of the meanderline array deteriorates while sweeping in frequency, because electrical length of the meanderline section varies and its inherent characteristic of traveling wave arrays.



(a) at 9.5 GHz



(b) at 10 GHz



(c) at 10.5 GHz

Figure 4.14 Meanderline Array E-Plane Co- and Cross-Polarization Electric Field Pattern Measurement Results

In this chapter linearly polarized meanderline array theoretical and practical design procedures have been explained in detail. Antenna structure has been analyzed by Ansoft Designer and HFSS. Obtained simulation results have been compared with measurements.

CHAPTER 5

DESIGN OF BEAM-STEERABLE TRAVELING WAVE MEANDERLINE ANTENNA

In this chapter, a beam-steerable traveling wave meander line antenna has been introduced for X-band radar applications. Beam steering capability of the meander line antenna has been achieved by loading the antenna by varactor diodes.

The beam-steerable meander line antenna is composed of eight meanderline sections and eight varactor diodes placed on top of the meanderline elements as shown in Figure 5.1. Varactor diodes are voltage-controllable devices and the capacitance of the diodes varies with the reverse-bias voltage. Loading the meanderline antenna elements with varactor diodes, impedance and the electrical length of the meanderline can be tuned. As a result, main beam of the meanderline array steers with the applied bias voltage. Figure 5.1 shows the schematic diagram of the beam-steerable meanderline array with varactor diodes and DC bias pad.

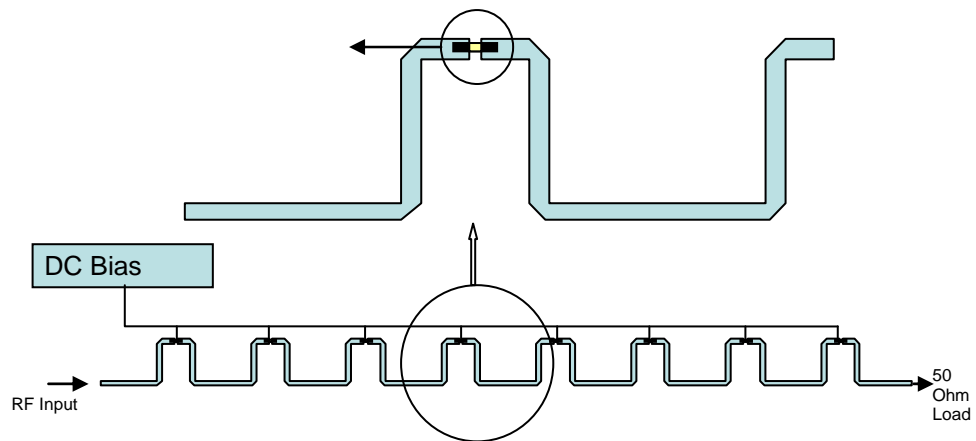


Figure 5.1 The Schematic View of Beam-Steerable Meanderline Antenna

Electrical properties of the beam-steerable meanderline array are similar to the properties of X-band linearly polarized meanderline array presented in Chapter 4. In the following sections, design aspects of beam steerable meanderline array and varactor diode phase shifting mechanism are given in detail. Afterwards, simulation results and measurements of the manufactured beam steerable array are presented.

5.2 Varactor Diode Phase Shifting Mechanism

Varactor diodes are voltage-controllable devices and are commonly used in electronic systems such as VCOs (Voltage Controlled Oscillators). By applying reverse-bias voltages, it is possible to obtain variable capacitance values. Besides, these features of varactor diodes are commonly used in phase shifting and capacitive loading mechanisms.

In this study, to rotate the beam of the meanderline antenna, meanderline is loaded with varactor diodes as shown in Figure 5.1.

Phase shift due to the varactor diodes directly depends on the capacitance variation controlled by the applied DC voltage. Many commercially available varactor diodes do not provide large capacitance variation, on the other hand; Microsemi MPV 2100 type varactors have very wide capacitance range under different bias voltages. Datasheet of Microsemi MPV 2100 varactor diode is given in Appendix C. Capacitance variation of varactor diodes with respect to different bias voltages given in datasheet is in Table 5.1.

Table 5.1 Microsemi MPV 2100 Type Capacitors Applied Voltage vs. Capacitance Values

Applied Voltage	Capacitance
0 V	2.7 pF
4 V	0.95 pF
20 V	0.3 pF

5.2.1 Characterization of Varactor Diode

In order to observe the phase shift provided by varactor diode, varactor diode on a microstrip line has been implemented on ROGERS 6010 Duroid with dielectric constant $\epsilon_r=10.2$ and dielectric loss tangent $\delta=0.0023$. Soldering pads of the varactor diode are placed on the back side; therefore silver epoxy has been used in order to mount the diode on the circuit board as shown in Figure 5.2.

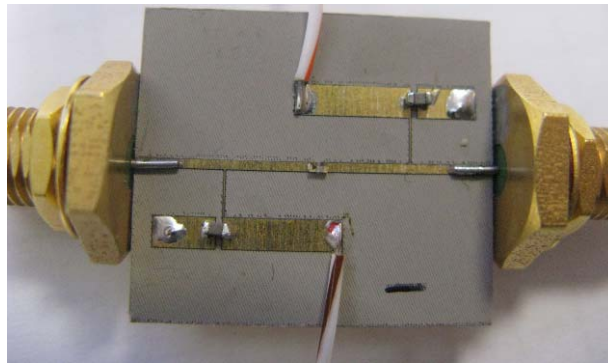


Figure 5.2 Bias Circuit of the Microsemi MPV2100 Varactor Diode Placed on the 50- Ω Microstrip Line

S-parameters of the varactor diode have been measured at 10 GHz using two-port network analyzer and given in Figure 5.3. S11 value is below -10 dB for different values of bias voltage and S21 values is around 2.5 dB.

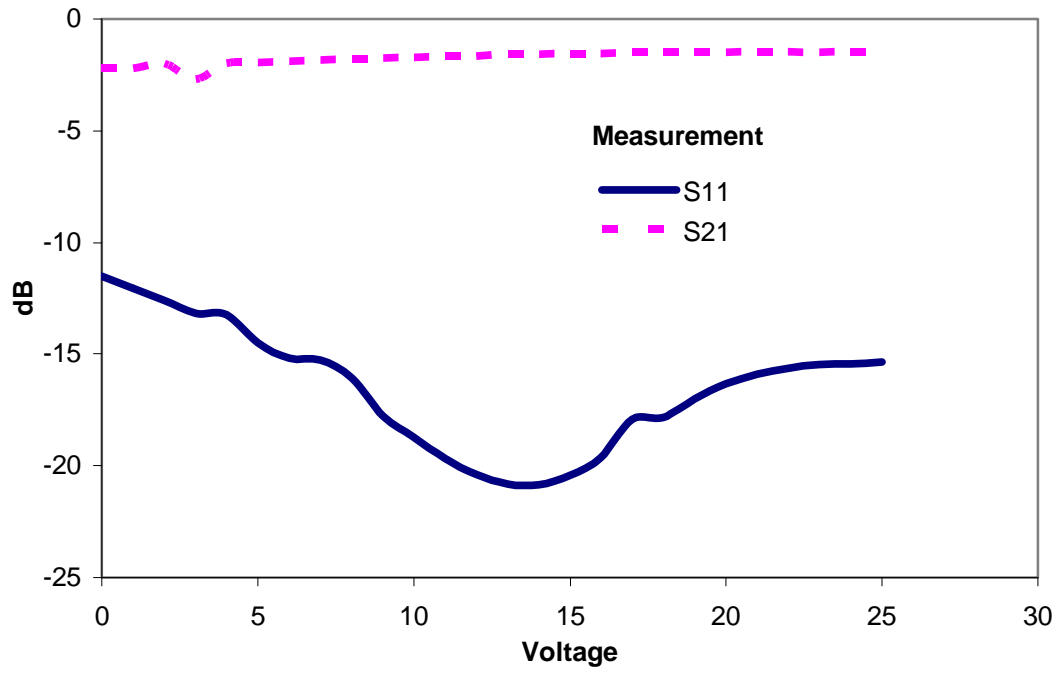


Figure 5.3 S-Parameter Measurement of Varactor Diode Bias Circuit

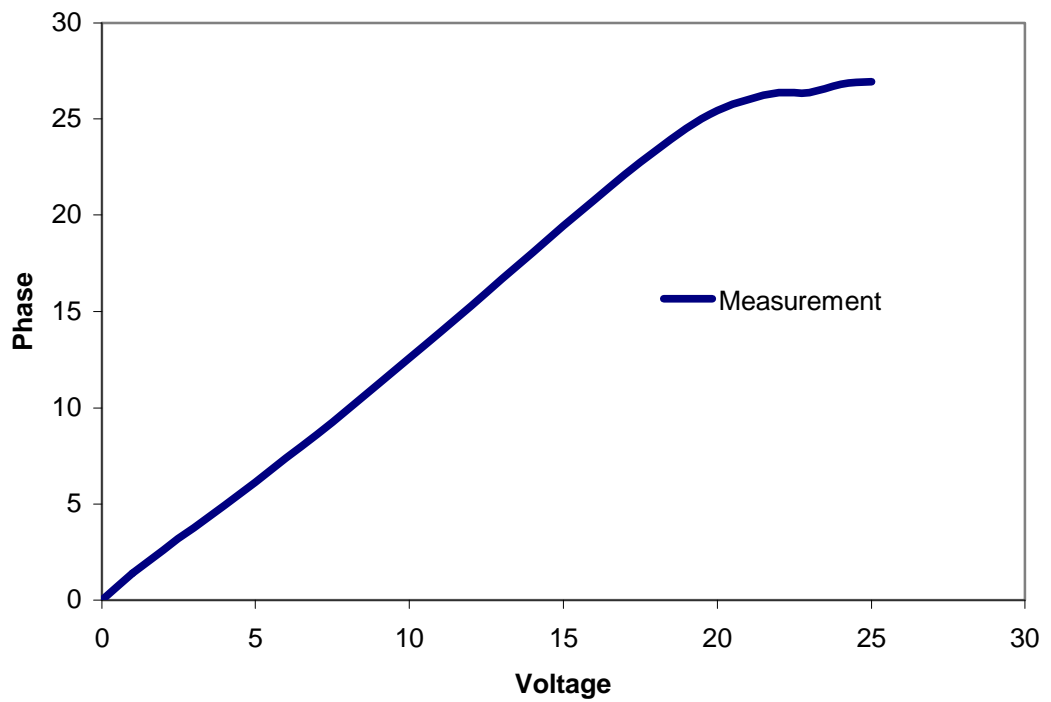


Figure 5.4 Measurement of Phase Variation with Respect to Different DC Bias Voltages

For different bias voltages, S21 phase values have been recorded and phase variation with respect to the bias voltage curve has been obtained and given in Figure 5.4. It is noticed that in measurements, more than 25° phase shift has been achieved. In addition, phase variation with respect to the bias voltage shows the linear change and this linear variation is an advantage during the design of beam-steerable meanderline array configuration since for constant increments of bias voltages, the direction of beam will sweep linearly.

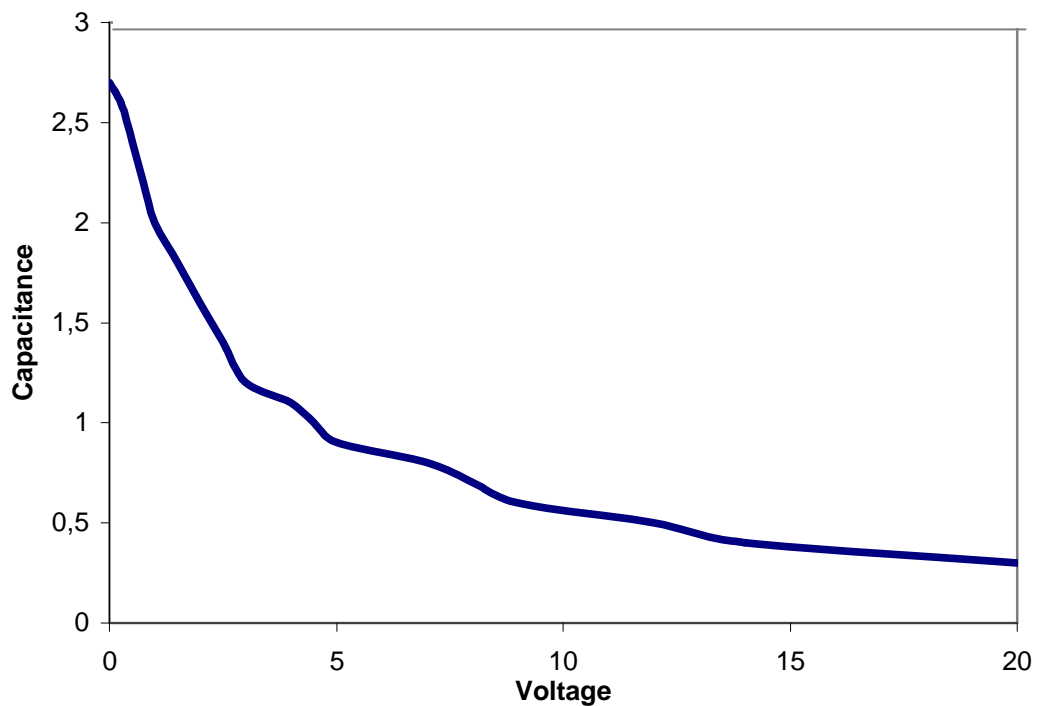


Figure 5.5 Relation between Applied Bias Voltage and Varactor Diode Capacitance

Furthermore, voltage versus capacitance curve of the varactor diode has been obtained in order to use during the design and measurement processes of beam-steerable meanderline array, as shown in Figure 5.5. It is observed that capacitance exhibits exponential variation with respect to the voltage as predicted from previous simulations and measurements.

5.3 Theoretical Investigations of Beam-Steerable Traveling Wave Antenna

Electrical parameters of the beam-steerable meanderline array are similar to those of linearly polarized meanderline array analyzed in Chapter 4. Therefore, theoretical analysis for polarization and direction of the radiation were not considered in this chapter. On the other hand, the design specifications of the beam-steerable meanderline array states that more than 10° beam variation is desired by applying corresponding phase shifts to the meanderline sections.

It is possible to analyze the beam variation of meanderline array by using array theory. Radiation direction of meanderline array can be found from

$$\psi = k_0(d + L)\cos\theta - (2s + d + L)\beta = 2n\pi \quad (5.1)$$

where $n=0,1,2,\dots$ and $\theta=90^\circ$ corresponds to broadside of the antenna array.

In Section 5.2, it is shown that 25° phase shift can be achieved using varactor diodes. Therefore, total beam steering for 25° phase shift has been calculated theoretically for given s , d and l parameters ($s=5.452$ mm, $l=6.687$ mm and $d=5.522$ mm). While calculating the radiation direction, width of the microstrip elements should be considered as well; because given s , l and d values are the edge dimensions of the meanderline array. In order to obtain corner-to-corner dimensions, width of the microstrip line should be incorporated in formulation as shown in Equation 5.2 so results will be more accurate.

Case 1: Phase= 0°

$$\psi = (d + L + 2w)\cos\theta - (2s + d + L + 2w)\beta = 2n\pi \quad (5.2)$$

After calculations, direction of radiation is found as $\theta=62^\circ$. It corresponds to 28° from broadside. Hence, the result is consistent with design specifications.

Case 2: Phase=25°

As shown in Equation 5.3, varactor diodes' phase shift should be added to the second part of the equation.

$$\psi = \frac{2\pi}{30}(d + L + 2w)\cos\theta - \{(2s + d + L + 2w)\beta + \text{phase}\} = 2n\pi \quad (5.3)$$

After calculations, direction of radiation is found as $\theta=72.2^\circ$, it corresponds to 17.8° from broadside.

Theoretical analysis shows that it is possible to steer the beam 10° towards broadside by applying 25° phase shift using varactor diodes.

In the next section, theoretical investigations are verified with full wave EM simulations.

5.4 EM Simulation Results

Simulations of the beam-steerable meanderline array have been performed using two electromagnetic softwares; Ansoft Designer and Ansoft HFSS.

In Ansoft Designer, S-parameters of N-port devices obtained from linear simulations can be inserted in electromagnetic simulations. Therefore, during the simulations of beam-steerable meanderline array, instead of varactor diodes, S-parameters of different capacitance values are inserted into 2-port boxes and these boxes are connected to meanderline sections as shown in Figure 5.6.

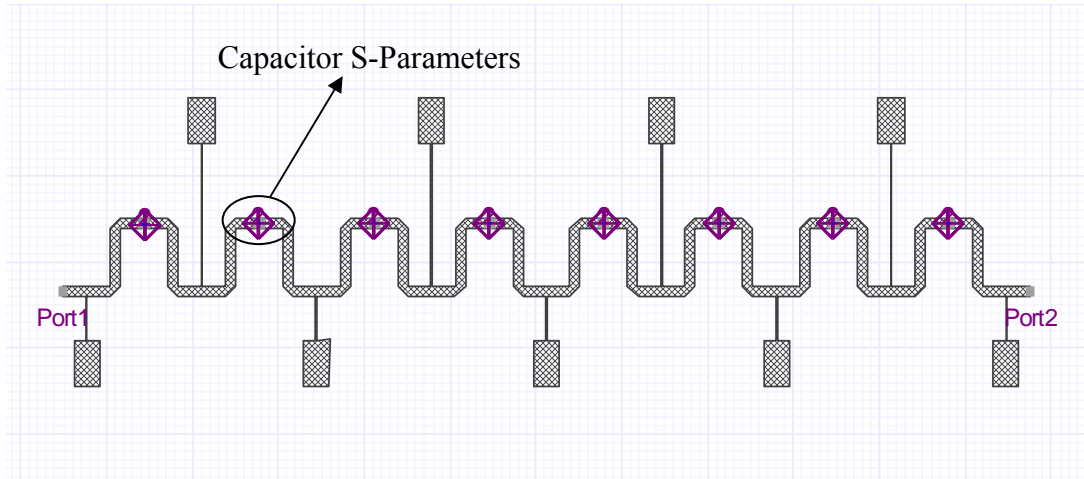


Figure 5.6 Ansoft Designer Model of the Beam Steerable Rampart Antenna with Varactor Diodes and Bias Lines

Dimensions of the beam-steerable meanderline array are similar to those of linearly polarized meanderline array mentioned in Chapter 4. In addition, varactor diodes' DC bias lines are reconfigured according to the geometrical structure of meanderline array. The unit element of meanderline array is illustrated in Figure 5.7 with dimensions $s=6.687$ mm, $l=5.452$ mm, $d=5.522$ mm, $l_1=16.35$ mm, $l_2=5.45$ mm, $l_3=5.45$ mm and $l_4=5.45$ mm.

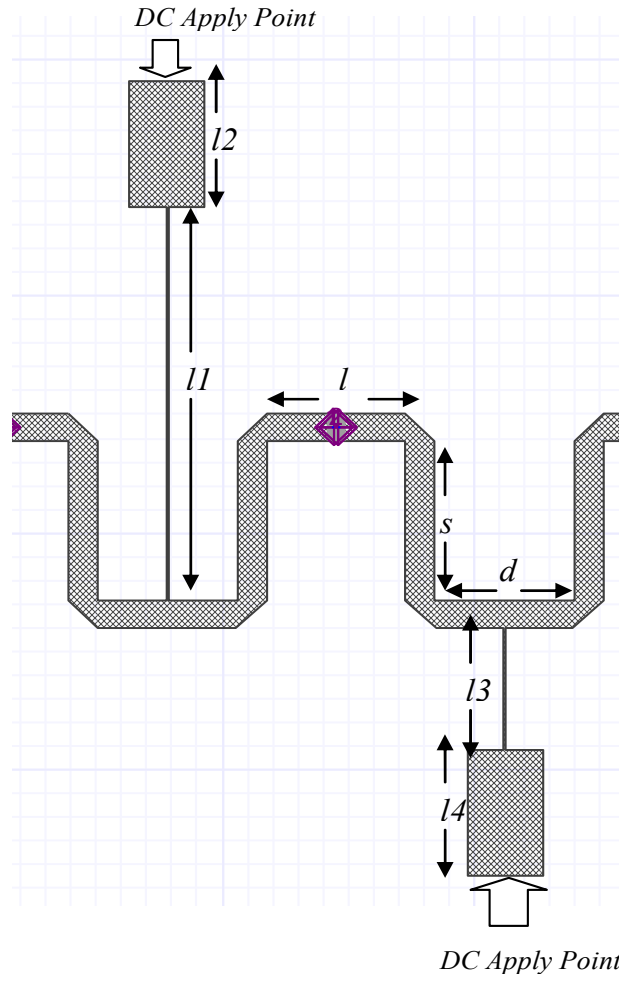


Figure 5.7 Unit Element of Beam-Steerable Meanderline Array

S-parameters obtained by Ansoft Designer is shown in Figure 5.8. As observed from the plots, for different values of varactor capacitance, return loss of beam-steerable array changes due to the impedance variation of the varactor diode. However, at 10 GHz, S11 value is well below -10 dB. Similarly, in Figure 5.9, S21 values for different capacitance values have been given and at 10 GHz, S21 value is about -3 dB.

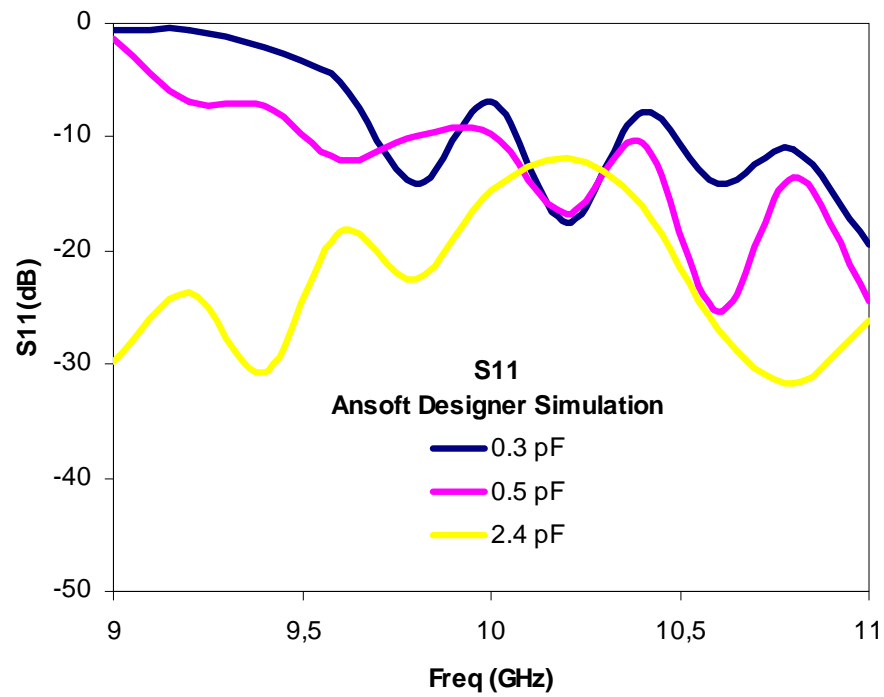


Figure 5.8 S11 Simulation of Beam-Steerable Meanderline Array for Various Capacitance Values

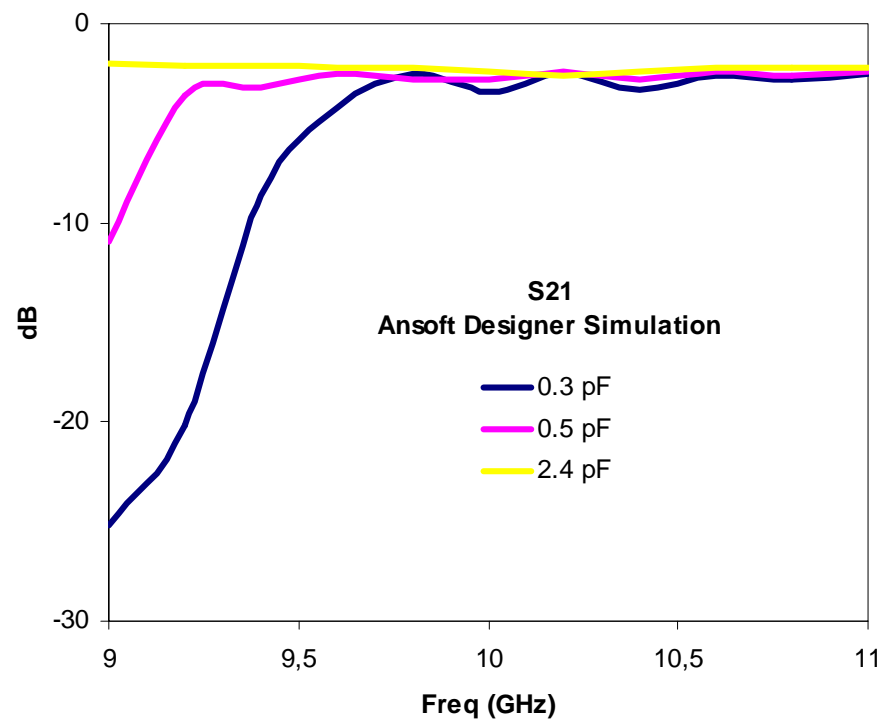


Figure 5.9 S21 Simulation of Beam-Steerable Meanderline Array for Various Capacitance Values

E-plane patterns for different values of varactor capacitances at 10 GHz is shown in Figure 5.10. The direction of the beam for 2.4-pF capacitance value is towards 30° and beam steers up to 19° for 0.3-pF capacitance value. Also, in Figure 5.11, beam variation with respect to varactor capacitance is presented. It could be derived from Figure 5.11 that beam steers more than 10° with corresponding varactor capacitance variation.

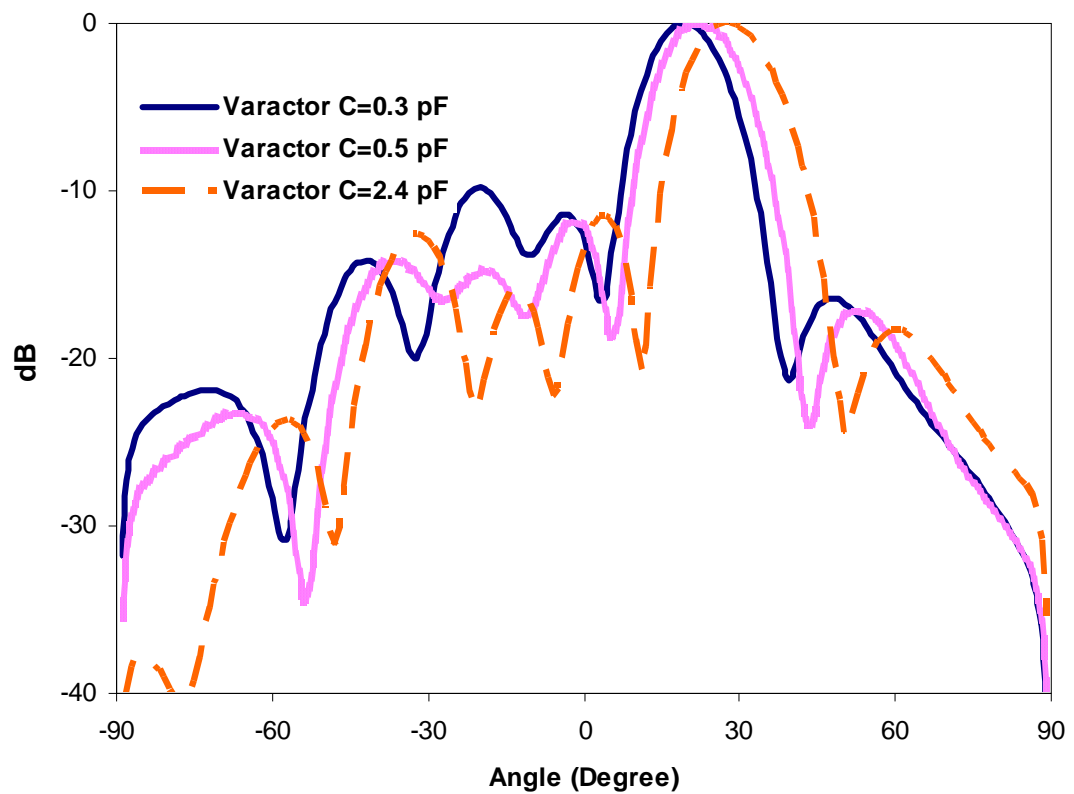


Figure 5.10 E-Plane Electric Field Pattern of Beam-Steerable Meanderline Array for Different Values of Varactor Capacitance (Ansoft Designer Simulation)

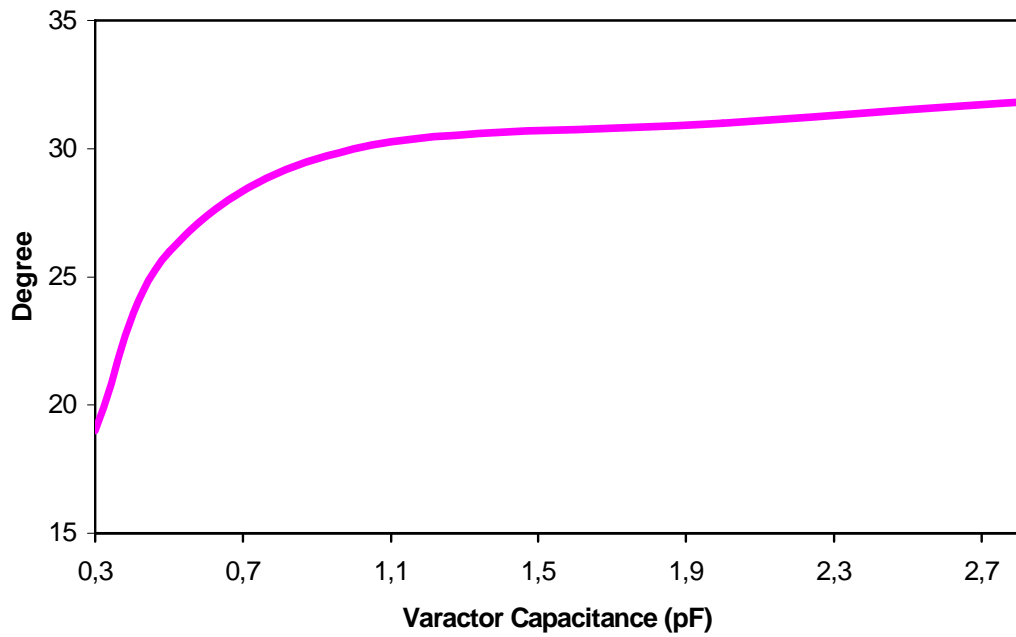


Figure 5.11 Beam Variation of Beam-Steerable Meanderline Array with respect to Varactor Capacitance Variation (Ansoft Designer Simulation)

E- and H-plane co- and cross-polarization patterns have been analyzed using Ansoft HFSS. Figure 5.12 shows E-plane co- and cross-polarization patterns of meanderline array. Since it is linearly polarized, there is more than 15 dB difference between co- and cross-polarizations' maximum values. H-plane radiation pattern of the meanderline array at 10 GHz has been illustrated in Figure 5.13. Difference between co- and cross-polarization levels is more than 15 dB which satisfies linearity requirements of beam-steerable meanderline array.

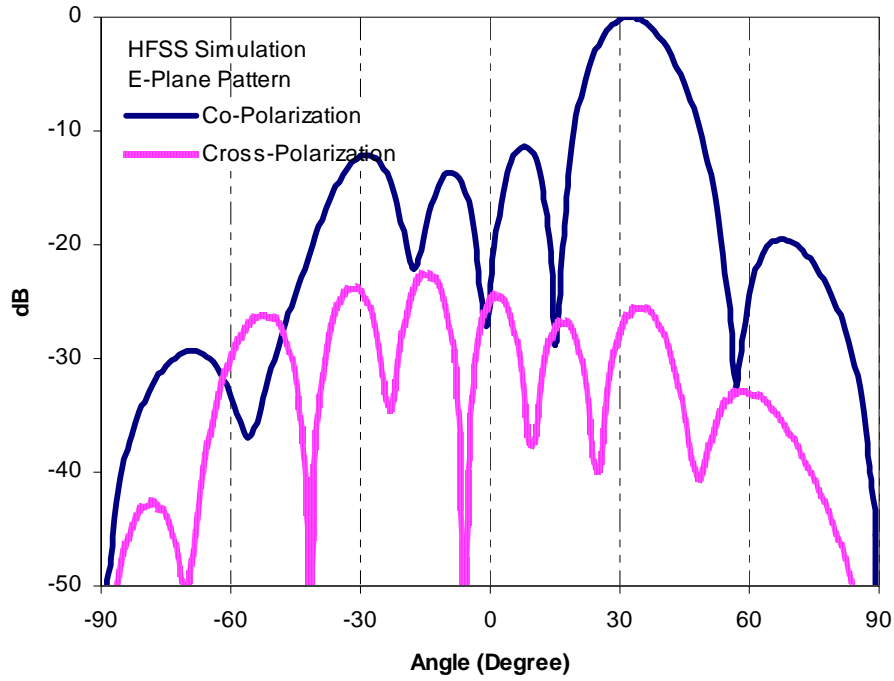


Figure 5.12 Co- and Cross-Polarization E-Plane Electric Field Patterns of Beam-Steerable Meanderline Array at 10 GHz

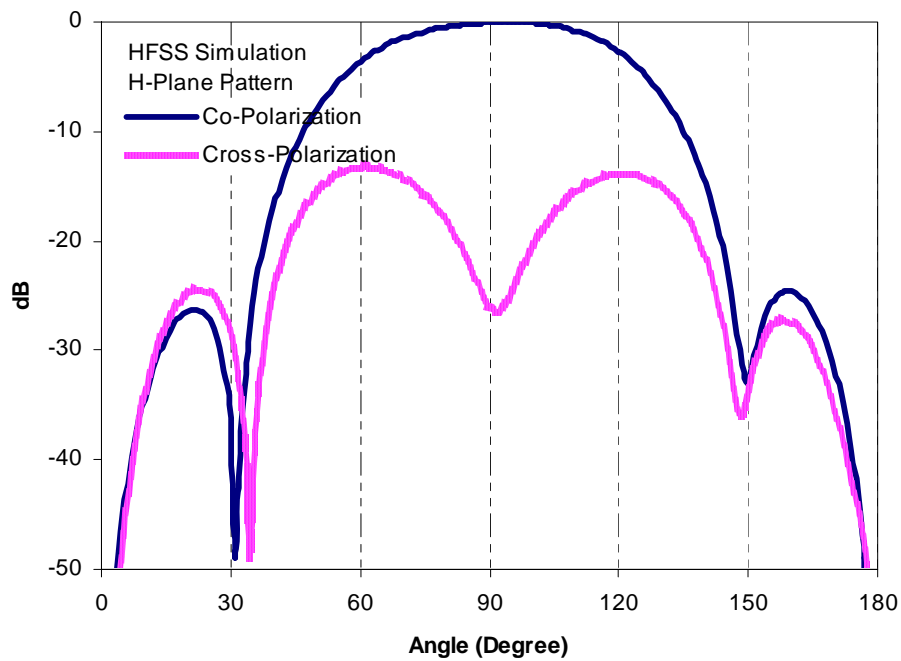


Figure 5.13 Co- and Cross-Polarization H-Plane Electric Field Patterns of Beam-Steerable Meanderline Array at 10 GHz

For different values of varactor capacitance, impedance of the varactor also changes; this affects the gain of the meanderline array. Ansoft Designer simulations show that the gain of the antenna decreases when the capacitance value of the varactor diode decreases.

Table 5.2 shows that for 2.4-pF varactor capacitance, gain of the meanderline array corresponds to 4.85 dB and it decreases down to 2.8 dB when the varactor capacitance equals 0.3 pF.

Table 5.2 Gain Variation of Meanderline Array for Different Values of Varactor Diodes Capacitance (Ansoft Designer Simulation)

Varactor Capacitance	Gain
0.3 pF	2.8 dB
0.5 pF	3.8 dB
2.4 pF	4.85 dB

To observe the effects of bias lines, surface current distribution obtained by HFSS is given in Figure 5.14 at 10 GHz. Current distribution demonstrates that no current flows on the bias paths, so meanderline array is not affected by varactor diodes' DC bias lines.

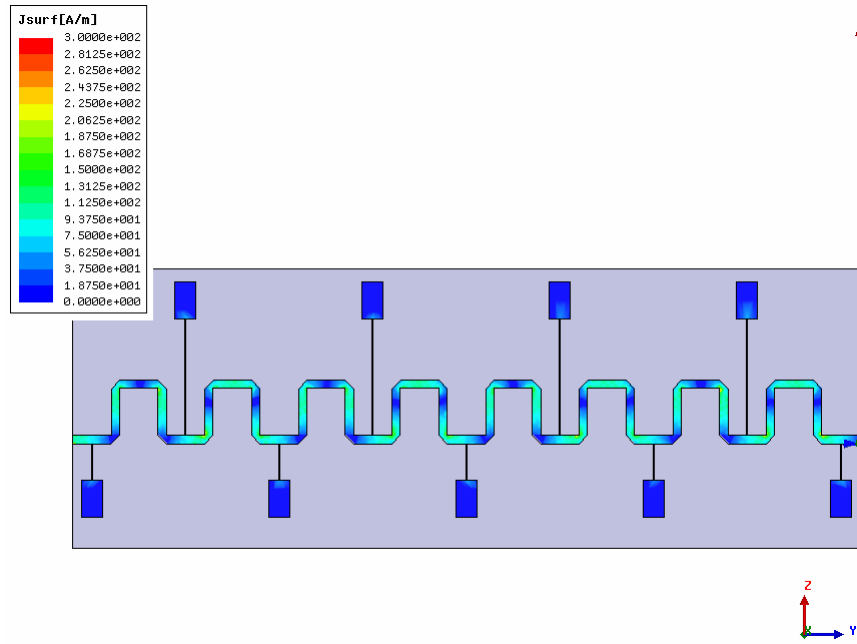


Figure 5.14 Surface Current Distribution of Meanderline Array

5.5 Production of Beam Steerable Antenna

Beam-steerable meanderline array has been manufactured on 15-mil thick ROGERS 5880 Duroid with dielectric constant $\epsilon_r=2.2$ as shown in Figure 5.15. Tyco/AMP SMA type connectors have been used at the input and termination ports. During radiation pattern measurements, second port is terminated with 50- Ω load.

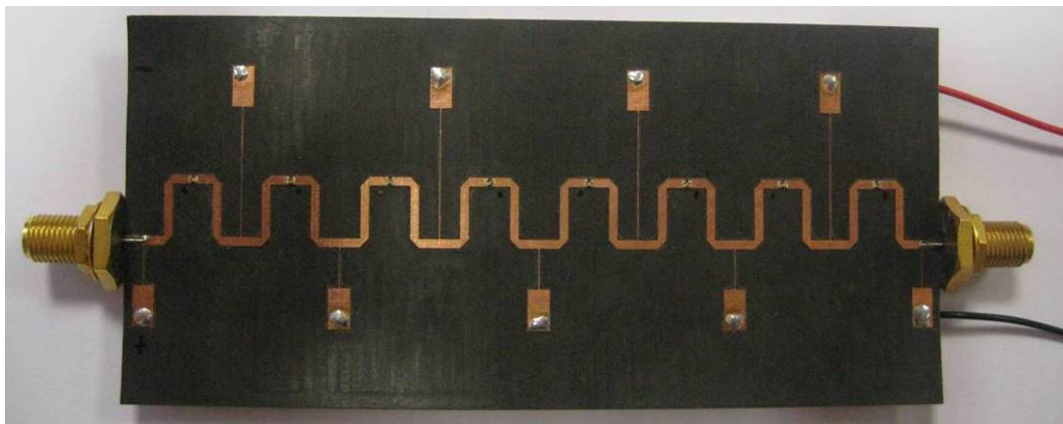


Figure 5.15 Prototype of Beam-Steerable Rampart Antenna with Varactor Diodes

In Figure 5.16, photograph of a unit cell of beam-steerable meanderline array with DC bias lines has been presented. Varactor diodes have been mounted on the meandering sections with silver epoxy cured at 150°C. Since ROGERS 5880 duroid is not suitable for plating, DC bias lines are connected to the DC pads placed on the ground plane by soldering.

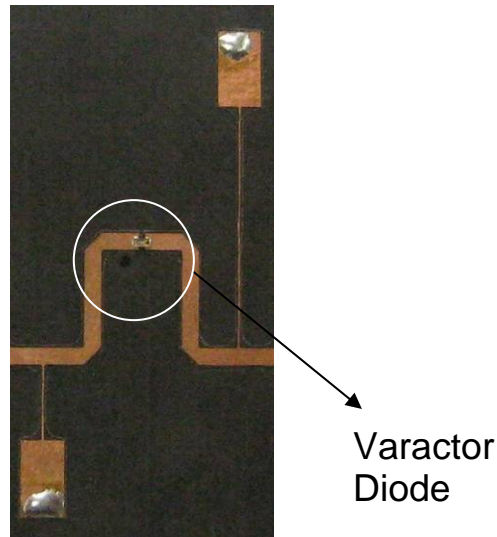


Figure 5.16 Unit Cell of the Beam Steering Rampart Antenna with DC Bias Pad

5.6 Measurements

In order to validate theoretical analysis and simulations performed in Ansoft Designer, S-parameters and radiation patterns of the meanderline array have been measured. In the following sections, measurement results will be presented.

5.6.1 S-parameter Measurements

S-parameter measurements of the beam-steerable meanderline array have been performed by using Agilent E8364C PNA, 10 MHz to 50 GHz Vector Network Analyzer. Two-port calibration has been carried out and antenna array has been measured between 9-11 GHz. Return loss of the beam-steerable meanderline array under different bias voltages has been measured to see the effect of capacitance variation to the S-parameters of the antenna. S11 measurements have been displayed in Figure 5.17. Return loss of the meanderline array is well below -10dB for different

values of bias voltages. Also, S21 parameter of the beam-steerable meanderline array has been measured and given in Figure 5.18. S21 parameter of the array is between -10 and -15 dB. Actually, S21 includes dielectric, copper, conductor, radiation losses and mainly varactor diodes' insertion losses. Furthermore, efficiency of the beam steerable meanderline array has been calculated at 10 GHz by using S-parameters.

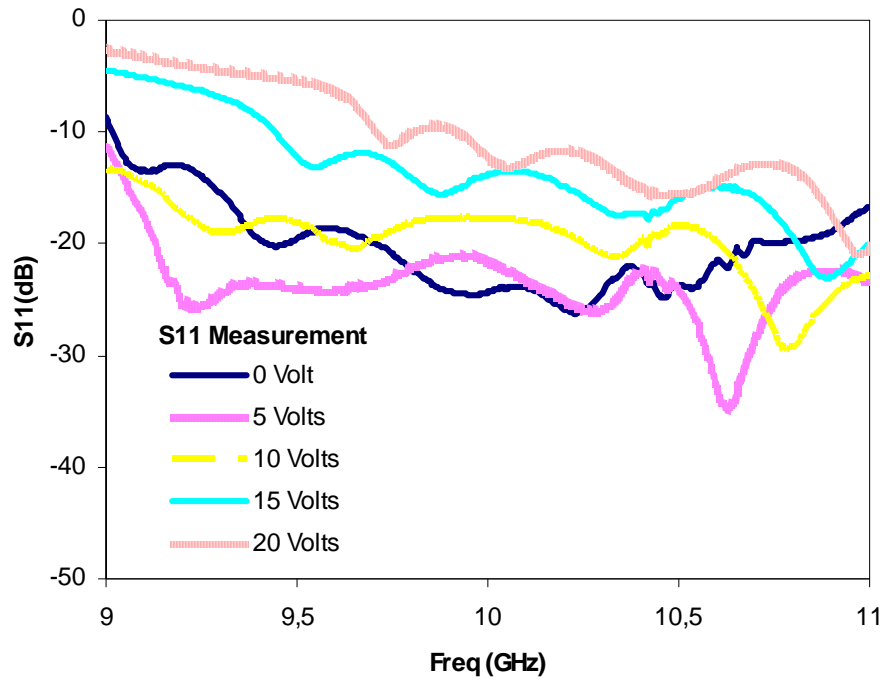


Figure 5.17 S11 Measurement of Beam-Steerable Meanderline Array Under Different Bias Voltages

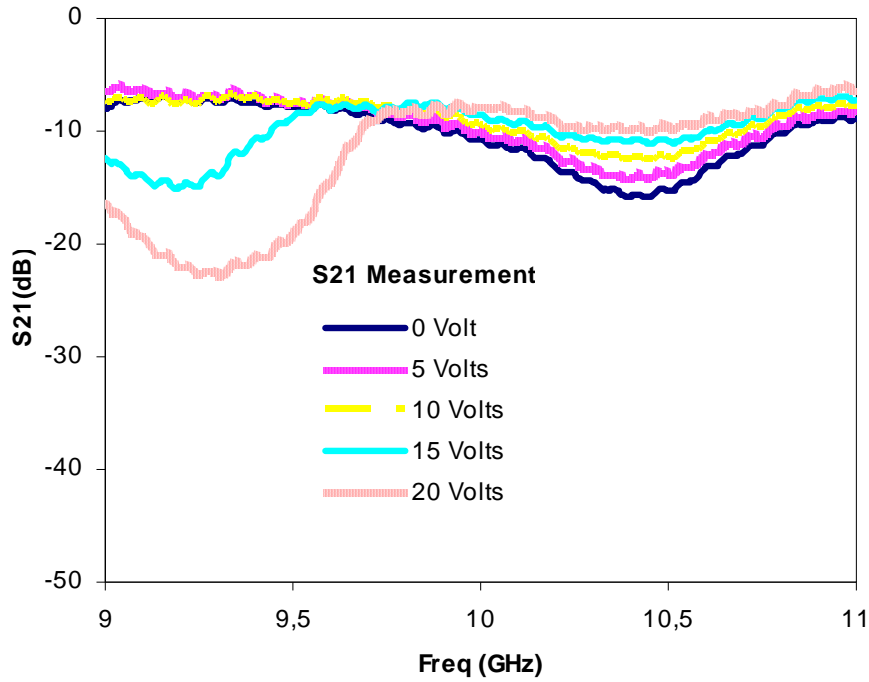


Figure 5.18 S21 Measurement of Beam-Steerable Meanderline Array under Different Bias Voltages

5.6.2 Radiation Pattern Measurements

Radiation patterns of beam-steerable meanderline array have been measured for different values of varactor diode bias voltage at 9.5, 10 and 10.5 GHz in tapered anechoic chamber at ASELSAN facilities

By using the relation between varactor capacitance vs. voltage derived in Section 5.2.2, simulations performed in Ansoft Designer are compared with measurements. Figure 5.5 indicates that 0-V bias voltage corresponds to 2.4-pF capacitance, therefore; in Figure 5.19, measured E-plane pattern under 0-V bias voltage is compared to the simulation with 2.4-pF capacitance case. It shows that simulations are consistent with measurements around the main beam. The difference at far side lobes is due to the effects of the platform on which the antenna is placed during measurement. In Figure 5.20 and Figure 5.21, simulations with different values of varactor capacitances are compared with measurements under 10-V and 20-V bias voltages. Reasonable agreement between simulations and measurements is observed.

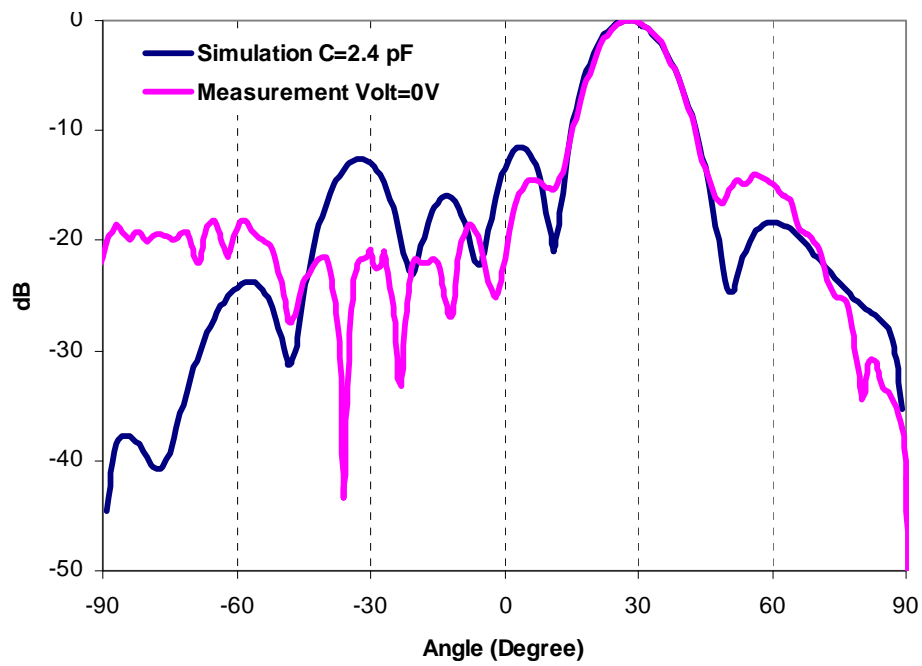


Figure 5.19 E-plane Electric Field Pattern Measurement under 0 Volt Bias Voltage and Ansoft Designer Simulation with 2.4 pF Varactor Capacitance

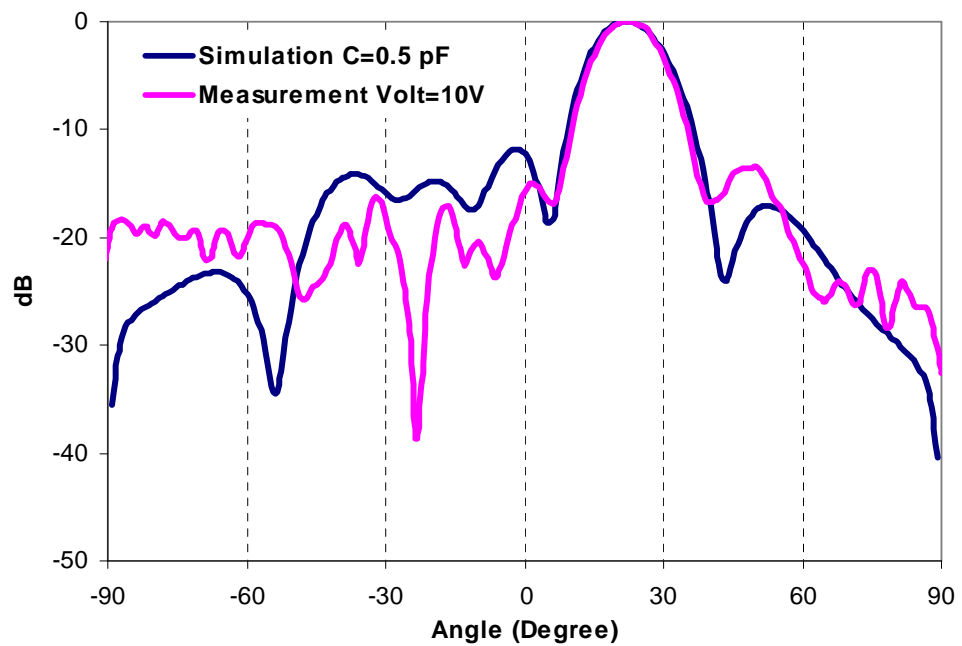


Figure 5.20 E-plane Electric Field Pattern Measurement under 10 Volt Bias Voltage and Ansoft Designer Simulation with 0.5 pF Varactor Capacitance

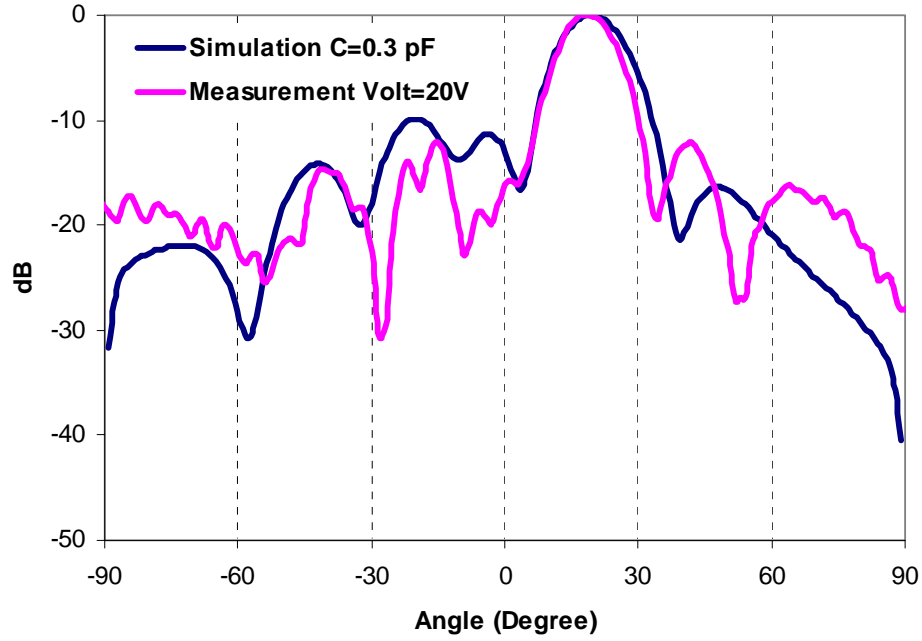


Figure 5.21 E-plane Electric Field Pattern Measurement under 20 Volt Bias Voltage and Ansoft Designer Simulation with 0.3 pF Varactor Capacitance

Furthermore, E- and H-plane measurements at 9.5, 10 and 10.5 GHz have been performed with different bias voltages. Results of E-plane measurements have been illustrated in Figure 5.22, Figure 5.23, and Figure 5.24. These figures show that the direction of the radiated beam steers linearly with respect to applied DC bias voltage. On the other hand, while the beam is steering, side lobes of the beam-steerable meanderline array also increase up to -10 dB. Also, as seen in Figure 5.22, Figure 5.23 and Figure 5.24, at different frequencies beam is steering at different angles. Electrical length between meanderline unit elements varies with frequency. Therefore, direction of radiation is steering with frequency as well.

H-plane measurements of beam-steerable meanderline array have been demonstrated in Figure 5.25, Figure 5.26, and Figure 5.27. H-plane pattern of the array does not change significantly with respect to the applied bias voltages. However, especially at 10.5 GHz, H-plane pattern is affected by the varactor diodes' bias lines.

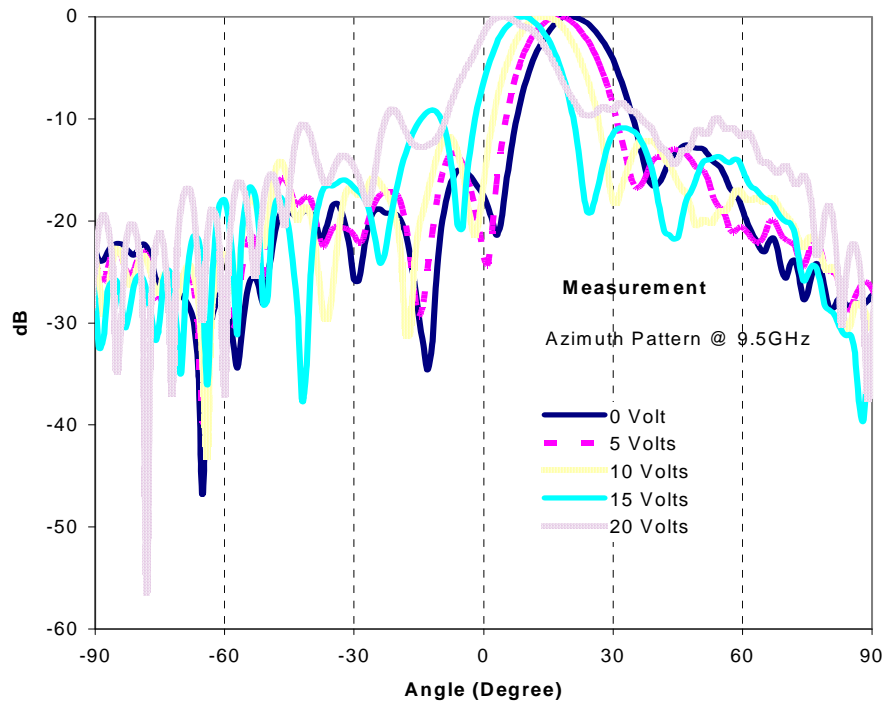


Figure 5.22 E-Plane Electric Field Pattern of Beam-Steerable Meanderline Array at 9.5 GHz Under Different Values of Bias Voltages

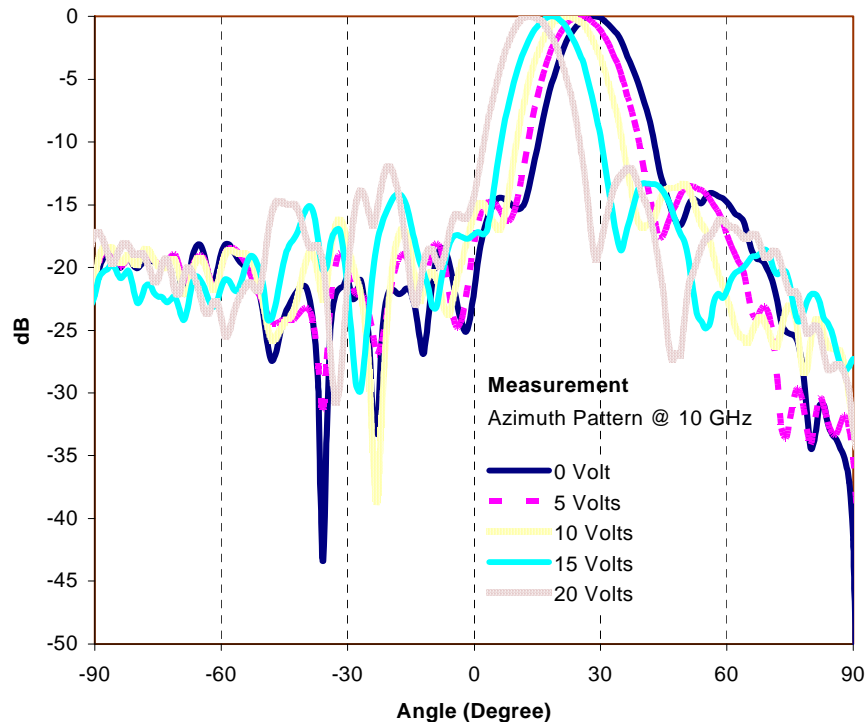


Figure 5.23 E-Plane Electric Field Pattern of Beam-Steerable Meanderline Array at 10 GHz Under Different Values of Bias Voltages

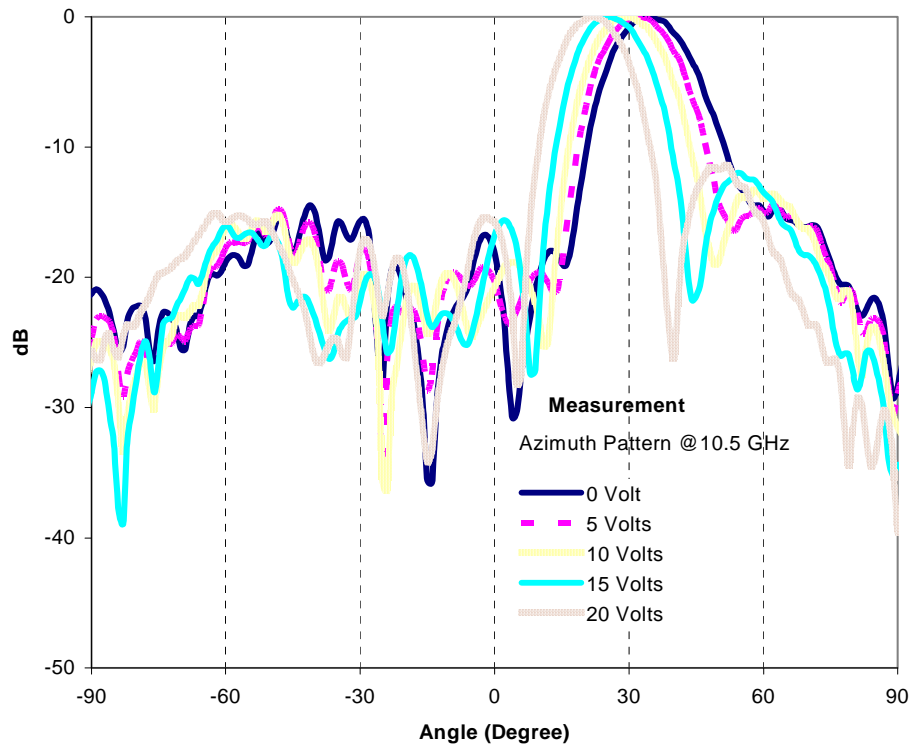


Figure 5.24 E-Plane Electric Field Pattern of Beam-Steerable Meanderline Array at 10.5 GHz Under Different Values of Bias Voltages

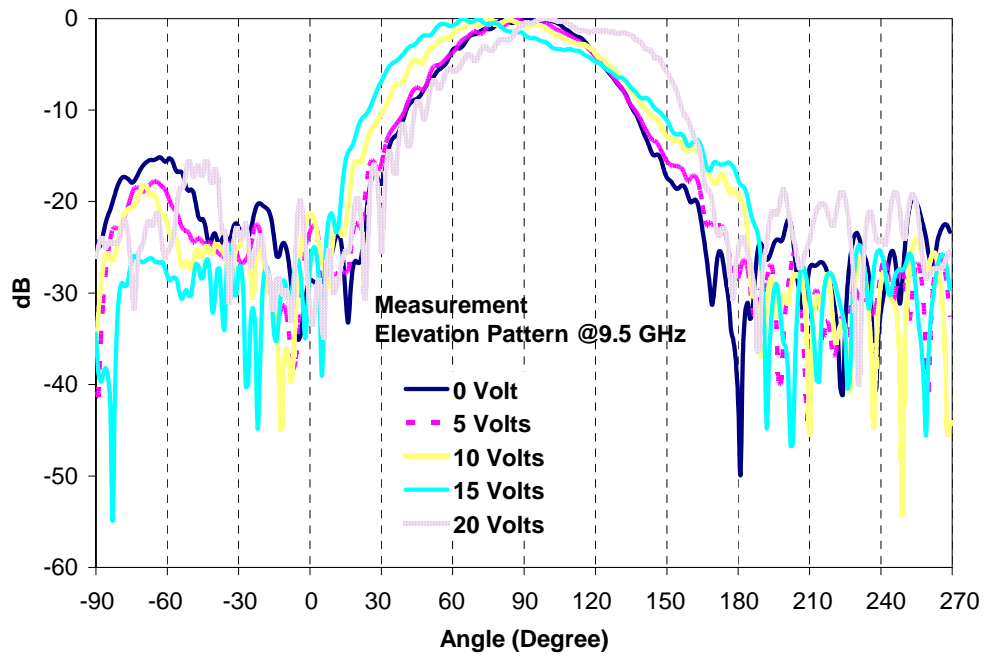


Figure 5.25 H-Plane Electric Field Pattern of Beam-Steerable Meanderline Array at 9.5 GHz Under Different Values of Bias Voltages

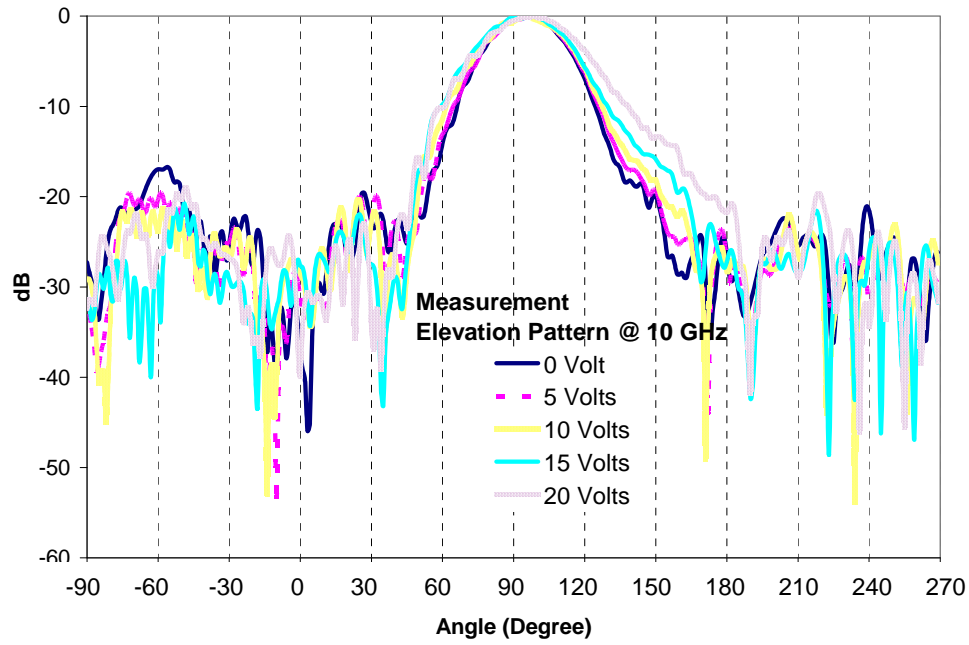


Figure 5.26 H-Plane Electric Field Pattern of Beam-Steerable Meanderline Array at 10.5 GHz Under Different Values of Bias Voltages

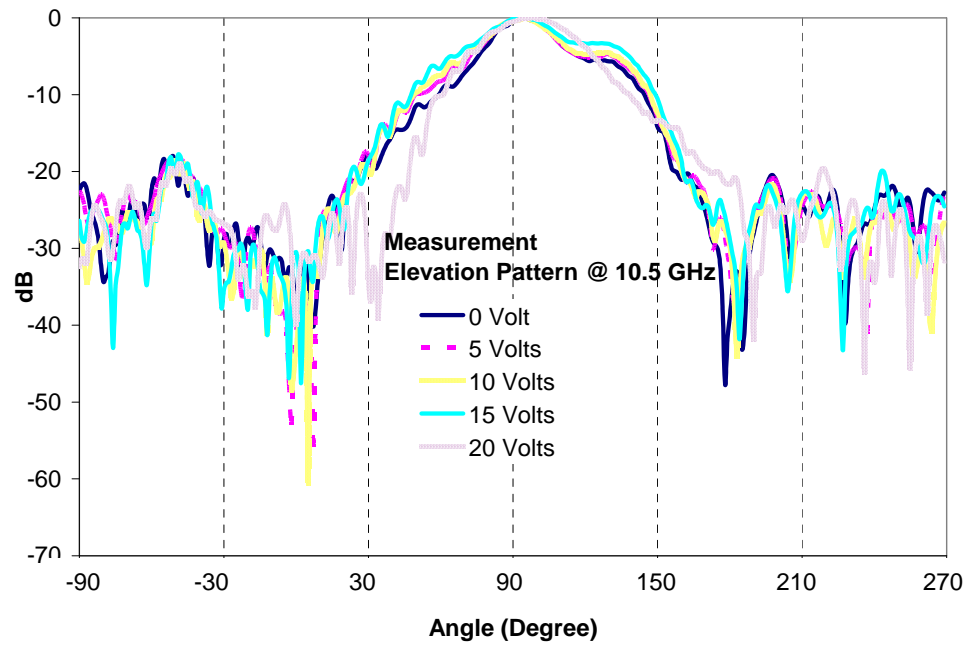


Figure 5.27 H-Plane Electric Field Pattern of Beam-Steerable Meanderline Array at 10.5 GHz Under Different Values of Bias Voltages

5.7 Further Investigations on Beam-Steerable Traveling Wave Meanderline Array

In previous section, it is shown that more than 10° beam steering can be achieved by loading the meandering sections with single varactor diode. As stated in Section 5.2, single varactor diode can provide 25° phase shift on the transmission line. On the other hand, in order to steer the beam of the meanderline array more than 10° , other phase shifting mechanisms can be used. In [32], it is stated that reflective type phase shifters can provide more than 60° phase tuning range.

To improve the beam scan range, a meanderline antenna with reflective type phase shifters has been designed. Reflective type phase shifter is composed of a hybrid-coupler and two identical tunable reflective loads. In order to realize tunable reflective loads, varactor diodes are utilized.

5.7.1 Varactor Diode Loaded Branch-Line Coupler Phase Shifters

Branch-line coupler is a narrowband device and can be used as power divider if it is designed as 3-dB directional coupler. In the case of 3-dB directional coupler which is called hybrid junction, power incident in port 1 is coupled to port 2 and port 3 but not into port 4 since it is the isolated port. Theoretical analysis of 3-dB branch-line coupler is investigated in detail in [31].

Design of narrowband branch-line coupler has been performed using Ansoft Designer. Operation frequency of the branch-line coupler has been set to 10 GHz. ROGERS 5880 Duroid with 15-mil thick ROGERS 5880 Duroid with dielectric constant $\epsilon_r=2.2$ is selected as substrate due to its low dielectric loss.

Ansoft Designer schematic model of the branch-line coupler is illustrated as in Figure 5.28. Theoretically, to realize a 3-dB branch-line coupler, the impedance of the branches should be set as;

$$Y_1 = Y_0 * \sqrt{2}$$

$$Y = Y_0$$

Length of the branch-line sections should be equal to;

$$l_1 = l_2 = \lambda_g/4;$$

Therefore, dimensions of the branch-line coupler are; $l_1 = l_2 = 5.75$ mm and $w_1 = 1.17$ mm, $w_2 = 1.9$ mm.

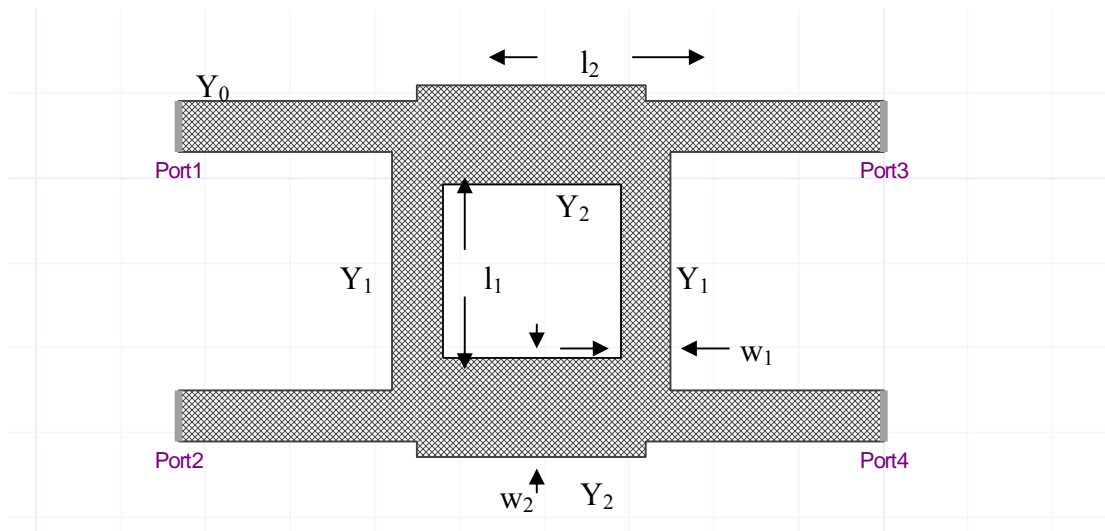


Figure 5.28 Ansoft Designer Model of 3-dB Branch-Line Coupler

Simulations of the 3-dB branch-line coupler have been performed between 6-15 GHz in Ansoft Designer. In Figure 5.28, S-parameters of branch-line couplers are presented. Return loss of the coupler (S11) is below -20 dB around 10 GHz. Power incident in port 1 is equally coupled to port 3 and port 4 and less than -20 dB of power is coupled to the isolated port (port 2).

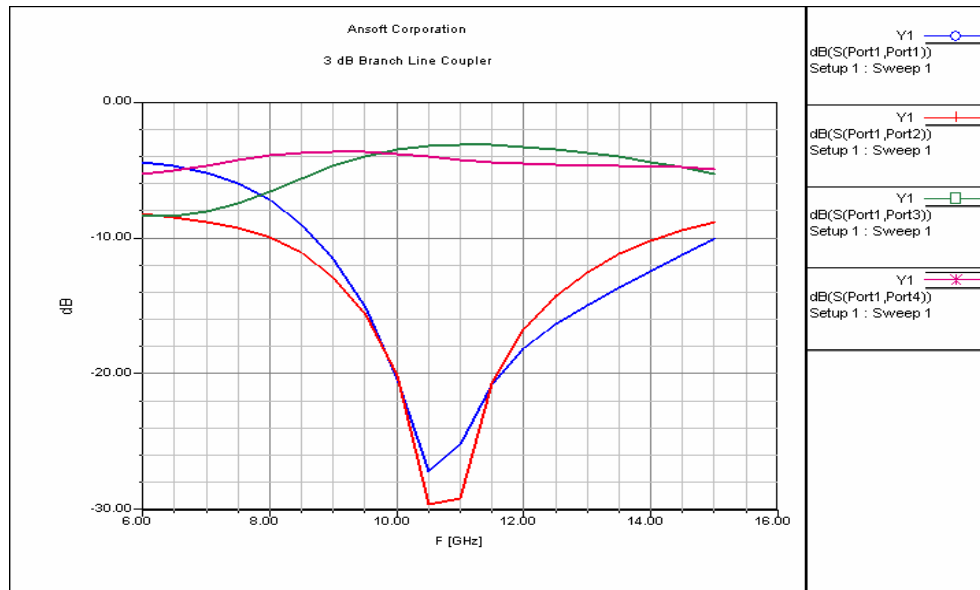


Figure 5.29 Ansoft Designer S-Parameter Simulation of 3-dB Branch-Line Coupler

As mentioned above, reflective type phase shifter is composed of 3-dB branch-line coupler loaded with varactor diodes. The analysis of reflective type phase shifter has been carried out in Ansoft Designer.

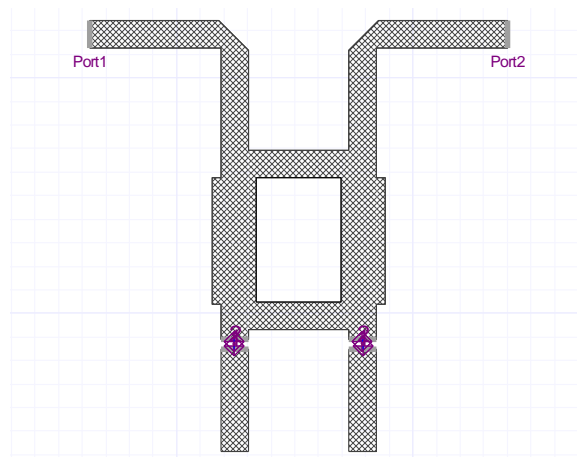


Figure 5.30 Ansoft Designer Model of Reflective Type Phase Shifter Loaded with Varactor Diodes

During the simulations of reflective type phase shifter, instead of varactor diodes, S-parameters of different capacitance values are inserted into 2-port boxes and these

boxes are connected to branch-line sections as shown in Figure 5.30. For different values of varactor capacitance, phase variation between port 1 and port 2 has been simulated. In simulations, varactor capacitance has been tuned between 0.3 pF to 2.7 pF and more than 70° phase variation has been observed as shown in Figure 5.31.

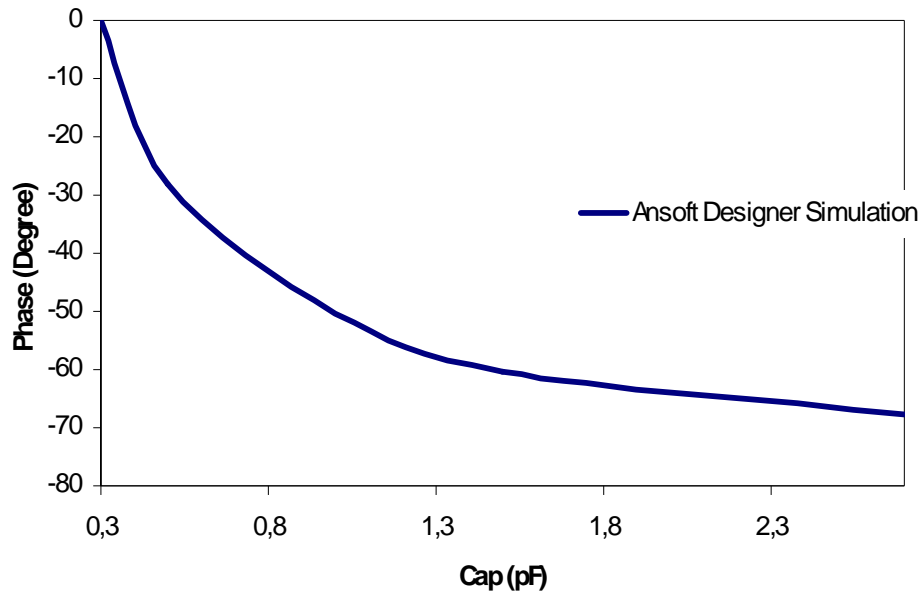


Figure 5.31 Ansoft Designer Simulation of Branch-Line Coupler Phase Variation with respect to Varactor Capacitance

5.7.2 Application of Phase Shifter on Traveling Wave Arrays

In order to achieve more beam-steering, varactor diodes in the previous design can be replaced by varactor diode loaded branch-line coupler type phase shifters, as shown in Figure 5.32.

Analysis of meanderline array with varactor diode loaded branch-line coupler type phase shifter has been performed using Ansoft Designer.

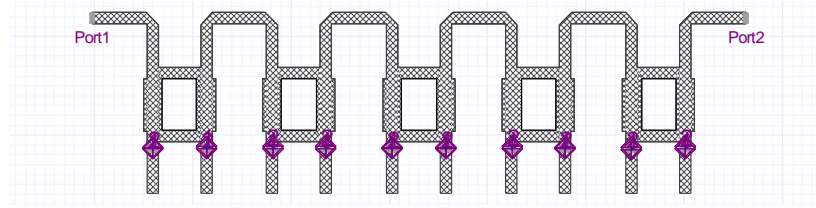


Figure 5.32 Meanderline Array with Varactor Diode Loaded Branch-Line Coupler Phase Shifter

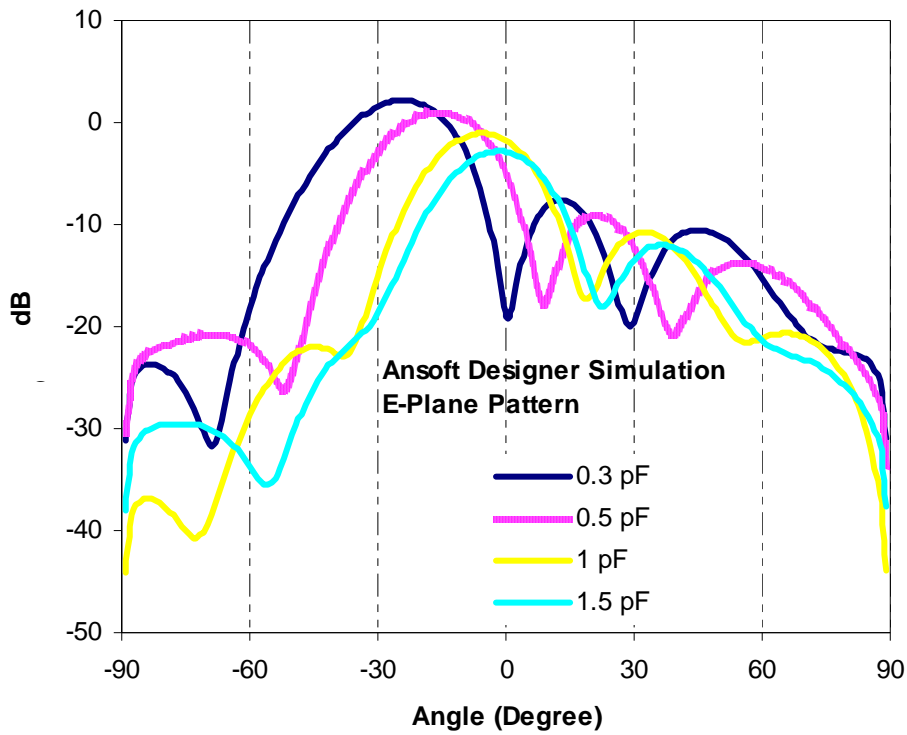


Figure 5.33 E-Plane Electric Field Pattern of Beam-Steerable Meanderline Array for Different Values of Varactor Capacitance (Ansoft Designer Simulation)

In Figure 5.33, patterns of the meanderline array with reflective type phase shifter are given for different capacitance value. Direction of the radiation beam steers from 24° to broadside 0° . On the other hand, while the beam is sweeping, the gain of the array decrease significantly.

To sum up, varactor diode loaded branch-line coupler phase shifters have wide phase-tuning range as shown in simulations. It is possible to use these types of phase

shifters in traveling wave meanderline arrays. However, since the branch-line coupler is physically large, placing the phase shifters between elements can be a problem. Furthermore, such a structure on the radiating part of the antenna may affect the radiation pattern as well. Thus, further investigations should be performed throughout the implementation processes.

CHAPTER 6

Dual CP Polarized Traveling Wave Meanderline Array using RF MEMS Technology for X-Band Applications

As mentioned in Chapter 2, polarization of the antenna is defined as the polarization of the wave transmitted (radiated) by the antenna and it is one of the important design parameters of the antennas in systems. Especially, polarization reconfigurability increases the degree of freedom of the antenna while sending and receiving signals with different polarizations. For instance, slant polarized antennas are able to receive both vertical and horizontal polarizations. It is possible to achieve polarization reconfigurability in antennas by using electrical and mechanical devices such as switches, loads etc. Particularly, RF MEMS switches have proven their usefulness, due to their small size, low insertion loss, high linearity and improved performance. RF MEMS devices are commonly used in frequency, polarization and radiation pattern reconfigurable antennas ([6], [7], [10])

Traveling wave meanderline arrays are microstrip structures and it is easy to integrate components on them. Consequently, it is rather easy to implement reconfigurable meanderline array structures as demonstrated in Chapter 5. Another advantage of meanderline arrays is that their polarizations can be controlled by tuning the dimensions of the meanderline sections. As explained in Section 3.2.1, if the dimensions of the meanderline array are $s=\lambda_g/2$, $d=\lambda_g/4$, and $l=3\lambda_g/4$, polarization of the meanderline array becomes circular.

In this chapter, a polarization-agile meanderline array has been investigated. Single meanderline array has been designed as circularly polarized antenna and by using RF MEMS switches its polarization can be set as either RHCP (Right Hand Circularly Polarized) or LHCP (Left Hand Circularly Polarized).

In Figure 6.1, schematic view of dual circularly polarized meanderline array is presented. Meanderline array consists of upper and lower meanderline sections and SPDT RF MEMS switches are placed at the connection point of meanderline sections. If the upper section of the meanderline array is switched, polarization of the array is RHCP and otherwise array is LHCP.

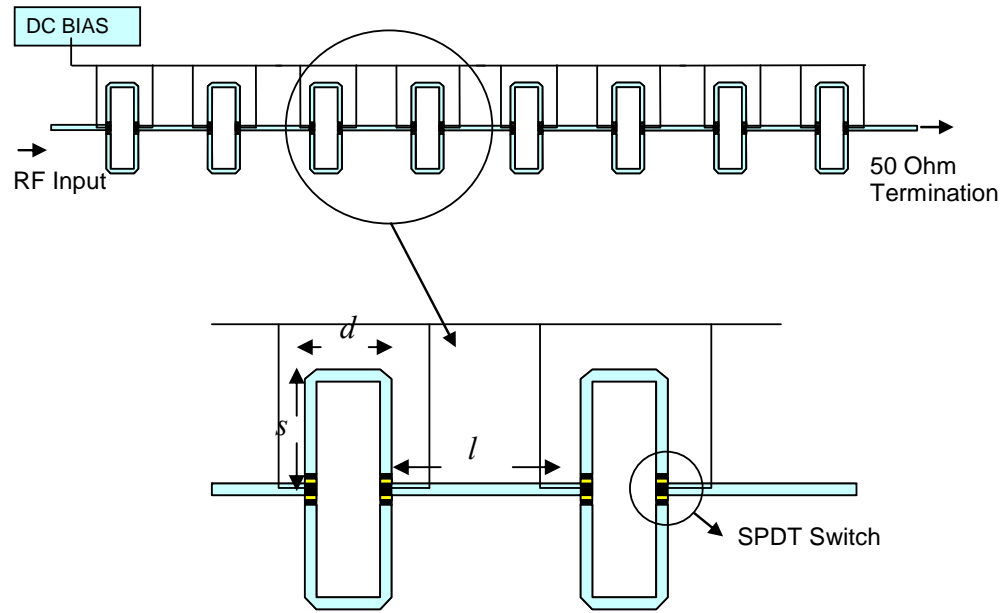


Figure 6.1 The Schematic View of Polarization-Agile Meanderline Array

Electromagnetic analysis of the polarization-agile meanderline array has been performed using Ansoft HFSS. Antenna has been designed on 15-mil thick ROGERS 5880 Duroid with $\epsilon_r=2.2$. Operation frequency of polarization-agile meanderline array is set to 10 GHz and polarization is circular. Impedance of the meanderline sections are 50 Ω and the width of the microstrip segments is equal to 1.17mm. Dimensions of the meanderline sections are set as $s=10.9\text{mm}$, $d=5.45\text{mm}$ and $l=16.35\text{mm}$ to achieve circular polarization.

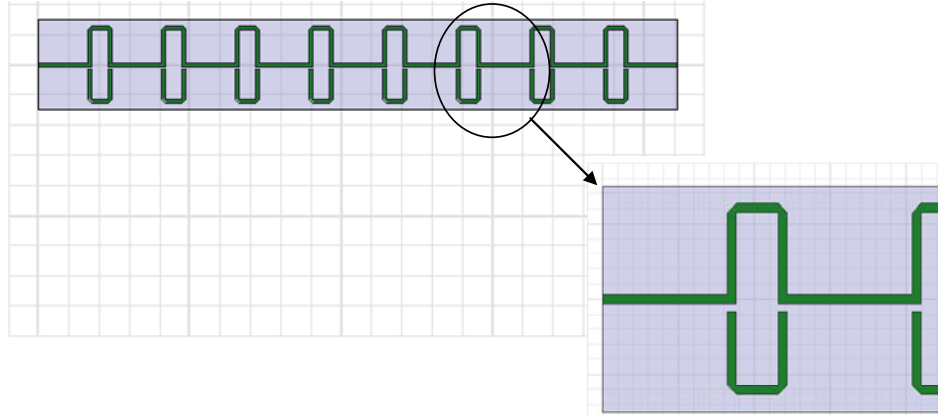


Figure 6.2 HFSS Model of the Polarization-Agile Meanderline Array

As illustrated in Figure 6.2, down states of MEMS switches are modeled by short metallic parts and up states of switches are left as open. S-parameter, radiation pattern and polarization characteristics of the polarization-agile array have been investigated at 10 GHz.

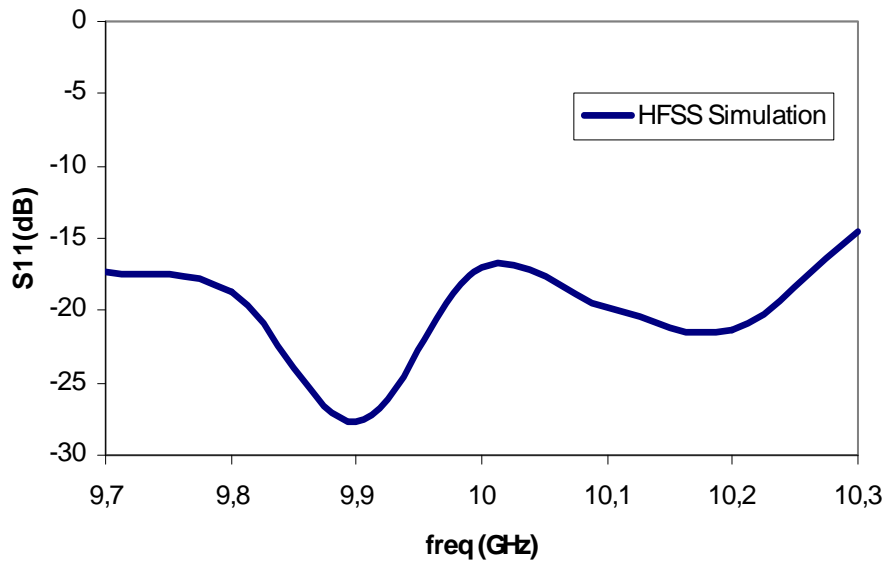


Figure 6.3 S11-Parameter Simulation of Polarization-Agile Meanderline Array

Return loss of the polarization-agile meanderline array is given illustrated in

Figure 6.3 between 9.7 to 10 GHz. Return loss of the array is well below -10 dB in the operation band.

E-plane pattern of the polarization-agile meanderline array at 10 GHz is shown in Figure 6.4. As seen from the pattern, the main beam of the array is directed toward 14° and 3-dB beam width is about 8° . Also, the shoulder around -100° is due to the placement of meanderline array elements. As mentioned in Chapter 3, meanderline array can be modeled with magnetic current elements. When the array factor of the array is calculated, grating lobes are observed.

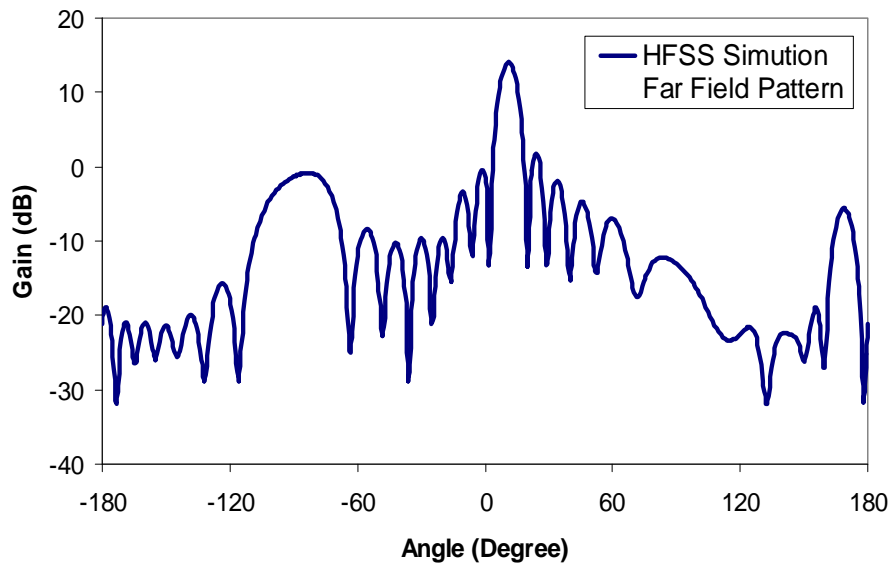


Figure 6.4 E-Plane Co-Polarization Pattern of Polarization-Agile Meanderline Array at 10 GHz

In addition, axial ratio of the meanderline array has been calculated around the main beam and given in Table 6.1. Around the main beam, axial ratio equals to 3 dB and axial ratio get worse towards 10° . In addition, when the switches select one array, other portion of the array will form open stubs. These sections disturb polarization of the array as well.

Table 6.1 Axial Ratio of the Polarization-Agile Meanderline Array around Main Beam at 10 GHz

Angle (Degree)	Axial Ratio (dB)
10°	3.24
11°	3.17
12°	3.07
13°	2.94
14°	2.77
15°	2.56
16°	2.28
17°	1.88
18°	1.3

As shown in Table 6.2, for the 1st state, upper part of the meanderline array is selected and the antenna is RHCP. In this case, the antenna receives RHCP signal with 16 dB of gain and LHCP signal 32 dB below. In a similar manner, when the 2nd state is selected, antenna is LHCP.

Table 6.2 Simulation of LHCP and RHCP values for the 1st and 2nd States of RF MEMS Switches

	1 st State	2 nd State
LHCP(dB)	-16 dB	16 dB
RHCP(dB)	16 dB	-16 dB

In summary, a polarization-agile meanderline array with SPDT RF MEMS switches has been proposed. Polarization of the meanderline array can be altered by selecting different paths of the meander line array. If the upper part of the array is selected by MEMS switches, antenna polarization becomes RHCP and if lower part of the meanderline array is selected, polarization turns out to be LHCP. Simulation of the polarization-agile array has been performed using Ansoft HFSS without MEMS switches and operation of the antenna has been verified.

CHAPTER 7

Dual Frequency Slot Dipole Array for X- and Ka- Band Applications

Frequency reconfigurable antennas are very attractive in many fields such as communication, radar and satellite applications. Reconfigurability can be provided by switches, loads etc. MEMS (MicroElectroMechanical Systems) devices have proven their usefulness in microwave applications with their reduced cost, improved performance, and miniaturized dimensions. A dual frequency reconfigurable slot dipole array with a CPW-based feed using RF MEMS technology for X- and Ka-band applications has been designed in [6]. In [6], the array has been designed on 500 μm -thick 4" glass substrate with $\epsilon_r=4.6$ ($\tan\delta=0.005$) and MEMS switches are monolithically integrated on the glass substrate. Operation of MEMS switches is summarized in Appendix E. The antenna proposed in this thesis, based on [6], is designed on 25 mil-thick Rogers 6006 Duroid ($\epsilon_r=6.15$) substrate and packaged MEMS switches will be implemented on the array. Prototype fabrication and measurements of single- and 2-element dual-frequency slot dipole antennas are introduced in this chapter.

The dual frequency array is composed of 2 linearly placed frequency-tunable slot dipole elements and a CPW-based feed network including 50- Ω /100- Ω dual-frequency transformers, chamfered CPW right-angle bends and T-junction. Coplanar waveguide (CPW) transmission lines have been used in the corporate feed network of 2-element linear array due to its advantages over a microstrip feeding network, such as low radiation losses, less dispersion, easier combination with active devices. Figure 7.1 shows the schematic view of the dual-frequency array.

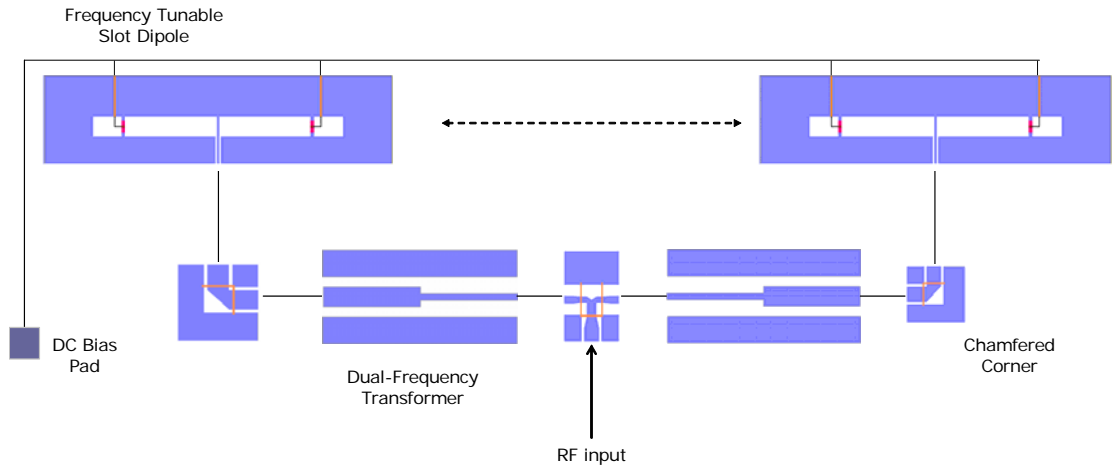


Figure 7.1 The Schematic View of 2-Element Reconfigurable Slot Dipole Antenna Array Structure with MEMS Switches

7.1 Reconfigurable Slot Dipole Antenna

Figure 7.2 shows the CPW fed slot dipole antenna structure used in the array [6]. For the implementation of these antennas, a 25 mil-thick Rogers 6006 Duroid ($\epsilon_r=6.15$) substrate with 0.5 Oz Copper has been used. The slot dipole antennas can operate at X- and Ka- band with the aid of RF MEMS switches located on the slot arms. Operation frequency of the slot antennas is determined by the length of the slots. Also, it is stated in [6] that in addition to the length of the slots, height of the dielectric substrate controls the resonance frequency. Slot width and feed line parameters control the return loss level. In fact, slot dipole antennas exhibit 40-70 Ω input impedance when the total length is about 0.8-0.9 λ_g at the frequency of interest. The total length of the dipole is equal to 0.7 λ_g (2*L1) when the switches are in up state and equal to 0.7 λ_g (2*L2) when the switches are in down state.

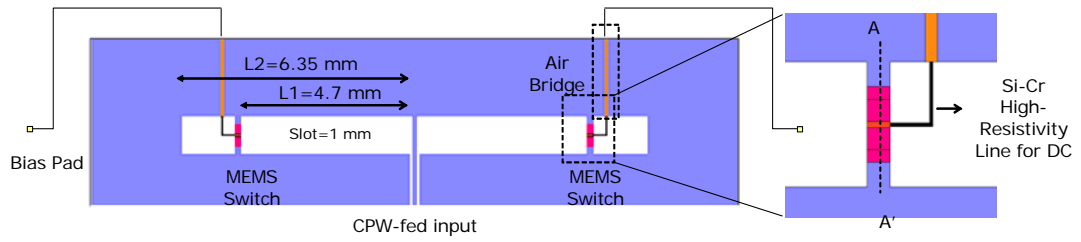


Figure 7.2 The Schematic View of Reconfigurable Slot Dipole Antenna with MEMS Switches Located on the Arms to Control Resonant Frequency

Throughout the design procedure of the antenna, the related analysis is performed using, Ansoft HFSS. Simulations are validated by comparing the measurements performed with the slot dipole antennas manufactured on the Rogers 6006 Duroid. Photographs of the fabricated antennas are given in Figure 7.3.

As shown in Figure 7.3, for up-state and down-state cases of RF MEMS switches two different prototypes have been manufactured. The down state case of the RF MEMS switches are modeled by short metallic parts as in Figure 7.3 (b) and up state of the switch is left as open as in Figure 7.3 (a).

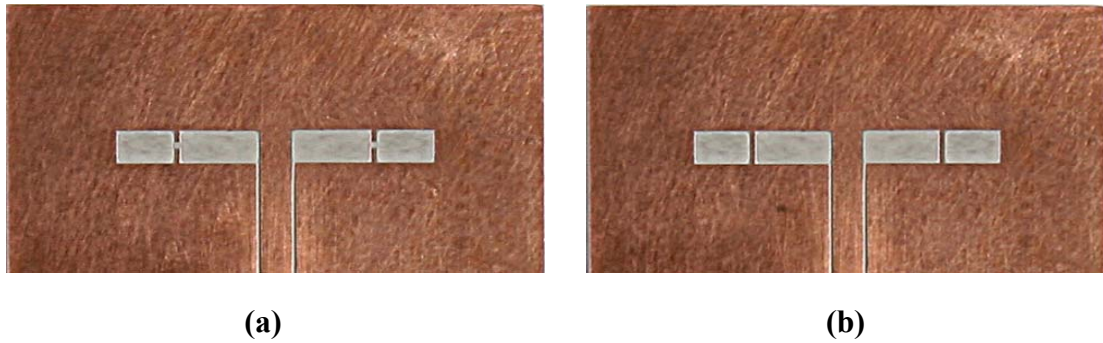


Figure 7.3 Prototype structures of slot dipole antenna with metallic strips instead of RF MEMS switches

(a) Switches Up Position (b) Switches Down Position

S11 values obtained by measurements and HFSS simulations are given in Figure 7.4. As seen from the figure, simulation results are in good agreement with the measurements. The antenna manufactured for the up-state case of switches resonates

at 10 GHz and the antenna manufactured for the down-state case of switches resonates at 15.4GHz as expected.

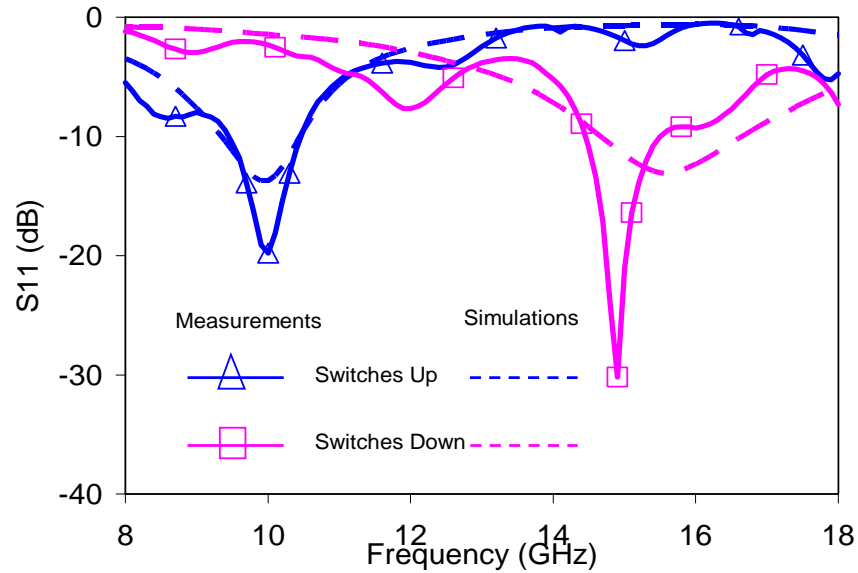


Figure 7.4 Measurement and simulation results of a slot dipole antenna with metallic strips instead of RF MEMS switches

Far field measurements of the prototype structures have been performed in the tapered anechoic chamber and shown in Figure 7.5-Figure 7.8. E-plane and H-plane measurements at 10 GHz for the up-state case and 15.4 GHz for the down-state case show good agreement with HFSS simulations.

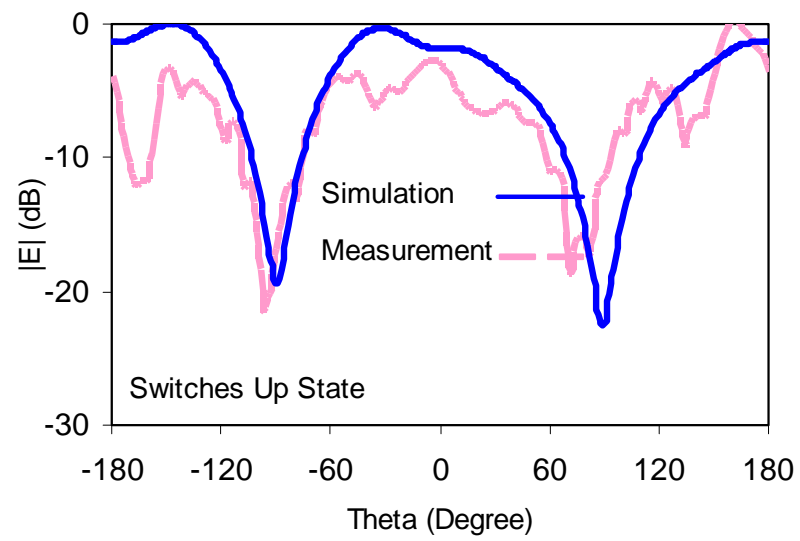


Figure 7.5 E-Plane Electric Field Pattern of Single Dipole Antenna at 10 GHz for the Switches are Up-State Case

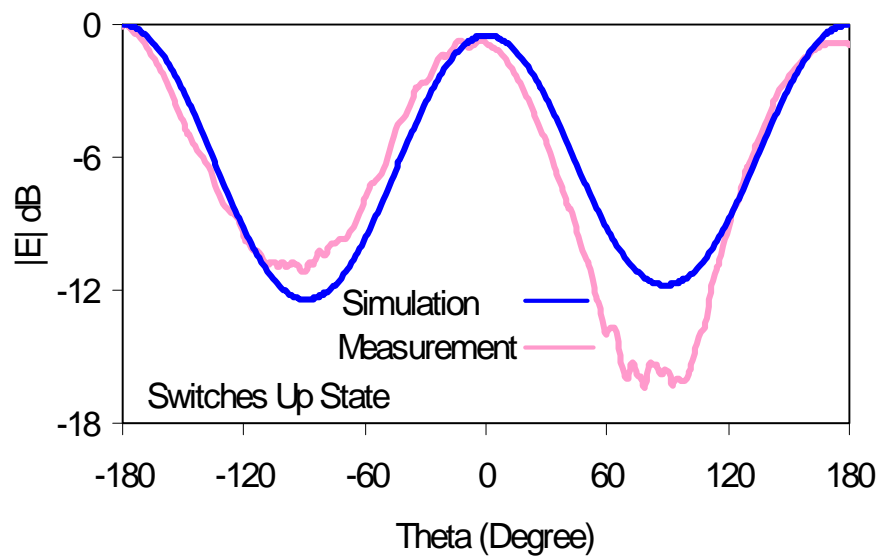


Figure 7.6 H-Plane Electric Field Pattern of Single Dipole Antenna at 10 GHz for the Switches are Up-State Case

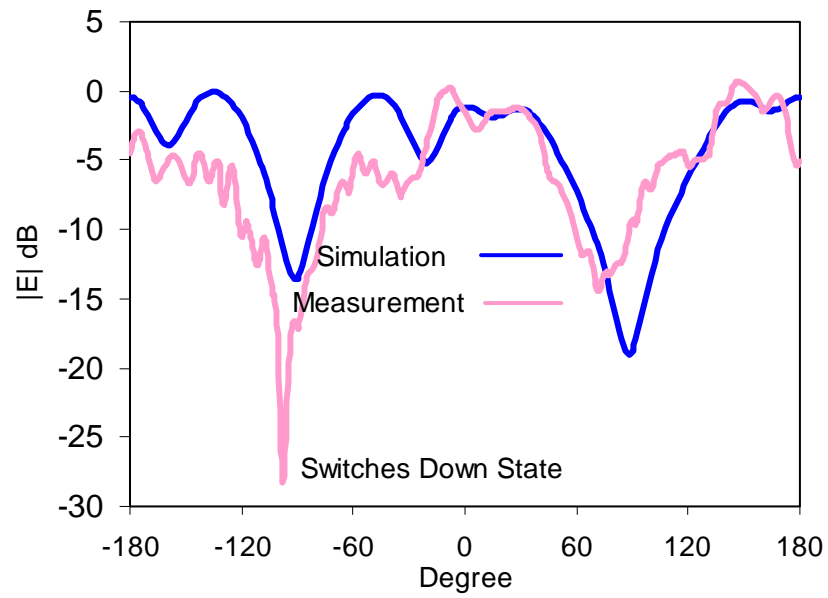


Figure 7.7 E-Plane Electric Field Pattern of Single Dipole Antenna at 15.4 GHz for the Switches are Down-State Case

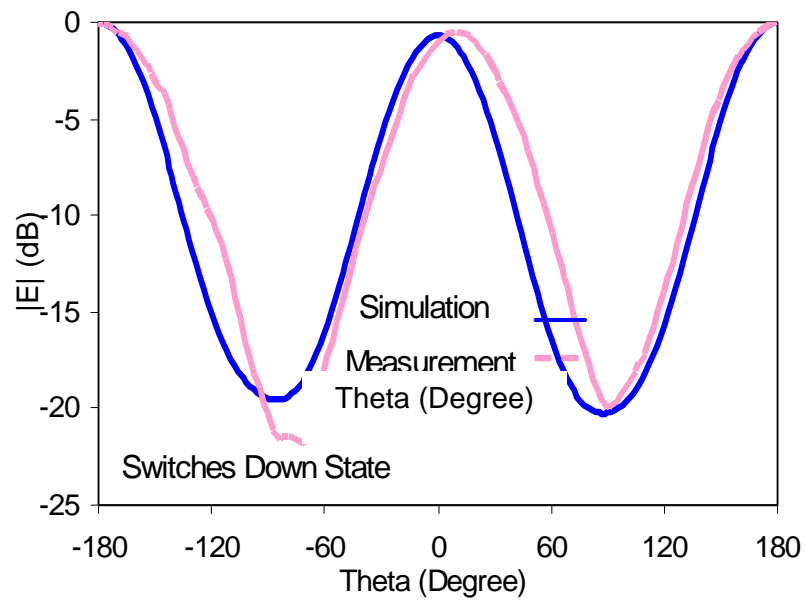


Figure 7.8 H-Plane Electric Field Pattern of the Single Dipole Antenna at 15.4 GHz for the Switches are Down-State Case

7.2 CPW-Based Feed Network

As mentioned in the introduction part, the feed network of the array is CPW-based that offers many advantages such as; low radiation losses, and less dispersion. The CPW-based feed network includes T-junctions, chamfered corners, and dual frequency transformers to match the input impedance at both resonant frequencies of the antennas.

Dual-frequency transformer

Generally, quarter-wave frequency transformers are used to match the impedance of a line at a single frequency. In fact, it is possible to design an electrically small transformer with two sections and achieve ideal impedance matching at two arbitrary frequencies. The dual frequency transformer presented in this study is used to transform 50-Ω input impedance of the antennas to 100-Ω impedance at the two ports of the T-junction [35]. Transformer has been designed on 500 μm-thick 4" glass substrate with $\epsilon_r=4.6$ ($\tan\delta=0.005$) and manufactured in [35]. The transformer, which is designed to operate both in X- and Ka-band, is realized using two equal-length sections of CPW lines with different characteristic impedances. The circuit schematic and parameters of the designed transformer are given in Figure 7.9.

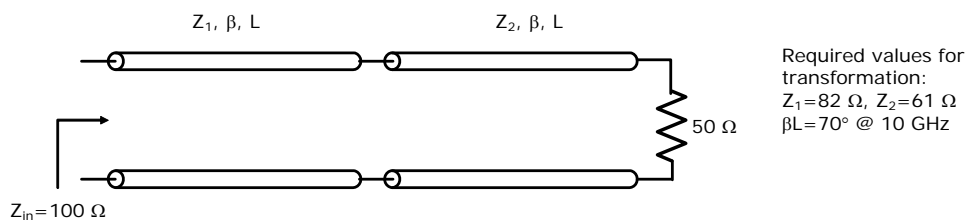


Figure 7.9 The Circuit Schematic View and Parameters of the Dual-Frequency Transformer

Also, dual frequency transformer has been manufactured and measurement results have been presented in [6]. As shown in Figure 7.10, HFSS simulations of the dual-frequency transformer are consistent with the measurements. Dual frequency

impedance transformers providing a return loss better than 15 dB at the frequency of interest.

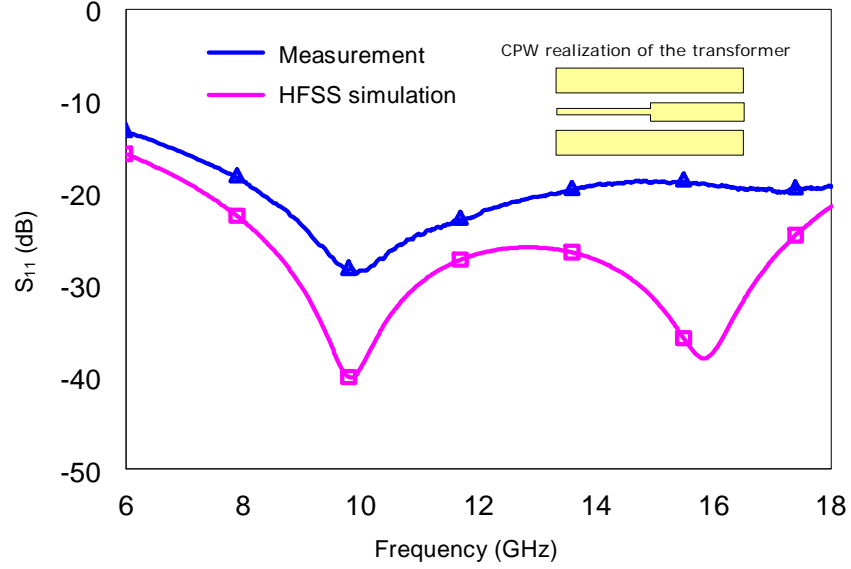
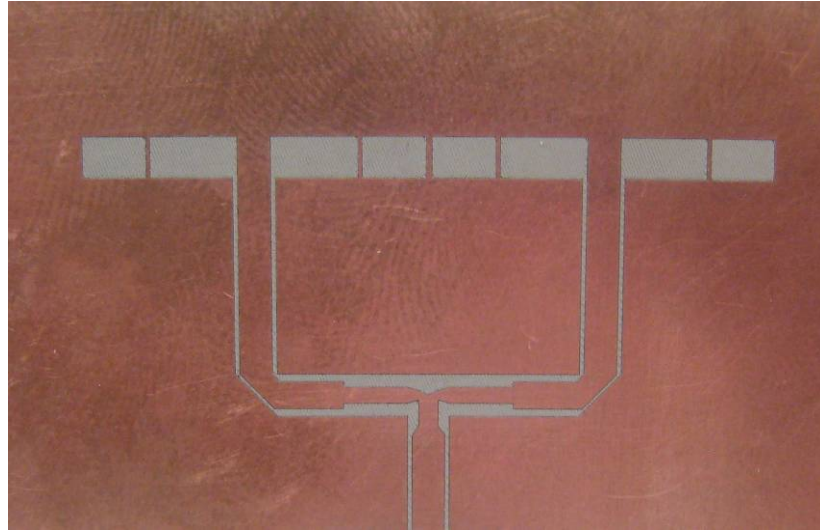


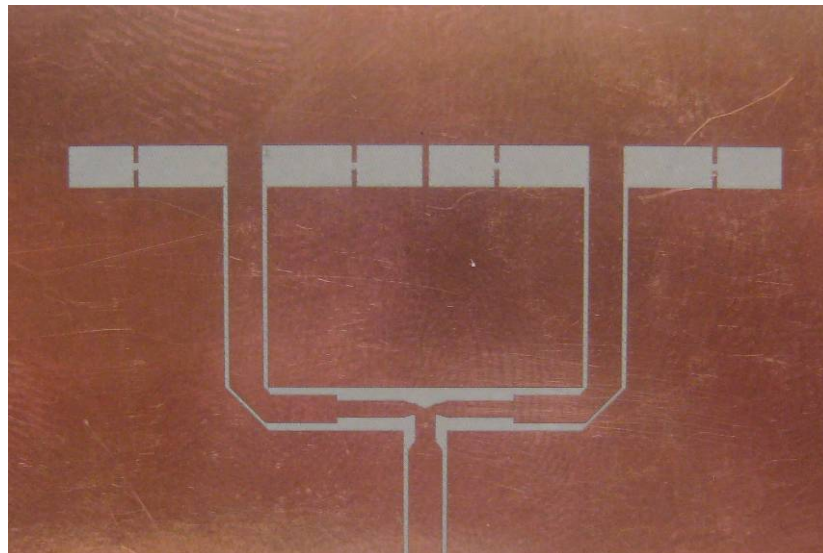
Figure 7.10 Measurement and simulation results of dual-frequency transformer operating at X- and Ka- Band

7.3 Two Element Slot Dipole Dual-Frequency Array Structure

Prototype structures of 2-element reconfigurable slot dipole antenna array structure have been manufactured on the 20 mil Rogers 6006 Duroid substrate. Photographs of the manufactured antennas for up-state and down-state cases of switches are given in Figure 7.11(a) and Figure 7.11 (b), respectively.



(a)



(b)

Figure 7.11 Prototype Structures of 2-Element Reconfigurable Slot Dipole Antenna Array with Metallic Strips Instead of RF MEMS Switches
(a) Switches Up-State Case. (b) Switches Down-State Case

The reflection coefficient measurements of the 2-element slot dipole antenna structure are performed using Agilent N5230A PNA-L 10 MHz-40GHz Network Analyzer. Figure 7.12 shows S11 measurements of the prototype structures for the up and down cases. For the up-state case resonance frequency of the antenna array is at

10.6 GHz and for the down-state case it is 15.9 GHz. However, there is a resonance around 10.5 GHz for the switches down state case. This resonance behavior should be investigated further.

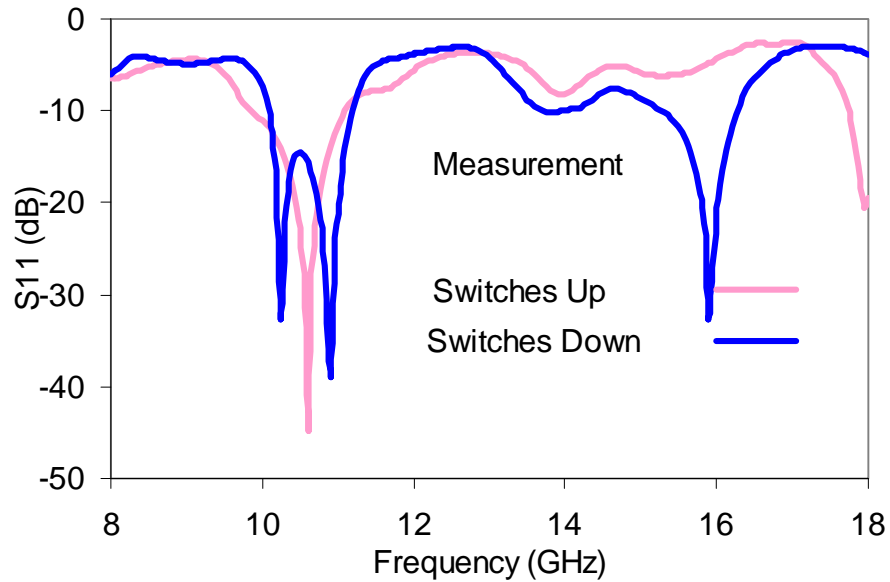


Figure 7.12 S11 Measurement Results of 2-Element Slot Dipole Antenna Array with Metallic Strips instead of RF MEMS Switches

Array structure far field pattern measurements have been performed in the tapered anechoic chamber. E-plane and H-plane patterns for the up-state and down-state cases are presented in Figure 7.14-Figure 7.16. For the up-state case E- and H- plane patterns have been measured at 10.6 GHz. As shown in Figure 7.13, E plane pattern of the array is similar to single slot dipole element. On the other hand, H-plane pattern of the array is more directive than a single element as expected. H-plane patterns at 15.9 GHz are consistent with the previous measurements. The asymmetry of the E-plane measurements can be attributed to feeding network.

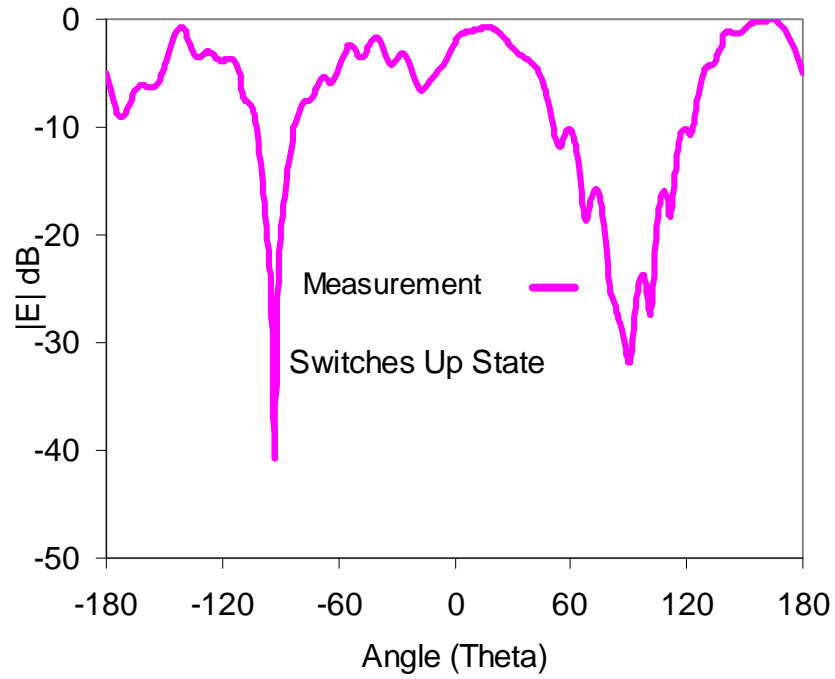


Figure 7.13 E-Plane Electric Field Pattern of 2-Element Antenna Array Structure at 10.6 GHz for the Switches are Up-State Case

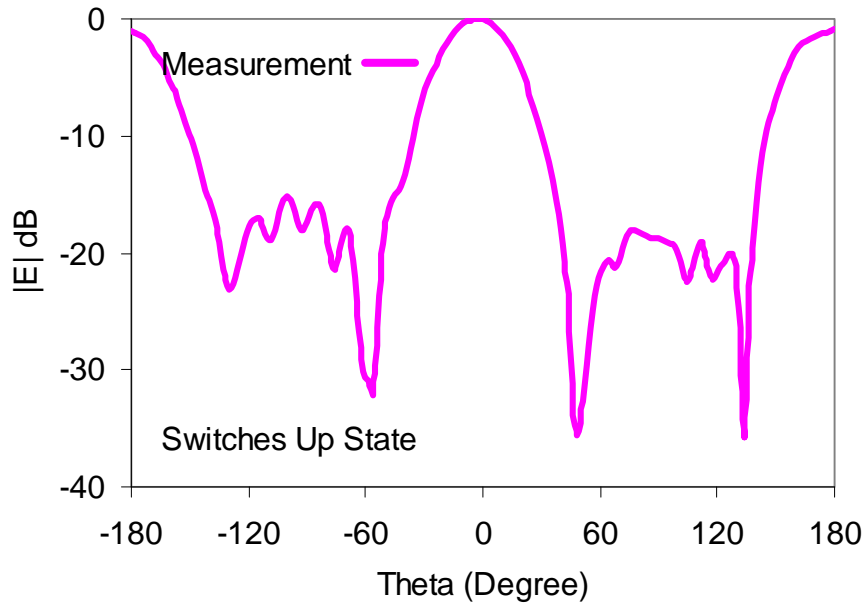


Figure 7.14 H-Plane Electric Field Pattern of 2-Element Antenna Array Structure at 10.6 GHz for the Switches are Up-State Case

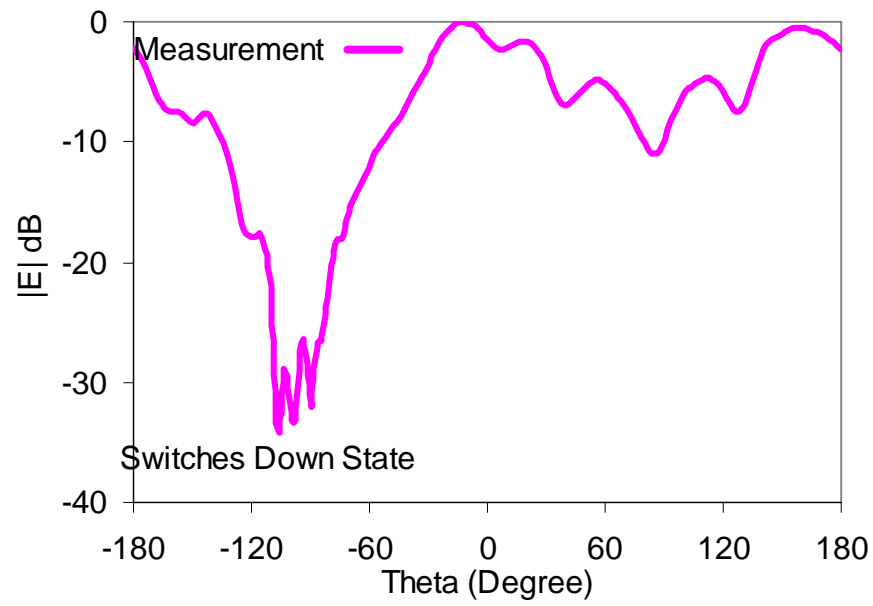


Figure 7.15 E-Plane Electric Field Pattern of 2-Element Antenna Array Structure at 15.9 GHz for the Switches are Down-State Case

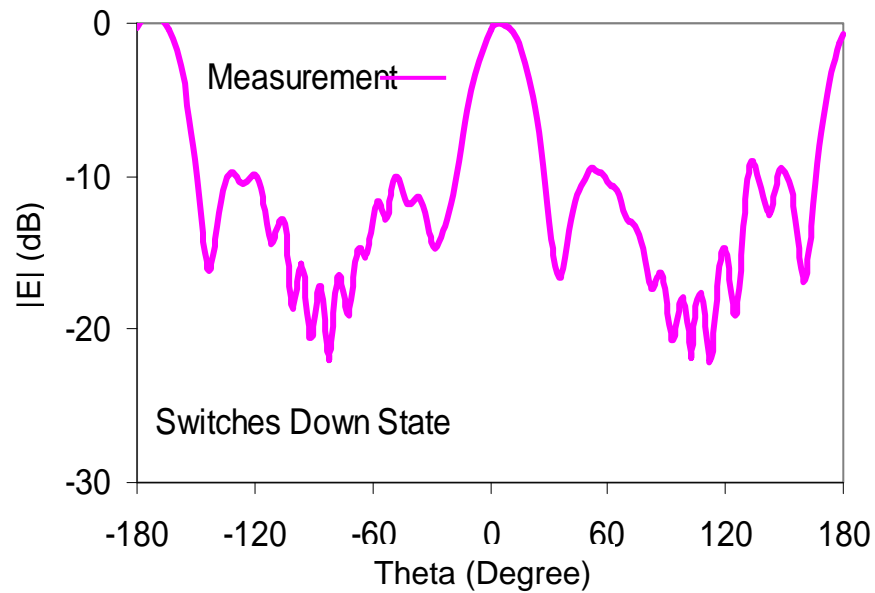


Figure 7.16 H-Plane Electric Field Pattern of 2-Element Antenna Array Structure at 15.9 GHz for the Switches are Down-State Case

In conclusion, a reconfigurable dual frequency slot dipole array operating at X- or Ka-band slot dipole antennas has been presented. It is possible to increase the number of elements in the array structure to enhance the directivity of the antenna array. In the future, commercial packaged MEMS switches will be integrated to the array.

CHAPTER 8

CONCLUSION

In this thesis, three different reconfigurable antenna structures, a beam-steerable traveling wave meanderline array with varactor diodes, dual circularly polarized meanderline array and frequency-tunable slot dipole array have been designed and investigated.

First, a linearly polarized meanderline array operating at 10 GHz has been designed by using previously introduced EM models. Then, final design parameters are obtained using full wave EM simulators, Ansoft Designer and Ansoft HFSS. Designed meanderline array has been manufactured and its S-parameters and radiation patterns have been measured. It has been shown that measurement results are in good agreement with the simulations.

Beam-steerable meanderline array has been designed, manufactured and measured. 10° beam scanning has been achieved by using reverse-biased varactor diodes. It has been shown that measurement results agree well with simulations. Since the varactor diodes are placed in series with the array, impedance of the varactor changes with applied voltage, so that return loss and S21 characteristics of the array change with applied voltage. In order to achieve beam-steering more than 10°, a reflective type phase shifter has been introduced. Reflective type phase shifter consists of a 3-dB branch-line coupler loaded with varactor diodes and has a phase tuning range of more than 60°. Reflective type phase shifters have been placed between meanderline unit cells and simulations have been performed. More than 20° beam-steering has been achieved in simulations. Reflective type phase shifters are commonly used in reconfigurable antennas. On the other hand, their sizes are large compared to wavelength making them inappropriate to use in small configurations.

A dual circularly polarized meanderline array has been designed and simulated in Ansoft Designer. Antenna polarization can be switched between LHCP and RHCP by using SPDT RF MEMS switches. In the simulations, down state of MEMS switches has been modeled by metallic parts replacing switches and in the up state switch locations have been left as open. Axial ratio around 3dB has been obtained, which is an acceptable value for circular polarization. Dual CP polarization has been verified by simulations.

Reconfigurable dual frequency slot dipole array has been designed for X- and Ka-band applications. Dual frequency operation of the antenna array has been achieved using RF MEMS switches located on slots. The corporate feed network of the array has been realized with coplanar wave transmission. Prototypes of single-element and two-element slot dipole array have been manufactured representing the corresponding structures with upstate and down state of MEMS switches. It has been shown that the array is operating at 10 GHz and 15 GHz for up state and down state of switches, respectively. The measurement results show very good agreement with the simulation results.

Dual Circularly polarized meanderline array and reconfigurable slot dipole array will be fabricated with packaged MEMS switches in a hybrid fashion. Packaged RF-MEMS switches are very recently available on the market. In fact, during the last months of this study there is only one company, RADANT MEMS Inc., which sells only SPST switches abroad. Therefore realization of dual CP antenna and dual frequency slot array will be performed in future.

REFERENCES

- [1] J. T. Bernhard, "Reconfigurable Antennas", Morgan & Claypool Publishers series, 2007.
- [2] J.Kiriazzi, H.Ghali, H.Radaie, and H. Haddara, "Reconfigurable dual-band dipole antenna on silicon using series MEMS switches," Proceedings of the IEEE/URSI International Symposium on Antennas and Propagation, vol.1, pp.403–406, 2003.
- [3] M.A. Ali and P. Wahid, "A reconfigurable Yagi array for wireless applications," Proceedings of the IEEE/URSI International Symposium on Antennas and Propagation, vol.1, pp. 466–468, 2002.
- [4] S. Liu M-J. Lee, C. Jung, G-P. Li, and F. De Flaviis, "A Frequency-Reconfigurable Circularly Polarized Patch Antenna by Integrating MEMS Switches", Proceedings of the IEEE/URSI International Symposium on Antennas and Propagation, Vol. 2A, pp.413- 416, 3-8 July 2005.
- [5] C.W. Jung, M-J. Lee, F. De Flaviis, "Reconfigurable dual-band antenna with high frequency ratio (1.6:1) using MEMS switches", Electronics Letters, Vol.44, No.2, pp.76–77, January 17 2008.
- [6] Kagan Topalli, Ozlem Aydin Civi, Simsek Demir, Sencer Koc, and Tayfun Akin, "Dual-Frequency Reconfigurable Slot Dipole Array with a CPW-Based Feed Network using RF MEMS Technology for X- and Ku-Band Applications," *IEEE AP-S*, 2007
- [7] E. Erdil, K. Topalli, O. Aydin Civi, and T. Akin, "Reconfigurable CPW-fed dual frequency rectangular slot antenna," IEEE AP-S Symp. Digest, vol.2A, pp.392-395, 2005
- [8] R.N. Simons, D. Chun, and L.P.B. Katehi, "Polarization reconfigurable patch antenna using microelectromechanical systems (MEMS) actuators," Proceedings of the IEEE/URSI International Symposium on Antennas and Propagation, vol.1, pp.6–9, 2002.

- [9] X-S. Yang, B-Z. Wang, Wu, and S. Xiao, "Yagi Patch Antenna With Dual-Band and Pattern Reconfigurable", *IEEE Antennas and Wireless Propagation Letters*, Vol.6, pp.168-171, 2007.
- [10] K. Topalli, O. Aydin Civi, S. Demir, S. Koc, and T. Akin, "A Monolithic Phased Array using 3-bit Distributed RF MEMS Phase Shifters," *IEEE Trans. MTT*, pp. 270-277, Feb. 2007.
- [11] J-C. Chiao, F. Yiton, M.C. Iao, M. DeLisio, and L-Y. Lin, "MEMS reconfigurable Vee antenna", *IEEE MTT-S International Microwave Symposium Digest*, vol.4, pp.1515–1518, 1999.
- [12] C. W. Jung, M-J. Lee, G. P. Li, and F. De Flaviis, "Reconfigurable Scan-Beam Single-Arm Spiral Antenna Integrated with RF-MEMS Switches", *IEEE Transactions on Antennas and Propagation*, Vol.54, No.2, Part 1, pp.455–463, Feb. 2006.
- [13] Kiriazi, J., Ghali, H., Radaie, H., and Haddara, H., "Reconfigurable dual-band dipole antenna on silicon using series MEMS switches," *Proceedings of the IEEE/URSI International Symposium on Antennas and Propagation*, vol. 1, pp.403–406, 2003.
- [14] Weedon, W.H., Payne, W.J., and Rebeiz, G.M., "MEMS-switched reconfigurable antennas," *Proceedings of the IEEE/URSI International Symposium on Antennas and Propagation*, vol.3, pp. 654–657, 2001.
- [15] Panagamuwa, C.J., Chauraya, A., and Vardaxoglou, J.C., "Frequency and beam reconfigurable antenna using photoconducting switches," *IEEE Transactions on Antennas and Propagation*, vol. 54, pp. 449–454, February 2006.
- [16] Freeman, J.L., Lamberty, B.J., and Andrews, G.S., "Optoelectronically reconfigurable monopole antenna," *Electronics Letters*, vol. 28, no. 16, pp. 1502–1503, July 1992.
- [17] Bhartia, P., and Bahl, I.J., "Frequency agile microstrip antennas," *Microwave Journal*, vol. 25, pp. 67–70, October 1982.

- [18] Kawasaki, S., and Itoh, T., "A slot antenna with electronically tunable length," Proceedings of the IEEE/URSI International Symposium on Antennas and Propagation, vol. 1, pp. 130–133, 1991.
- [19] Kiely, E., Washington, G., and Bernhard, J.T., "Design and development of smart microstrip patch antennas," Smart Materials and Structures, vol. 7, no. 6, pp. 792–800, December 1998
- [20] Kiely, E., Washington, G., and Bernhard, J.T., "Design, actuation, and control of active patch antennas," Proceedings of the SPIE International Society for Optical Engineering, vol. 3328, pp. 147–155, 1998.
- [21] Bernhard, J.T., Kiely, E., and Washington, G., "A smart mechanically-actuated two-layer electromagnetically coupled microstrip antenna with variable frequency, bandwidth, and antenna gain," IEEE Transactions on Antennas and Propagation, vol. 49, pp. 597–601, April 2001.
- [22] Pozar, D.M., and Sanchez, V., "Magnetic tuning of a microstrip antenna on a ferrite substrate," Electronics Letters, vol. 24, pp. 729–731, June 9, 1988.
- [23] Mishra, R.K., Pattnaik, S.S., and Das, N., "Tuning of microstrip antenna on ferrite substrate," IEEE Transactions on Antennas and Propagation, vol. 41, pp. 230–233, February 1993.
- [24] Mishra, R.K., Pattnaik, S.S., and Das, N., "Tuning of microstrip antenna on ferrite substrate," IEEE Transactions on Antennas and Propagation, vol. 41, pp. 230–233, February 1993.
- [25] Langer, J.-C., Zou, J., Liu, C., and Bernhard, J.T., "Reconfigurable out-of-plane microstrip patch antenna using MEMS plastic deformation magnetic actuation," IEEE Microwave and Wireless Components Letters, vol. 13, pp. 120–122, March 2003.
- [26] Eom, H.J., Lee, S.U., "Leaky Wave in a Slotted Rectangular Waveguide" Antenna Technology: Small Antennas and Novel Metamaterials, 2008. iWAT 2008. International Workshop, Page(s):103 – 106, 4-6 March 2008
- [27] Tranquilly, J.M., Lewis, J.E., "On the Propagation of Leaky Waves in a Longitudinally Slotted Rectangular Waveguide" Microwave Theory and

- Techniques, IEEE Transactions on Volume 28, Issue 7, Page(s):714 – 718, July 1980
- [28] Dural,G., *Theory and Design of Microstrip Rampart Line Arrays*, Master Thesis, Metu, 1983
- [29] I.J.Bahl and P. Bhartia, *Microstrip Antennas*, Artech House, Inc., 1980.
- [30] J.R. James, P.S. Hall and C. WOOD, *Microstrip Antenna Theory and Design*, IEE Electromagnetic Waves Series 12, 1981.
- [31] R. E. Collin, *Foundations for Microwave Engineering*, McGraw-Hill, Inc., 1992.
- [32] S. Cheng, E. Öjefors, P. Hallbjörner, and A. Rydberg, “Compact Reflective Microstrip Phase Shifter for Traveling Wave Antenna Applications” IEEE Microwave and Wireless Components Letters, Vol.16, No.7, July 2006.
- [33] R. Ratmon, I. Oz, C. J. Samson, “Comparision of Resonant and Travelling-Wave Meander-Line Antenna” Electrical & Electronics Engineers in Israel, 1991, 17th Convebtion of. 5-7 March 1991 Page(s):149-151
- [34] M. Tiuri, S. Tallqvist, S. Urpo, “*Chain Antenna*” 1974 Antennas and Propagation Society International Symposium, Volume 12, Jun 1974 Page(s):274 – 277
- [35] C. Monzon, “A Small Dual-Frequency Transformer in Two Sections,” IEEE Trans. Microwave Theory & Tech., vol.51, pp.1157-1161, April 2003.
- [36] G.M. Rebeiz, J. B. Muldavin, “RF MEMS Switches and Switch Circuits” IEEE Microwave Magazine, pp. 59-71, December 2001.
- [37] RADANT MEMS SPST Switch-
[http://www.radantmems.com/radantmems.data/Library/Radant-](http://www.radantmems.com/radantmems.data/Library/Radant-Datasheet200_1.5.pdf)
 Datasheet200_1.5.pdf , Radant MEMS Inc, Hudson, MA, August, 2008.

APPENDICES

A. Effective Dielectric Constant and Characteristic Impedance of Microstrip Lines

The Characteristic impedance of a microstrip line of width w over a dielectric substrate of dielectric constant ϵ_r and thickness h , at the frequency f is given below.

$$\epsilon_e(f) = \epsilon_r - \frac{\epsilon_r - \epsilon_e(0)}{1 + (f/f_a)^m}$$

$$\epsilon_e(0) = \frac{\epsilon_r + 1}{2} + \frac{\epsilon_r - 1}{2} \left(1 + \frac{12h}{w}\right)^{-1/2} + F(\epsilon_r, h) - 0.217(\epsilon_r - 1) \frac{t}{\sqrt{wh}}$$

$$F(\epsilon_r, r) = \begin{cases} 0.02(\epsilon_r - 1)(1 - w/h)^2 & w/h \leq 1 \\ 0 & w/h > 1 \end{cases}$$

$$f_a = \frac{f_b}{0.75 + (0.75 - 0.332\epsilon_r^{-1.73})(w/h)}$$

$$f_b = \frac{299.7924562}{2\pi h \sqrt{\epsilon_r - \epsilon_e(0)}} \tan^{-1} \left[\epsilon_r \sqrt{\frac{\epsilon_e(0) - 1}{\epsilon_r - \epsilon_e(0)}} \right]$$

$$m = \begin{cases} m_0 m_c & m_0 m_c \leq 2.32 \\ 2.32 & m_0 m_c > 2.32 \end{cases}$$

$$m_0 = 1 + \frac{1.4}{1 + \sqrt{w/h}} + \frac{0.32}{(1 + \sqrt{w/h})^3}$$

$$m_c = \begin{cases} 1 + \frac{1.4}{1 + w/h} \left[0.15 - 0.235e^{-0.45f/f_a} \right] & w/h \leq 0.7 \\ 1 & w/h > 0.7 \end{cases}$$

$$Z_c = \sqrt{\frac{\mu_0 \varepsilon_0}{\varepsilon_e} \frac{1}{C_a}}$$

where

$$C_c = \begin{cases} \frac{2\pi\varepsilon_0}{\ln\left(\frac{8h}{w} + \frac{w}{4h}\right)} & w/h \leq 1 \\ \varepsilon_0 \left[\frac{w}{h} + 1.393 + 0.667 \ln(w/h + 1.444) \right] & w/h > 1 \end{cases}$$

B. ASELSAN Tapered Anechoic Chamber Measurement System

The measurements and evaluation of the sinuous antennas are performed in an anechoic chamber (see Figure B.1). Anechoic chamber is a reflection free (i.e. the reflectivity levels of the absorbers covering the whole room are very low, about -20 dB) room inside of which is covered by absorbers.

The tapered anechoic chamber is designed in the shape of pyramidal horn that tapers from the small source end to a large rectangular test region, and with high quality absorbing material covering the side walls, floor and ceiling. The tapered anechoic chamber in the R&D department of Aselsan Inc. is used with an azimuth over elevation positioner holding up the antenna under test, a polarization positioner holding up the standard transmitter antenna, an Agilent PNA model vector network analyzer, and HP PII series computers using programs written in HP VEE program at Aselsan and which communicate with the above listed equipment through the aid of HP-IB's. Antenna measurement set up in anechoic chamber is shown in Figure B.2.

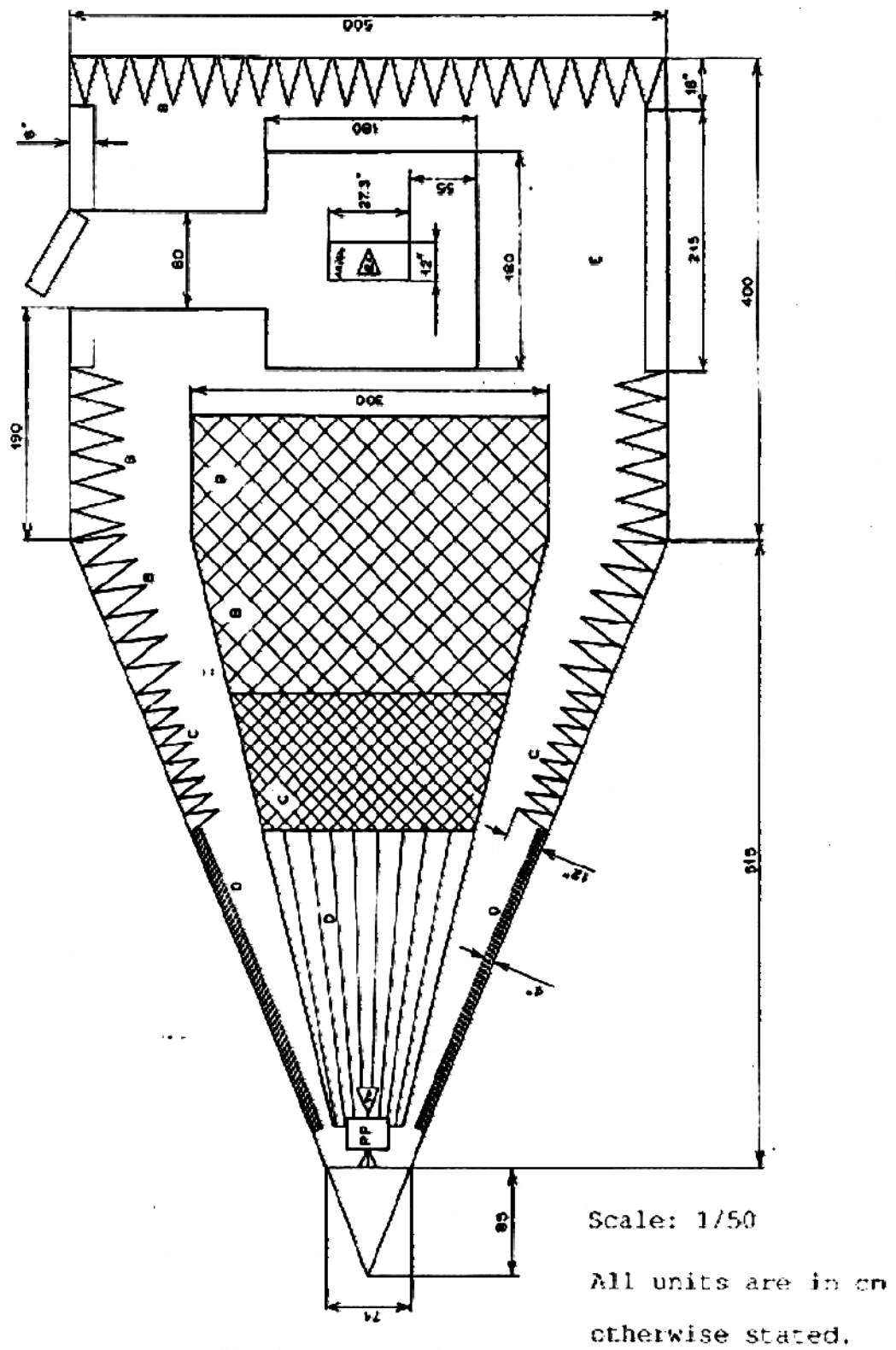


Figure B.1 Top view of the Tapered Anechoic Chamber in Aselsan Inc.

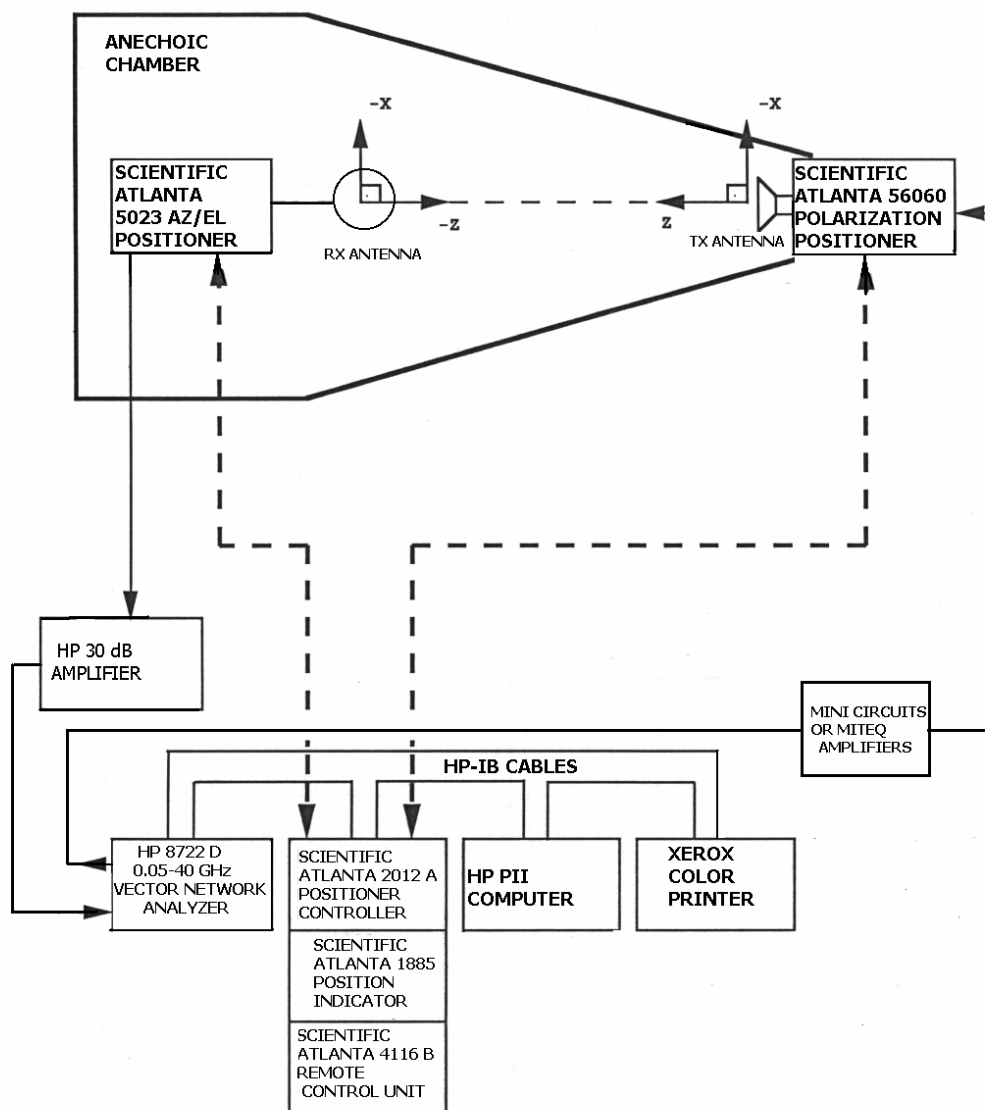


Figure B.2 Antenna Measurement Setup in Anechoic Chamber

C. RO5880 High-Frequency Laminate Datasheet



Advanced Circuit Materials Division
100 S. Riverwalk Avenue
Chandler, AZ 85226
Tel: 480-961-1382, Fax: 480-961-4533
www.rogerscorporation.com

Data Sheet
1,3000

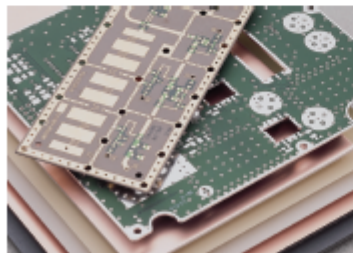
RT/duroid® 5870 / 5880 High Frequency Laminates

Features:

- Lowest electrical loss for reinforced PTFE material.
- Low moisture absorption.
- Isotropic
- Uniform electrical properties over frequency.
- Excellent chemical resistance.

Some Typical Applications:

- Commercial Airline Telephones
- Microstrip and Stripline Circuits
- Millimeter Wave Applications
- Military Radar Systems
- Missile Guidance Systems
- Point to Point Digital Radio Antennas



RT/duroid® 5870 and 5880 glass microfiber reinforced PTFE composites are designed for exacting stripline and microstrip circuit applications.

Glass reinforcing microfibers are randomly oriented to maximize benefits of fiber reinforcement in the directions most valuable to circuit producers and in the final circuit application.

The dielectric constant of RT/duroid 5870 and 5880 laminates is uniform from panel to panel and is constant over a wide frequency range. Its low dissipation factor extends the usefulness of RT/duroid 5870 and 5880 to Ku-band and above.

RT/duroid 5870 and 5880 laminates are easily cut, sheared and machined to shape. They are resistant to all solvents and reagents, hot or cold, normally used in etching printed circuits or in plating edges and holes.

Normally supplied as a laminate with electrodeposited copper of $\frac{1}{4}$ to 2 ounces/R.² (8 to 70µm) on both sides, RT/duroid 5870 and 5880 composites can also be clad with rolled copper foil for more critical electrical applications. Cladding with aluminum, copper or brass plate may also be specified.

When ordering RT/duroid 5870 and 5880 laminates, it is important to specify dielectric thickness, tolerance, rolled or electrodeposited copper foil, and weight of copper foil required.

The information in this data sheet is intended to assist you in designing with Rogers' circuit material laminates. It is not intended to and does not create any warranties express or implied, including any warranty of merchantability or fitness for a particular purpose or that the results shown on this data sheet will be achieved by a user for a particular purpose. The user should determine the suitability of Rogers' circuit material laminates for each application.

The world runs better with Rogers.™

Figure C.1 RO5880 High-Frequency Laminate Datasheet

PROPERTY	TYPICAL VALUE		DIRECTION	UNITS	CONDITION	TEST METHOD
	RT/duroid® 3813	RT/duroid® 3810				
Dielectric Constant, ϵ_r	2.33 2.33 ± 0.02 spec.	2.29 2.29 ± 0.02 spec.	Z Z		C/W/25/90 C/W/25/90	1 MHz IPC TM-450, 2.5.5.2 30 GHz IPC TM-2.5.5.5
Dissipation Factor, tan δ	0.0005 0.0002	0.0004 0.0009	Z Z		C/W/25/90 C/W/25/90	1 MHz IPC TM-450, 2.5.5.3 30 GHz IPC TM-2.5.5.5
Thermal Coefficient of ϵ_r	-115	-125		ppm/°C	-50~150°C	IPC TM-450, 2.5.5.5
Volume Resistivity	2×10^{12}	2×10^{12}	Z	Mohm-cm	C/W/25/90	ASTM D257
Surface Resistivity	2×10^9	2×10^9	Z	Mohm	C/W/25/90	ASTM D257
Tensile Modulus	Test at 25°C	Test at 100°C	Test at 25°C	Test at 100°C		
	100 (psi)	40 (psi)	100 (psi)	40 (psi)	X	
	100 (MPa)	40 (MPa)	100 (MPa)	40 (MPa)	Y	
	40 (psi)	34 (psi)	37 (psi)	31 (psi)	X	
Ultimate Stress	40 (psi)	34 (psi)	37 (psi)	31 (psi)	Y	
	18	8.7	6.8	7.2	X	
	18	8.8	4.9	5.8	Y	
	1010 (psi)	40 (psi)	710 (psi)	300 (psi)	X	
Compressive Modulus	1010 (psi)	440 (psi)	710 (psi)	300 (psi)	Y	
	40 (psi)	34 (psi)	37 (psi)	31 (psi)	X	
	40 (psi)	34 (psi)	37 (psi)	31 (psi)	Y	
	37 (psi)	28 (psi)	37 (psi)	21 (psi)	X	
Ultimate Stress	37 (psi)	28 (psi)	37 (psi)	21 (psi)	Y	
	40	40	8.8	8.4	X	
	3.3	3.3	7.7	7.8	Y	
	8.7	8.8	10.8	10.4	Z	
Deformation Under Load, Test at 180°C			1.0		X	200/14 MPa (2 ksi)
Heat Distortion Temperature	>260 (>500)	>260 (>500)	X,Y	°C (°F)	140 MPa (20 ksi)	ASTM D648
Specific Heat	0.94 (0.22)	0.94 (0.22)		J/gK		Calculated
Moisture Absorption	Thickness: 0.31" (8mm)	0.9 (0.02)				
	0.62" (16mm)	10 (0.015)				
Thermal Conductivity	0.22	0.25	Z	W/mK		ASTM C518
Thermal Expansion	X	Y	Z	X	Y	Z
	-6.0	-6.8	-11.4	-6.7	-8.7	-16.7
	-6.4	-6.9	-6.0	-6.9	-1.8	-6.9
	-0.3	-6.4	-6.4	-6.8	-6.9	-6.8
	0.7	0.9	7.8	1.1	1.8	8.7
	1.8	3.2	20.9	3.3	3.2	26.3
	3.4	4.0	50.7	3.8	5.8	69.8
Td	300	300		°C TGA		ASTM D3850
Density	2.2	2.2				ASTM D792
Copper Foil	25.0 (3.7)	25.0 (4.0)		µl (mm)	after solder float	IPC TM-450 2.4.6
Flammability	96V0	96V0				UL
Lead-free Process Compatible	Yes	Yes				


[1] If unit given list with other frequently used units in parentheses.
 [2] Reference: Interval 1% 140, 225, 265, Reference at 25°C unless otherwise noted.
 Typical values should not be used for specification limits.

STANDARD DIMENSIONS		STANDARD PANEL SIZE		STANDARD COPPER CLADDING	
0.005" (0.127mm)	0.021" (0.533mm)	36" X 12" (457 X 305mm)	1/2 oz. (15µm) electrodeposited copper foil.	1/2 oz. (15µm), 1 oz. (35µm), 2 oz. (70µm) electrodeposited and rolled copper foil.	
0.010" (0.254mm)	0.043" (1.092mm)	36" X 24" (457 X 609mm)			
0.015" (0.381mm)	0.125" (3.175mm)	36" X 36" (457 X 914mm)			
0.020" (0.508mm)		36" X 48" (457 X 1,219mm)			

The information in this data sheet is intended to assist you in designing with Rogers' circuit material laminates. It is not intended to and does not create any warranties express or implied, including any warranty of merchantability or fitness for a particular purpose or that the results shown on this data sheet will be achieved by a user for a particular purpose. The user should determine the suitability of Rogers' circuit material laminates for each application.
 These commodities, technology and software are exported from the United States in accordance with the Export Administration regulations, Division contrary to U.S. law prohibited.
 © 1989, 1994, 1995, 1999, 2002, 2005, 2006 Rogers Corporation, Printed in U.S.A. All rights reserved.
 Revised 11/06 0696-1106-0.5CC Publication #92-101

Figure C.2 RO5880 High-Frequency Laminate Datasheet

D. MICROSEMI MPV-2100 Varactor Diode Datasheet



Microsemi
MICROWAVE PRODUCTS DIVISION

MPV1965, MPV2100

**MONOLITHIC MICROWAVE SURFACE MOUNT
VARACTOR DIODES**

PRODUCT PREVIEW

DESCRIPTION

This series of surface mount Varactor diodes utilize new and unique monolithic MMSM technology. The technology is a package/device integration accomplished at the wafer fabrication level. Since the cathode and anode interconnections utilize precision photolithographic techniques rather than wire bonds, parasitic package inductance is tightly controlled. The package parasitics provide smooth non-resonant functionality through 12GHz.

IMPORTANT: For the most current data, consult MICROSEMI's website: <http://www.microsemi.com>



KEY FEATURES

- Tape and Reel for Automatic Assembly
- Low Series Inductance (<0.2nH typical)
- Low Parasitic Capacitance (0.05 pF typical)
- Meets All Commercial Qualification Requirements
- 0204 Outline
- Very low thermal resistance

APPLICATIONS/BENEFITS

- 2.4 GHz PCB
- 5.7 GHz Wireless LANs
- VCO's (Voltage Controlled Oscillator)
- Tunable Filter
- Widest bandwidth of any commercial surface mounted device
- Ultra tight parametric distribution

ELECTRICAL CHARACTERISTICS

Part #	Vb@10uA (min) Volts	Cr@1V (Tf)	Cr 1V/ Cr 3V (Tf)	Cr 1V/ Cr 6V (Tf)	Q (Min/4v/ 50MHz)	Outline Dwg Number	APPLICATION
MPV1965	15	2.6-3.8	1.4-2.2	2.6-3.6	1500	206	Low Voltage VCO

ELECTRICAL CHARACTERISTICS

Part #	Vb@10uA (min) Volts	Cr@4V Tf	Cr 0V/ (Typ) (Tf)	Cr @ 20V (Tf)	Q (Min/4v/ 50MHz)	Outline Dwg Number	APPLICATION
MPV2100	22	0.9-1.5	3.25	0.2-0.5	1500	206	Wide Bandwidth VCO

Figure D.1 MICROSEMI MPV-2100 Varactor Diode Datasheet

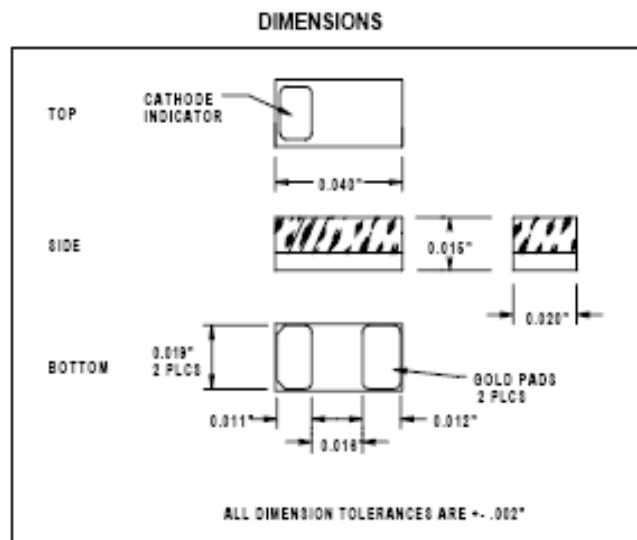


Figure D.2 MICROSEMI MPV-2100 Varactor Diode Datasheet

E. MEMS Switch Operation

RF MEMS switches are commonly used in phase shifters and switching networks up to 120 GHz due to their improved performance compared to p-i-n or field-effect transistor (FET) diode switches. RF MEMS application areas are in phase arrays and reconfigurable apertures for defense and telecommunication systems, switching networks for satellite communications.

MEMS switches are devices that use mechanical movement to achieve a short circuit or an open circuit in the RF transmission line. In order to achieve mechanical movement electrostatic, magnetostatic, piezoelectric, or thermal forces can be used. In fact, only electrostatic-type switch's operation has been verified at 0.1-100GHz with high reliability [36].

There are two types of RF MEMS switches: shunt switch and series switch. Shunt and series switches have two states; up and down state. Figure E.1 shows the up state of the series and shunt SPST MEMS switches. In the down state, as seen from Figure E.2 the bridge collapses due to DC actuation to the switch mechanism.

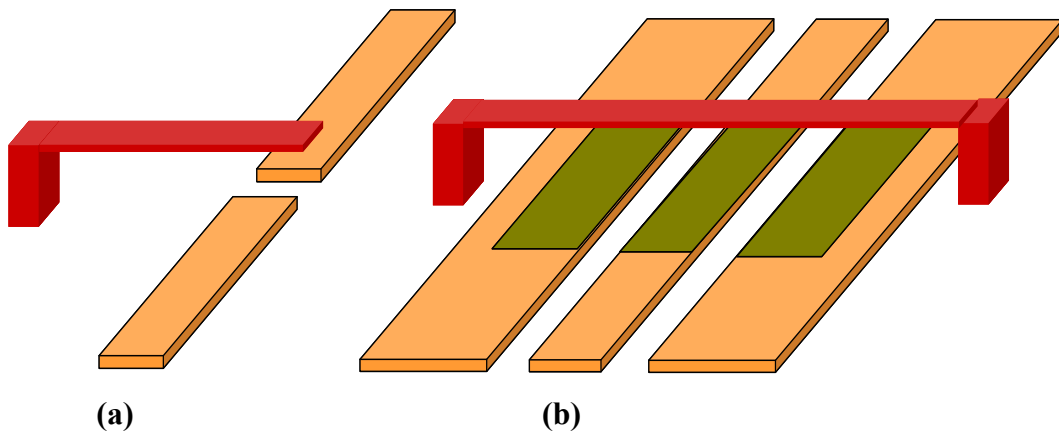


Figure E.1 Up State Schematic Models of (a) Series SPST Switch (b) Shunt SPST RF MEMS Switch

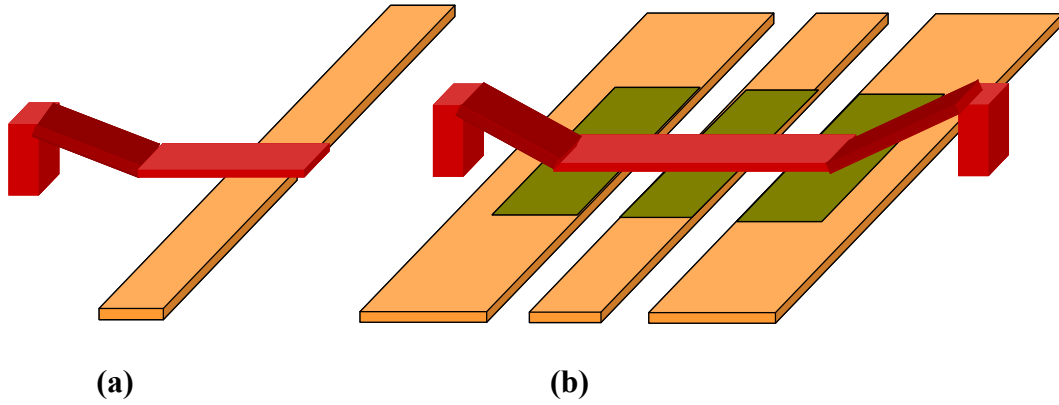


Figure E.2 Down State Schematic Models of (a) Series SPST Switch (b) Shunt SPST RF MEMS Switch

The schematic model of the RADANT SPST MEMS shunt switch is shown in Figure E.3 [37]. A MEMS shunt switch has up- and down- states. In the down-state, a voltage is applied between the gate and source electrodes. The free end of the switch contacts the drain and completes an electrical path between the drain and the source. When the applied voltage is removed, the MEMS bridge returns back to its original position.

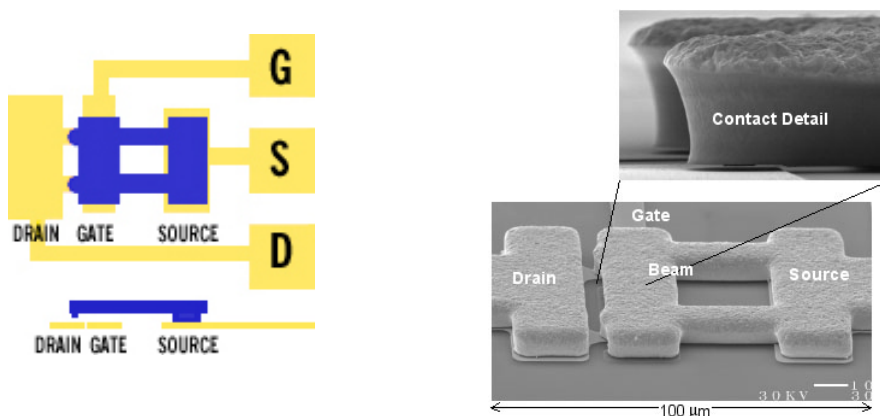


Figure E.3 Schematic Model and Photograph of RADANT SPST RF MEMS Shunt Switch